UNIVERSITY OF CALIFORNIA
SANTA CRUZ

UNRAVELING THE MAGMATIC AND GEOMORPHIC PROCESSES RECORDED IN THE TOPOGRAPHY OF THE CENTRAL ANDES

A dissertation submitted in partial satisfaction of the
requirements for the degree of

DOCTOR OF PHILOSOPHY

in

EARTH & PLANETARY SCIENCES

by

Jonathan P. Perkins

December 2015

The Dissertation of Jonathan P. Perkins
is approved:

Dr. Noah J. Finnegan, Chair

Dr. Emily E. Brodsky

Dr. David M. Rubin

Dr. Jeremy K. Hourigan

Tyrus Miller
Vice Provost and Dean of Graduate Studies

Table of Contents

List of Figures

List of Tables

Abstract

Unraveling the magmatic and geomorphic processes recorded in the topography of the Central Andes

by

Jonathan P. Perkins

The topography of volcanic arcs reflects a combination of magmatic ascent processes that deform the overlying crust, volcanic eruptions that blanket the surface in lava and ash, and geomorphic processes that shape these deposits into the observable landscape and consequently record an erosional archive of surface deformation. A central goal of geomorphology is to utilize the form of landscapes to infer the processes that shape them, yet comparatively little work has been done to quantitatively understand the geomorphology of volcanic landscapes. The Central Volcanic Zone of the South American Andes (CVZ, 15-28°S) represents an ideal location for understanding the processes that shape the surface of volcanic arcs; the arid climate and well-constrained geochronology of volcanic deposits provide a geomorphic archive going back 11 Myrs, and the wealth of available geophysical imaging data provides a high-resolution glimpse into the subsurface. In this thesis I utilize geormophic and geophysical data to explore fundamental questions in volcanic landscape evolution at varying spatial scales. To begin, I examine the isostatic uplift response to crustal intrusion of mantle-derived melt, resulting in growth of the largest known active magma reservoir on Earth (the Altiplano-Puna Magma Body). From topography I show that it is possible to calculate the contribution of mantle-derived melt to crustal thickening, and I compare these results to independent seismic estimates that agree well with our data. I then use the record of volcanic deposits from the Altiplano-Puna

Magma Body to estimate the flux of mantle melt into the crust, and show that predicted uplift rates are comparable to the surface uplift associated with convective lithospheric removal. Next, I explore how the topography of individual volcanic systems can help discern the style of melt ascent from deeper crustal magma reservoirs to shallow ones. Using two actively deforming volcanoes in the CVZ, Uturuncu volcano and the Lazufre volcanic complex, I use river profiles, lake shorelines, and lava flow deflections to infer each volcano's surface deformation record into the geomorphic past. Uturuncu volcano shows little signs of permanent paleo-deformation, suggesting transient ascent of magma over millenial timescales, while Lazufre's long wavelength deformation suggests continued accumulation of magma since > 0.3 Ma. Finally, I utilize the unique topography of a windswept ignimbrite erupted from the Altiplano-Puna Magma body to better understand how wind abrasion can incise bedrock canyons, a fundamental geomorphic process in arid landscapes on both Earth and Mars. Using a natural experiment within the 4 Ma Puripicar ignimbrite on the western slope of the Central Andes, we quantify the relative contribution of wind and water erosion in propagating bedrock canyons and show that wind can incise canyons an order of magnitude faster than rivers, streamlining their profiles in the process. Thus, in these chapters I illustrate how geomorphology can be a useful tool for quantifying subsurface magmatic processes, while volcanic landscapes themselves can also provide unique opportunities for understanding fundamental planetary geomorphic processes not often observed elsewhere on Earth.

For my tremendously supportive parents, Alan and Diana, and for Sarah, whose infinite patience and positivity are an inspiration.

Special thanks to Zoe, my cat, for offering persistent and creative typing suggestions.

Acknowledgments

This thesis has been a collaborative endeavor from start to finish, and there are many friends, family, and colleagues to thank who have helped me both personally and scientifically. First, I would like to thank my Advisor, Noah Finnegan, who gave me the freedom to explore ideas and concepts throughout graduate school, and who had the guidance to nudge me in the right direction when those ideas led me astray. Noah, I hope I can emulate your and intellectual rigor and excitement for novel research in the future!

I would also like to thank the other members of my thesis committee: Emily Brodsky, David Rubin, and Jeremy Hourigan. Trying to complete a thesis that combines large scale geodynamic problems with grain-scale sediment transport mechanics by wind often put me in the deep end of fields that I was not initially familiar with, and I would have made very little traction without their support. I would also like to thank Shan de Silva, who operated as a de facto advisor for these projects and whose deep knowledge of the Central Andes and collaborative support for my work made this thesis possible.

A number of other scientists have helped me significantly during this process. Francis Nimmo has been kind enough to meet with me over the years to explain (and re-explain) a number of geophysical methods to me. Tammy Rittenour and Greg Balco have offered much advice with the gathering and processing of geochronlogy samples for a number of projects. Kevin Ward and Scott Henderson have been invaluable resources for thinking about magmatism and topography.

My interest in geology started my freshman year at San Francisco State University, due in large part to the amazing and attention-grabbing teaching of Dr. David Mustart. Over the course of my time at SFSU Karen Grove provided constant inspiration and taught me how to think, do, and teach geology. John

Caskey's field courses taught me how to approach complicated field problems and begin to solve them.

Leonard Sklar introduced me to the field of geomorphology and the sometimes strenuous but rewarding process of independent scientific research. It is difficult not to be inspired by his passion for understanding the natural world, and I am grateful to be one of the many who caught the bug!

I cannot thank enough the geomorphology lab past and present at UC Santa Cruz: Kerri Johnson, Danica Roth, Allison Pfeiffer, Claire Masteller, Alex Nereson, Dave Santaniello, and Rachael Klier. It is both inspiring and motivating to be around so many brilliant, creative, and hard-working people! Thank you especially to Kerri Johnson, who accompanied me in Chile and Bolivia and whose insightful field observations there helped me think about landscape evolution in a new light. I would also like to thank our post-doc, Christian Braudrick, who has provided advice and conversation since I first met him at UC Berkeley 8 years ago.

Sam Johnstone has been a tremendous help and exceedingly generous over the years, offering guidance on many aspects of numerical modeling, topographic analysis, and image processing techniques.

Joel Scheingross has been my foremost geomorphic confidant, partner in geo-tourism, and primary peer-advice-giver since we were first paired as mapping partners in 2006. You are a great friend and an impossible yard-stick.

Mikael Witte, Don Penman, and Danica Roth made the best science/adventure cohort one could ask for.

A note, chapters 2 and 4 are formatted for the journal publication *Nature Geoscience* (Chapter 2 is in submission, and Chapter 4 has been published). As such, the formatting for these chapters strays from what is more conventionally

seen in dissertations. Here we include referenced abstracts, and because the journal is short-format, the chapters are as succinct as possible.

In Chapter 2, I worked closely with research scientists outside of my thesis committee, who are co-authors on the manuscript which has recently been submitted: Kevin M. Ward (University of Arizona), Shanaka L. de Silva (Oregon State University), George Zandt (University of Arizona), and Susan L. Beck (University of Arizona).

In Chapter 3, I collaborate with two researchers outside of my committee, who are co-authors on this manuscript, which is currently in review: Dr. Tammy Rittenour of Utah State University, who helped me process and interpret my geochronology data, and Scott Henderson of Cornell University, who processed the InSAR data and worked with me to help interpret the data in the context of melt ascent models. This chapter is presently in review at an academic journal.

Though chapter 4 has been published, in lieu of including a reprint I include some additional work that was not included in the manuscript. In this chapter I also collaborated with Dr. Shanaka de Silva from Oregon State University, who is a co-author on the published manuscript and helped guide field work and interpretation of the volcanology and wind-erosional landforms of the APVC.

The bulk of this dissertation was generously supported by the National Science Foundation Grant EAR 0908850, which formed the financial basis for the PLUTONS project (plutons.oregonstate.edu). I would like to thank the whole PLUTONS group for their collegiality and willingness to help with fieldwork and explain complicated geophysical concepts to an ignorant geomorphologist. In particular, Matthew Pritchard has been very helpful with field and research logistics. I would also like to thank the UCSC Graduate Division, whose Dissertation Quarter Sabbatical Fellowship allowed me the time to get my chapters

ready to publish and finish this document.

Last, I would like to thank my family members who all offered support, love, and hilarity thoughout my time in graduate school: Mom, Dad, Grandma, Mike, Chris, Jen, Addison, Linden, and Hayden. I could not have done this without you all! And finally, I would like to thank my partner Sarah, who offered unbelievable kindness, love, understanding, and snacks.

"May not subterraneous fire be considered as the great plough (if I may be allowed the expression) which Nature makes use of to turn up the bowels of the earth?"

-Sir William Rowan Hamilton

Observations on Mount Vesuvius, Mount Etna, and other volcanoes (1774), 161.

Chapter 1

Introduction

Geomorphology as it applies to volcanic landscapes is an emerging scientific field. A small but growing body of literature exists describing the geomorphic response to volcanic disturbances (e.g., Smith, 1987; Major, 1990; Gran and Montgomery, 2005), the geomorphic and fluid dynamical properties of erupted material (e.g., Cashman, 2009; Dufek, 2009), and the geomorphic impact of a growing magma chamber (e.g. Ouichi, 1985; Finnegan and Pritchard, 2009). The studies presented in this dissertation build on these ideas, and use quantitative tools from the field of process geomorphology along with modern geochronologic and geophysical techniques to solve both applied and theoretical problems in volcanic landscapes. The primary questions I am asking through these projects are:

1) How can we use geomorphology to learn about magmatic processes at depth, such as the growth and ascent of mantle melt to form batholiths and upper-crustal reservoirs that feed caldera-forming systems ?

And conversely,

2) What can the unique topographic properties of volcanic landscapes tell us about fundamental geomorphic processes?

This projects of this dissertation are laid out in an arc along the evolutionary path of a silicic volcanic system, starting with questions addressing the topographic response to growth of a mid-crustal batholith that feeds a volcanic complex, then exploring the surface deformation styles associated with upward ascent of melt to shallow reservoirs in potential caldera-forming systems, and finally examining the erosional mechanics and spatiotemporal evolution of an ancient landscape created through the cumulative emplacement of erupted material over 11 Myrs.

In Chapter 2 I quantify the topographic growth associated with intrusion of the largest known active melt reservoir on Earth, the Altiplano-Puna Magma Body (APMB). At such large spatial (200-300 km) and volumetric (500,000 km^3) scales, the crust responds to changes isostatically, and we show using an isostatic model that surface uplift of the APMB can be related to the magnitude of mantle-derived melt addition to the crust. We then use the record of volcanism associated with APMB growth to estimate the tempo of mantle melt flux to the crust since 11 Myr, and show that surface uplift rates associated with magmatic addition are within a factor of 2 of those associated with convective lithospheric removal (e.g., Ghosh et al., 2006; Garzione et al., 2014), the main engine of rapid surface uplift in the Altiplano since the Miocene.

Chapter 3 focuses on the paleo-geodetic history of both Uturuncu volcano and the Lazufre volcanic zone, two CVZ volcanoes that are presently experiencing a phase of rapid topographic and magmatic growth. InSAR satellite measurements of surface deformation provide data going back two decades (Pritchard and Simons, 2002), but as silicic magma chambers grow over hundreds of thousands of

years in the lead up to eruption (e.g., Vasquez et al., 2002), long term deformation rates are necessary for interpreting the evolutionary stage and eruptive potential of these volcanoes. Geomorphic processes operate over such timescales, and here we use a combination of Pleistocene lake shorelines dated with OSL geochronology, river longitudinal profiles, and lava flow directions to infer the topographic and magmatic growth of Uturuncu of Lazufre over the Pleistocene. What we find is essentially that Uturuncu, being connected to the APMB, appears to be deforming due to the ascent of melt from a lower crustal reservoir into the APMB. Lazufre on the other hand, with a shallower deformation source and long-lived, long-wavelength topographic dome, appears to be accumulating magma and deforming for over 300 kyrs.

In Chapter 4, rather than apply a geomorphic approach to a volcanology problem I instead use a landscape formed by large-scale volcanism to learn about the mechanics of transient erosional processes in bedrock by wind and water. The Altiplano Puna Volcanic Complex (APVC) is home to a 12,800 km^3 ignimbrite flare-up, beginning at 11 Ma and lasting up to the present (Salisbury et al., 2011). It is also home to immensely strong (Milana et al., 2009) and geologically consistent (e.g., Green et al., 1995) winds that result from deflection of the westerly subtropical jet stream over the Altiplano (e.g., Vuille et al., 1999). The landscape of the APVC is unique because its surfaces showcase dramatic patterns of landforms that reflect the prolonged influence of wind erosion into bedrock, which is at present a poorly understood process (Goudie, 2008). Here I use the well-constrained topography and geochronology of the 4.09 Ma Puripicar ignimbrite to quantitatively understand how wind abrasion of bedrock can shape landscapes.

Through the chapters presented in this dissertation, it is my hope to illustrate

both the utility of geomorphic approaches for understanding magmatic processes within the Earth's crust, and the utility of volcanic landscapes as natural laboratories to quantitatively understand geomorphic processes.

Chapter 2

Surface uplift in the Central Andes driven by growth of the Altiplano-Puna Magma Body

2.1 Abstract

The Altiplano Puna Magma Body (APMB) in the Central Andes is the largest imaged magma reservoir on Earth (Zandt et al., 2003; Ward et al., 2014) and is located below the second highest orogenic plateau on Earth, the 4.5 km tall Altiplano-Puna. Although the APMB is a first-order geologic feature similar to the Sierra Nevada batholith in CA, both its magma production rate (Ward et al., 2015; Kay et al., 2010) and its role in the surface uplift history of the Central Andes (e.g., Allmendinger et al., 1997; Ghosh et al., 2006) remain uncertain. Here we show that a long-wavelength, 1 km high topographic dome overlies the seismically measured extent of the APMB. Exposed basement rock elevations show that doming is a structural feature, and low isostatic residual gravity anomalies suggest that the

uplift is isostatically compensated. Using a buried load isostatic model (e.g., Forsyth, 1985; Watts, 2001) we estimate an arc mantle magmatic production rate of 195 km^3/km/Myr to the Altiplano-Puna since 11 Ma. Our estimate compares well with independent seismic estimates of magmatic volume (Ward et al., 2014), and suggests that the APMB growth is comparable to the peak Cretaceous flare-up in the Sierran batholith (Ducea and Barton, 2007; Paterson and Ducea, 2015). Our analysis reveals that magmatic addition may provide a contribution to surface uplift on par with lithospheric removal, and more generally illustrates that surface topography may help quantitatively constrain the magnitude of pluton-scale melt production.

2.2 Introduction

The APMB resides within the Altiplano-Puna plateau, a region that is characterized by a higher mean elevation than the Altiplano to the north (Isacks, 1988; Allmendinger et al., 1997), a thickened crust (Prezzi et al., 2009; Tassara and Echaurren, 2012), and a very thin mantle lithosphere (Tassara and Echaurren, 2012) (Fig. 1a).

The thin lithosphere beneath the APVC may result from convective removal (Kay and Coira, 2009; de Silva et al., 2006; Beck et al., 2015), a potentially cyclical process (e.g.,DeCelles et al., 2009) that has contributed to pulses of rapid surface uplift throughout the history of the Central Andes (Garzione et al., 2014). The mantle heat flux associated with lithospheric removal is thought to be responsible for the flare-up of large-volume ignimbrites (Babeyko et al., 2002; de Silva et al., 2006; Kay and Coira, 2009), collectively known as the Altiplano-Puna Volcanic Complex (APVC) (de Silva, 1989b), since 11 Ma (Salisbury et al., 2011). Chemical compositions of the ignimbrites show a roughly equal contribution from crustal

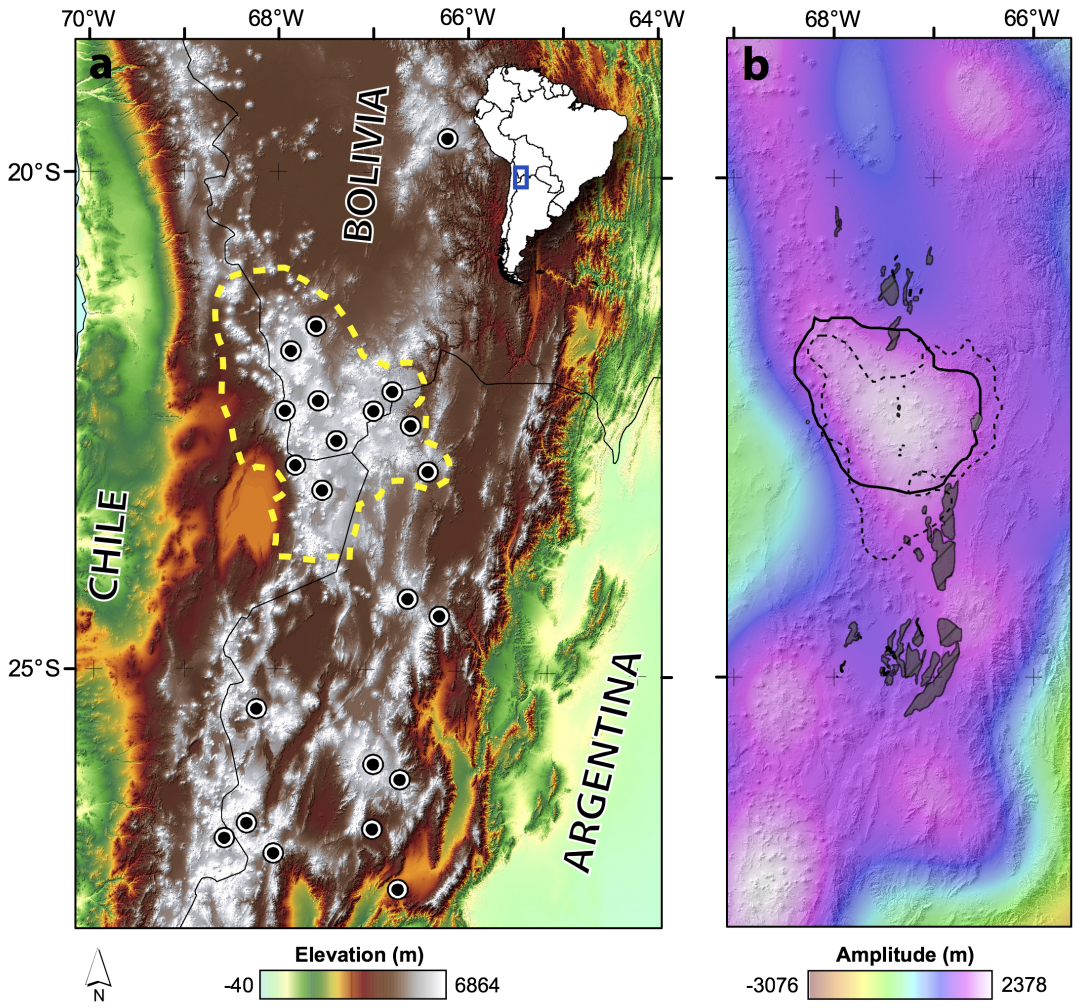

Figure 2.1: Location map of the study area in the Central Andes. The left panel shows the approximate extent of the Altiplano-Puna Volcanic Complex (APVC) (dashed yellow line). Caldera locations are denoted by black circles. Right panel shows the locations of basement outcrops (gray blobs), the 2.9 km/s velocity contour that roughly defines the extent of the APMB (solid black line) and the -400 mGal Bouguer gravity anomaly of Prezzi et al. (2009) (dashed black line) overlain on the long wavelength topography.

and mantle sources (Kay et al., 2010; de Silva, 1989a), consistent with extensive melting of the upper mantle and crust. Though horizontal shortening alone may not account for the crustal thickness observed in the APVC (e.g., Allmendinger et al., 1997) the role of magmatic addition in contributing to the crustal evolution and surface uplift history of the region is often neglected, due largely to the lack of constraints on the volume of magmatic material within the crust (e.g., Isacks, 1988; Allmendinger et al., 1997). However, new tomographic evidence by Ward et al., (2014) reveal an immense, 500,000 km^3 zone of partial melt at 10 to 20 km depth beneath the APVC, which substantially changes predictions for both the APMB's magma production rate and contribution to crustal thickening (and thus surface uplift). Here our primary goal is to test whether melt intrusion into the APMB is actually reflected in the topography and geology of the APVC, and if so, to then utilize this topographic signature to help place bounds on estimates of mantle melt intrusion into the crust.

2.3 Methods

2.3.1 Topographic analysis

To examine the surface topographic signal associated with the growth of the APMB we utilize both the long wavelength topography and Paleozoic basement outcrop elevations generated from a 90 m SRTM digital elevation model. To look at the long wavelength component of the topography in our study area, we first downsample the SRTM data to a 1 km grid size, then take the 2D Fourier transform of the data using Matlab's built in *fft2* command. We then multiply the transformed dataset by a lowpass filter with a cutoff wavelength of 175 km, and finally take the inverse transform of the filtered data to recover the long wavelength

Table 2.1: Parameters used for isostatic and magma production rate models

Symbol	Name	Value	Units
g	Gravity	9.81	m/s^2
H_b	Topographic amplitude	800-1200	m
W_i	Magmatic addition volume	-	km^3
F_{whm}	Full width at half max	230	km
ρ_c	Density of crust	2700-2850	kg/m^3
ρ_a	Density of asthenosphere	3200-3300	kg/m^3
k	wave number	-	$1/m$
T_e	Elastic thickness	15000	m
E	Young's Modulus	70	Gpa
ν	Poisson's Ratio	0.25	-
D	Flexural Rigidity	$2x10^{22}$	Nm
α	Volcanic volume	12,820	km^3
β	Plutonic:volcanic	-	-
μ	crust:mantle provenance	0.5	-
η	dense residue:melt	0.5	-
λ	arc-parallel length	230	km
ξ	Mantle magma prod. rate	-	$km^3/km/Myr$
τ	Timescale of melt accumulation	11	Myr

topography in xy space. The basement rock exposures that dot the surface of the APVC consist of Paleozoic basement rock associated with the Antofalla terrane (Ramos, 2008). The folded and tilted strata associated with surface exposures of the Antofalla terrane near the APMB contrast markedly with the overlying deposits of volcanic rock, making their identification relatively straightforward in satellite imagery. We thus map exposures of this basement along the APMB using high-resolution satellite imagery in Google Earth, and extract their surface elevations using 90 m SRTM topographic data within ArcGIS. To visualize the data, we plot the outcrop centroid and its median elevation in Figures 2.2 and 2.3.

2.3.2 Isostatic modeling of melt contribution

We use the long wavelength topographic anomaly above the APMB to model the isostatic load at depth using a buried load isostatic model (Watts, 2001; Forsyth, 1985). The conceptual model underlying the mathematical one assumes that the crust is thickening from addition of material at its base. In the case of our study, we assume that crust is being added by mantle-derived melt as upwelling warm asthenosphere replaces the relatively colder (and denser) lithosphere that was removed through delamination. We can therefore model the original contribution to crustal thickening from accumulation of mantle-derived melt as a convolution of the topographic load profile and the isostatic response function in frequency space:

$$W_i = -H_b(k)(\frac{\rho_c}{\phi_{....}(k)\Delta\rho}) \tag{2.1}$$

where k corresponds to the wavenumber, $Hb(k)$ is the Fourier transform of the topographic response profile, $Wi(k)$ is the Fourier transform of the buried load profile, ρ_c is the density of the crust, $\Delta\rho = \rho_m - \rho_c$, and $\phi_{....}(k)$ is the isostatic response function, defined as:

$$\phi_{....}(k) = \frac{Dk^4}{\rho_c g + 1}. \tag{2.2}$$

D is the flexural rigidity of the crust:

$$D = \frac{ET_e^3}{12(1-\nu^2)}, \tag{2.3}$$

where E is the Young's modulus, T_e is the effective elastic thickness of the crust, and ν is Poisson's ratio (0.25). Parameters used in our calculations are found

in Table 2.1. In order to mitigate the extreme sensitivity of the calculation to high-frequency noise, and isolate the component of long wavelength topography associated with the APMB, we approximate the long wavelength topographic response profile as a Gaussian curve with an amplitude of approximately 1200 m and a full-width at half-maximum of 232 km (Fig. 2.5). Forward modeling this curve yields a Gaussian buried load profile extending to about 9 km depth at its maximum (Fig. 2.5). To estimate the root volume from the 1D profile, we assume radial symmetry of the load and calculate the volume of the 2D Gaussian directly numerically using trapezoidal integration.

2.3.3 Arc mantle magma production rate

We can relate our modeled isostatic root volume to independent estimates of mantle-derived melt volume utilizing the seismically imaged magma chamber volume and an arc mantle production rate model (e.g., Ward et al., 2014; Paterson and Ducea, 2015). As shown in Ward et al., 2014, mantle-derived melt flux can be related to APMB volume via the following formulation:

$$\xi = \frac{\alpha(\beta+1)}{(\frac{\mu+1}{\eta+1})\lambda\tau}. \tag{2.4}$$

Here, ξ is the cross-sectional arc mantle magma production rate ($km^3/km/Myr$), α is the volume of volcanic material, β is the plutonic:volcanic ratio, η is the ratio of dense residue mass to melt mass, μ is the ratio of crust to mantle melt provenance, λ is the arc-parallel length, and τ is the time interval over which melt accumulation has occurred. As both the ratio of residue mass to melt mass (η) and crust to mantle provenance (μ) are thought to be near 1:1 (Kay and Coira, 2009), the volume of mantle-derived melt calculated from the model should be equal to

the summed volume of seismically imaged volume of the magma chamber and the volcanic volume α (Fig. 2.4). This value is equivalent to the "volume addition rate per arc length" as described by Paterson and Ducea, 2015.

2.3.4 Uplift history from the volcanic record

We estimate the time history of surface uplift from magmatic thickening of the APVC crust by utilizing measurements of erupted ignimbrite dense rock equivalent volume since 11 Ma (Salisbury et al., 2011, Table 6). Using our topographic estimate of $\beta = 37$, we convert ignimbrite volume to plutonic volume and divide the plutonic volume by the approximate aerial extent of the APVC (40,000 km^2) to get a mean crustal thickness contribution. We convert the change in thickness to surface uplift assuming Airy isostatic compensation, and take the local gradient in uplift over time to estimate surface uplift rate. As our buried load model shows, the large wavelength of the APMB does not feel the effects of the flexural rigidity of the upper crust and thus an Airy approximation for our simplified uplift model is appropriate. Because mechanical processes in the crust will filter the power input from the mantle (e.g., de Silva et al., 2015), there is likely not a linear relationship between mantle melt production and surface eruption rates. However, the 6 Myr interval that defines the APVC flare-up may record the time variability of melt production (de Silva et al, 2015), so we average our uplift calculations over this change in volcanic volume (Fig. 2.6).

2.4 Results and discussion

In order to constrain the topographic signal associated with the presence of the APMB, we measure the long wavelength component of the topography in the

Central Andes and find that a high-amplitude, km-scale dome spatially coincides with the estimated bounds of the seismically imaged magma body (Fig. 2.1b, Fig. 2.2a). Here the seismic bounds of the APMB in Fig. 2.1b are delineated by the 2.9 km/s contour from the shear-wave velocity model of Ward et al., 2014 (Fig. 2.2d).

In cross section, the peaks of volcanoes can be seen superimposed on the long wavelength topographic dome of the APVC. The dashed line in Fig. 2.2a shows an envelope with an amplitude of 1 km drawn through the topographic maxima of the APVC along our cross section line. This is akin to looking at the long wavelength component of the raw topography; however, it is notable to see the signature reflected in the summits of the volcanoes that have been distributed across the APVC since the late Miocene. Visualized this way, one can observe the physiographic transition at the southern edge of the dome as the declining peaks of the APVC run into the high relief, fault-bounded blocks of the southern Puna (Fig. 2.1a, 2.2a).

The dome is also located within the bounds of a $<$ -300 (Prezzi et al., 2009) to -400 (Bonvalot et al., 2012) mGal Bouguer gravity anomaly, which roughly mirrors topography and suggests a thickened, isostatically supported crust directly below the dome (e.g., Beck et al., 1996) (Fig. 1b, Fig. 2b, Supplementary Fig. 1). Forward modeling of Bouguer anomalies with seismic constraints by Tassara and Echaurren, 2012, show that the depth to Moho and the lithosphere-asthenosphere boundary are separated by less than 10 km beneath the APVC, consistent with the idea of convective lithospheric removal. Additionally, although there is a nonzero free-air gravity anomaly along the Central Andes (Fig. 2.2c and 2.3), it does not change from the southern Altiplano to the southern Puna (Fig. 2.2c), which further suggests the Central Andes as a whole are roughly in isostatic balance.

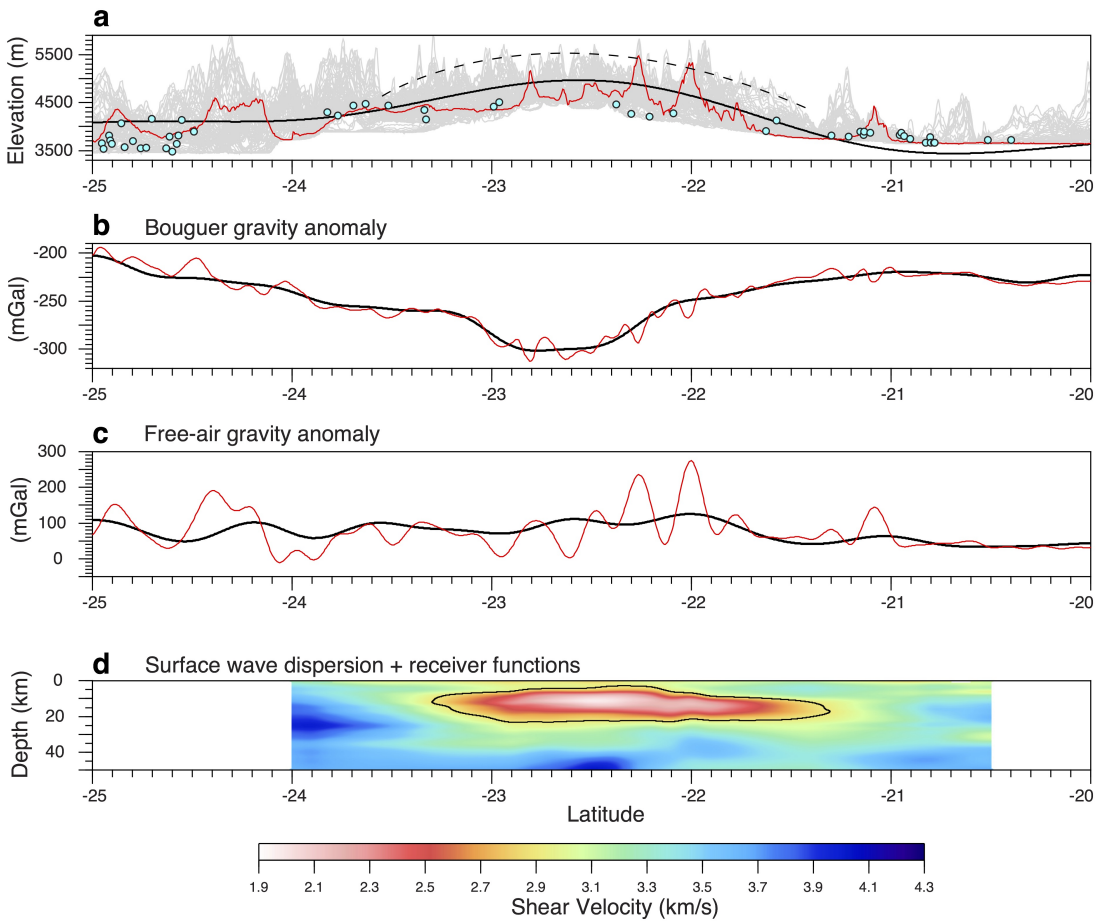

Figure 2.2: Cross-sections of various datasets through the study area along the 67.2° longitude line. Panel **a** shows a topographic swath profile (gray band), an exact topographic profile along the cross section line (red line), filtered long wavelength topography (black line), and median outcrop elevations (blue dots). **b** shows the filtered (black) and unfiltered (red) bouguer gravity anomaly from the 2012 World Gravity Model dataset. **c** shows the filtered (black) and unfiltered (red) free-air gravity anomaly from the AnGrav dataset. **d** shows the S wave velocity models of Ward et al., 2014.

Here the positive free-air gravity anomaly likely arises from the narrow width of the Central Andes (200 km) relative to the compensation depth (60 km), which may result in significant free-air edge effects within the APVC (e.g.,Fowler, 2004). Additionally, short wavelength (and thus flexurally supported) topography such as volcanoes appears to contribute to this signal (Fig. 2b). Regardless, Airy isostatic residual anomalies from the 2012 World Gravity Model are roughly zero at the APVC (Fig. 2.3), consistent with isostatically-supported topography.

A key question is whether the high topography of the APVC results from structural uplift or the deposition of volcanic material on the plateau surface (e.g.,Quade et al., 2014). We estimate the mean thickness of ignimbrite material above the APMB basement using the volcanic volume estimates of Salisbury et al., 2011, who report a total dense rock equivalent volume of 12,820 km^3. Over the 40,000 km^2 area of the APVC, roughly 20% consists of caldera basins where much of this material resides. Assuming an average caldera fill depth of 1.1 km, we estimate an average thickness of 120 m across the non-caldera basins. To verify this estimate, we map exposures of basement rocks proximal to our 67.2°W cross section line. The basement rocks underlying the late Neogene ignimbrites within the Central Andes are largely composed of the Paleozoic Antofalla terrane, an accreted crustal block consisting of metamorphosed igneous and sedimentary basin rocks associated with the Sunsás orogeny (Ramos, 2008). Figures 2.2 and 2.3 show the mean elevations for the mapped basement outcrops projected onto our cross section lines. Although exposures in general decline toward the interior of the APVC, the median outcrop elevations roughly track the rise observed in the topographic datasets and appear to define the level of topography just below the volcanoes (red lines, Fig. 2.2a and 2.3a). Lastly, evidence for a 1 km structural rise is also expressed in tilted forearc basin strata along the monoclinal

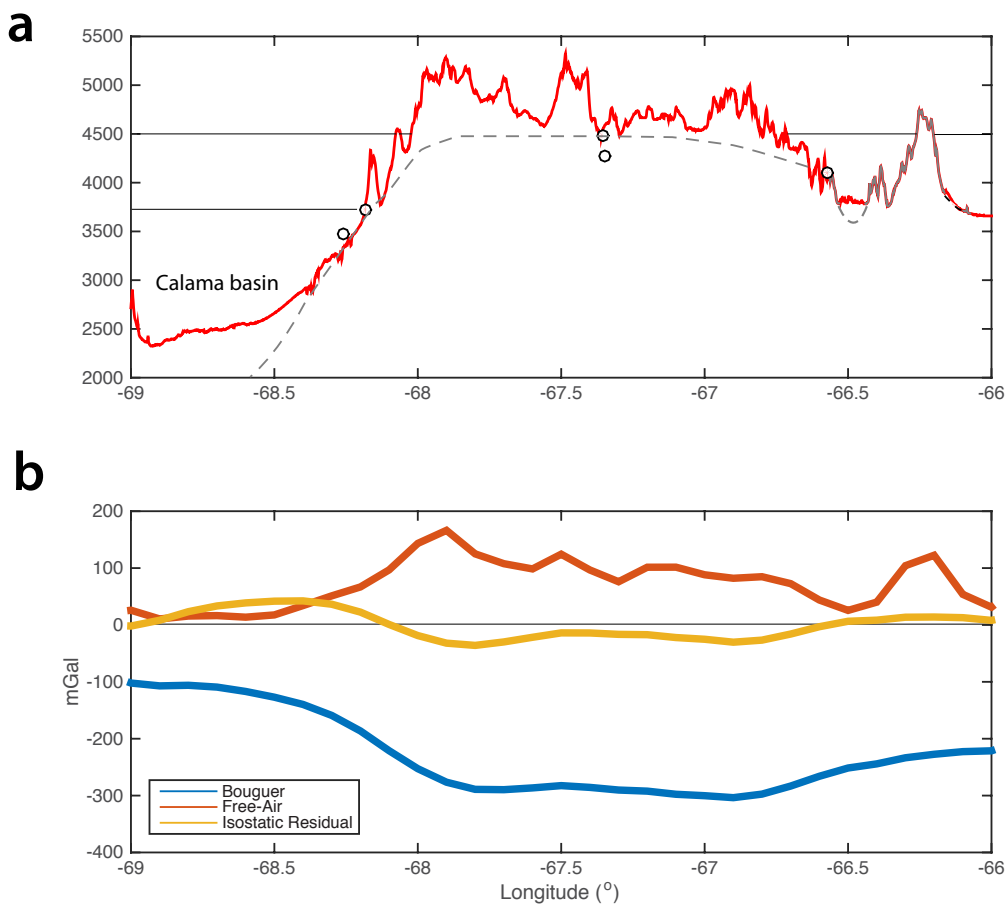

Figure 2.3: Latitudinal cross section along the 22.4° latitude line. **a** shows a topographic profile (red line) and isolated basement rock outcrop elevations (white dots, locations in Fig. 1b). The gray line represents a coarse estimation of the elevation of pre-11 Ma basement rock. It is solid where it is visible at the surface in the Eastern Cordillera, and is dashed underneath the APVC and the Calama basin to the west. Reference lines are at 3700 m (mean elevation of the southern Altiplano) and 4500 m (mean elevation of the Altiplano-Puna). **b** shows gravity anomalies along the cross section line. The free-air gravity anomaly mirrors the flexurally supported short-wavelength topography, and the negative Bouguer gravity anomaly roughly mirrors the long-wavelength topography. The lack of a significant Airy isostatic residual anomaly suggested that the topography of the APVC is isostatically compensated.

Table 2.2: Magma production rate calculations from isostatic model results.

H_b (m)	$\Delta\rho$ (kg/m^3)	W_i (km^3)	ξ_{Wi} $(km^3/km/Myr)$	β -	V_{apmb} $(\alpha * \beta)$
800	500	287,610	114	21	274,790
800	450	314,730	124	24	301,910
800	400	348,620	138	26	335,800
1000	500	358,580	142	27	345,760
1000	450	392,380	155	30	379,560
1000	400	434,640	172	33	421,820
1200	500	450,830	178	34	438,010
1200	450	493,330	195	37	480,510
1200	400	563,540	223	43	550,720

folds of the western slope of the Central Andes, where Jordan et al., (2010) find an increase in structural relief growth of 1.1 km from 20°-24°S since 11 Ma. Assuming an isostatically compensated crust as the gravity data suggest, we utilize the topographic signature of the APMB to calculate the contribution to crustal thickening by the addition of mantle melt at its base. To make this calculation we use a buried load isostatic model (e.g., Watts, 2001; Forsyth, 1985) which utilizes the surface response profile (topography) to calculate the depth of the initial buried load (Fig. 2.5). There are a number of assumptions that go into modeling this system as a buried load, namely that the density of the material entering the crust is the same as the crust itself. Obviously this is not the case as the asthenospheric melt will have a higher density than the overlying crust, so we take an average density of 2800 kg/m^3 for the crustal column and 3250 kg/m^3 for the density of the underlying asthenosphere (e.g., Prezzi et al., 2009). We approximate the segment of the lowpass-filtered topography associated with the APMB as a Gaussian curve with an amplitude of 1200 m and a full-width-at-half-maximum of 230 km (Fig. 2.5).

We then forward model the 1D root profile and calculate the volume of mantle

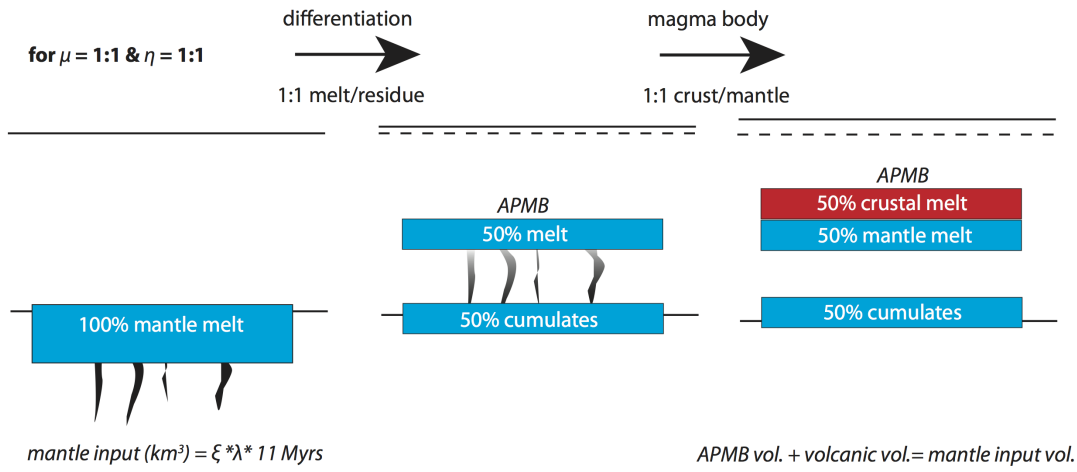

Figure 2.4: Schematic cartoon showing the chemical mass balance that relates mantle melt production to crustal thickening and pluton growth. For the case where the mantle melt:residue ratio and crust:mantle provenance ratios are both 1:1, as is thought to be the case for the APMB, the volume of mantle melt added to the base of the crust should be roughly equal to the size of the magma reservoir in the mid-crust. Figure modified from George Zandt and Kevin Ward (pers. comm.).

melt contribution to the crust assuming radial symmetry (e.g., Fig. 2.1b). This volume can be related directly to estimates of magma chamber volume assuming that both the ratio of crustal to mantle provenance and ratio of dense residue to melt mass are 1:1 (Ducea and Barton, 2007), which is seen in the chemistry of the APVC ignimbrites (Kay et al., 2010) (see Methods section for full description). The mantle melt volume estimate of 480,000 km^3 from the isostatic model is reasonably close to the seismically determined magma chamber volume of 530,000 km^3 from the 2.9 km/s velocity contour of Ward et al., 2014, given the inherent errors in estimating seismic and topographic volumes; however, our calculation is sensitive to both the prescribed density difference as well as the dimensions of the topographic profile used in our isostatic model, so we include a range of model runs adjusting these parameters in Table 2.2.

Taking into account both the seismic and topographic constraints on mantle

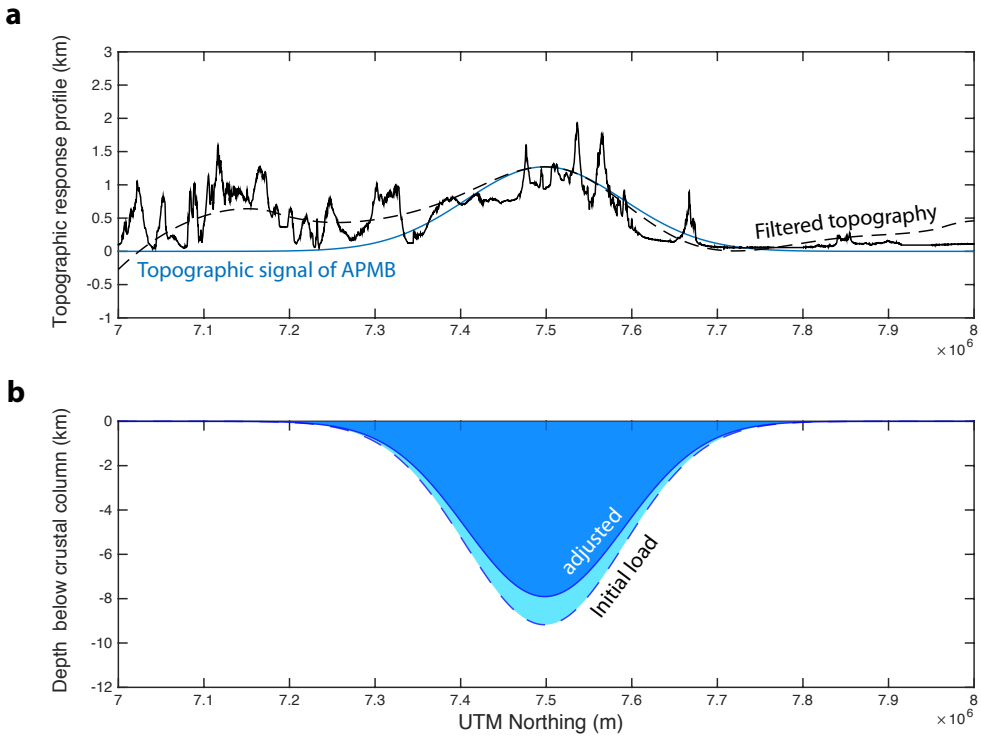

Figure 2.5: Buried load isostatic model results for the topographic dome overlying the Altiplano-Puna Magma Body. **a** shows the north-south raw topographic profile using 90 m SRTM data (solid black line), the long wavelength component of that profile (dashed black line, 175 km cutoff wavelength), and the Gaussian approximation of the topography related to the APMB (solid blue line). figure **b** shows the isostatic model profiles of the initial (light blue) and adjusted (darker blue) thickened crust beneath the APMB.

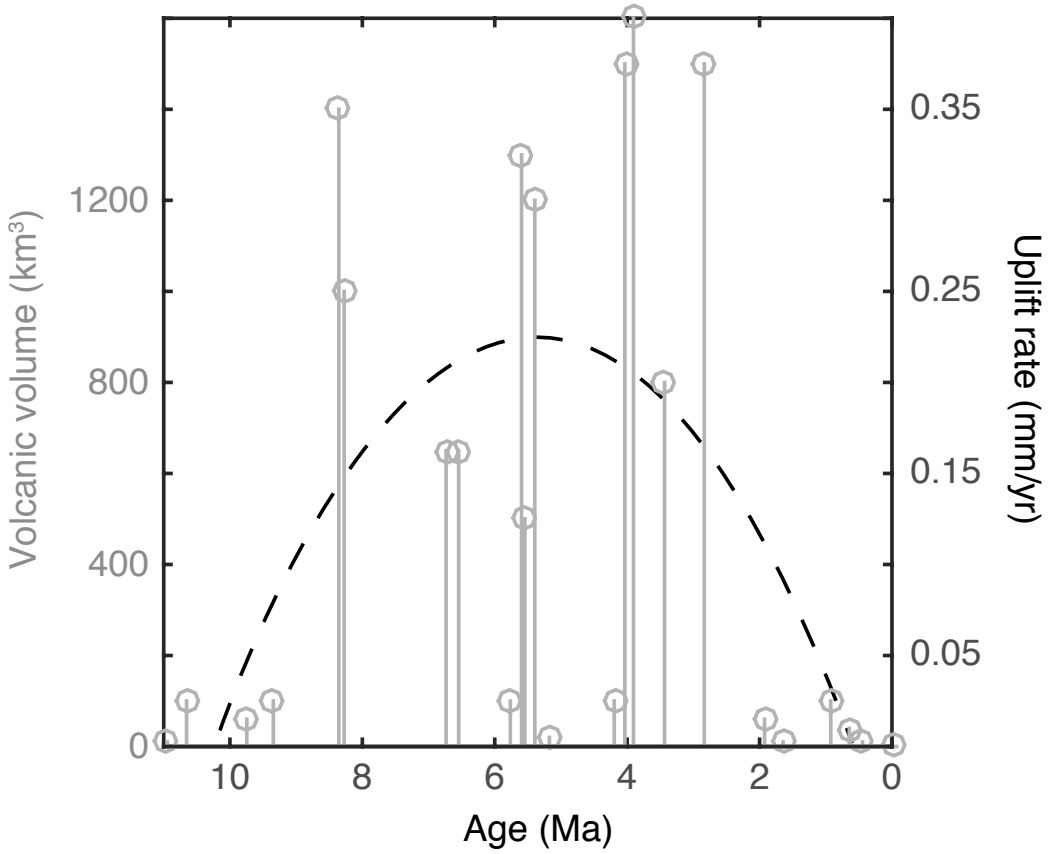

Figure 2.6: Estimated uplift rate from magmatic thickening of the crust since the onset of ignimbrite volcanism at 11 Ma. The gray bars show erupted volume (dense rock equivalent) from APVC ignimbrites (Data taken from Salisbury et al., 2011). The peak of the flare-up occurs from 9-3 Ma, and may reflect the phase of peak mantle power input to the crust (de Silva et al., 2015). Dashed black line represents an uplift trajectory through our modeled isostatic response to magmatic addition over the 6 Myr flare-up interval.

melt flux, we calculate plutonic:volcanic value of $\beta = 37$ and an arc mantle magma production rate of 200 km^3/km/Myr for the APMB (see Methods section and Table 2.2 for calculation details). The APMB growth rate appears comparable to the peak growth of the late Cretaceous Sierran flare-up (e.g., Paterson and Ducea, 2015), and closer to the magma production rates associated with intra-oceanic volcanic arcs and spreading ridges (Jicha and Jagoutz, 2015). Additionally, our topographic estimate of $\beta = 37$ is similar to geochemical estimates of $\beta = 30$ for the Sierran batholith (Paterson and Ducea, 2015). The 1 km of surface uplift gained over the 11 Myr of magmatic addition represents 1/5 of the total uplift of the Altiplano-Puna, with the rest being accomplished primarily through crustal shortening (Isacks, 1988; Allmendinger et al., 1997) and lithospheric removal (Kay and Coira., 2009). Given the volcanological evidence for episodic magmatism throughout the APVC flare-up (Salisbury et al., 2011), it is likely that surface uplift from magmatic addition was non-uniform over time. Though the individual 2 Myr-duration ignimbrite pulses that characterize the APVC flare-up likely do not record the time variation of mantle melt flux into the crust (e.g., de Silva et al., 2015), the peak eruption rates cluster from 9-3 Ma and do likely define the peak of mantle power input over the 11 Myr duration (Fig. 3). We convert the measured volcanic volume over this interval to a plutonic volume using our measured value of β and model the uplift rate from the Airy isostatic response to the magmatic addition (Figure 2.6). We find that mean uplift rate during the flare-up interval is approximately 0.2 mm/yr, about half the 0.4 mm/yr rates associated with lithospheric removal in the southern Altiplano from 16-9 Ma (Garzione et al., 2014).

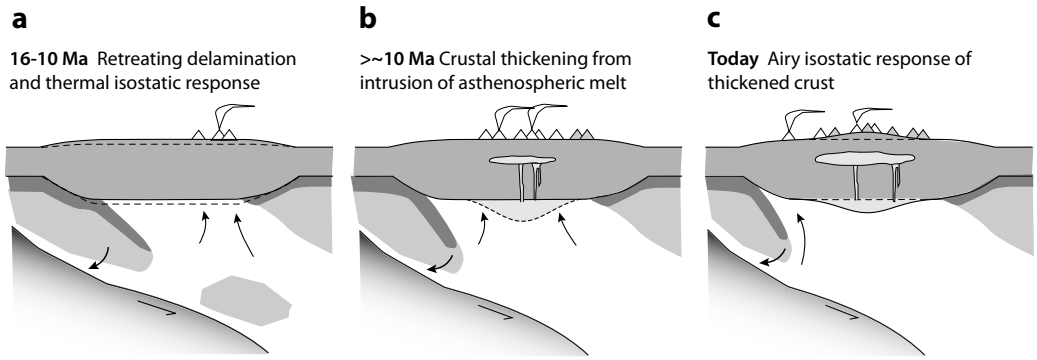

Figure 2.7: Cartoon depicting the time evolution of topography and subsurface geology along an East-West transect through the study area. **a** shows the westward retreating delamination of the mantle lithosphere beneath the Puna plateau and consequent Pratt isostatic response to the emplacement of warm (lower density) mantle asthenosphere beneath the crust (arching arrows). Back-arc volcanism also persists during this time. **b** depicts the influx of asthenospheric melt into the lower crust which constitutes an effective buried load. Airy isostatic compensation of this crustal loading from below leads to an increase in surface uplift in the Altiplano-Puna **(c)**.

2.5 Conclusions

We present a schematic cartoon illustrating our conceptual model for the growth of topography above the APMB since 10 Ma (Fig. 2.7), which builds off the models of Kay and Coira, 2009, and Beck et al., 2015. Beginning with the westward retreating delamination of a weak mantle lithosphere and dense lower crust after an increase in the dip of the subducting slab at 16 Ma (Kay and Coira, 2009), hot (low density) asthenosphere flows under the thickened orogenic crust causing uplift from the gain in gravitational potential energy (e.g.,Molnar and Stock, 2009) (Fig. 2.7a). Decompression melting of the thickened mantle wedge and elevated temperatures at the base of the crust facilitate crustal melting and the addition mantle-derived melts to the crust (Kay et al., 2010) (Fig. 2.7b), causing an additional Airy isostatic response (Fig. 2.7c).

Thus, in light of recent seismic constraints on the volume of partial melt in

the mid-crust (Ward et al., 2014), we argue that magmatic thickening of the crust represents a significant component of surface uplift in the APVC since 11 Ma. That the topographic response to building a batholith can be of similar magnitude to surface uplift from thinning the mantle lithosphere (e.g., Molnar and Stock, 2009; Pelletier et al., 2010) has implications both for interpreting the paleo-elevation history of the Central Andes as well as for geodynamical modelers seeking to understand the processes responsible for orogenesis and pluton growth in arc settings.

Chapter 3

Topographic constraints on magma accumulation below the Uturuncu and Lazufre volcanic centers in the Central Andes

3.1 Abstract

Geodetic surveys of Volcán Uturuncu and the Lazufre volcanic complex in the Central Andes of South America reveal sustained surface uplift from magmatic intrusion at depth. However, the decadal timescales of geodetic surveys are short relative to the timescales of magma chamber growth. Hence, from geodesy alone it is difficult to infer the deformation and hence magma accumulation history of these volcanoes. Here we combine data from InSAR, long wavelength topography, GPS and high-resolution topographic surveys of lake shorelines and rivers, and lava flow morphology to constrain the spatial and temporal evolution of magmatism at

Uturuncu and Lazufre. Near Uturuncu, dated lake shorelines show no evidence of tilting since 16 ka, and we find no evidence of deformation in the long wavelength topography. A lack of net surface displacement suggests that uplift related to a rising diapir must be less than a century old, or, more likely, magmatic inflation at Uturuncu is transient over millennial timescales and is therefore not recorded in the topography. At Lazufre we also find no evidence for sustained uplift recorded in late Pleistocene lake shorelines. However, the orientations of multiple dated lava flows suggest that the long-wavelength dome at the center of Lazufre's uplift has persisted since at least 300 ka. The dome's longevity indicates significant magma storage at depth, and therefore Lazufre is likely a highly evolved pre-caldera magmatic system. These two case studies demonstrate that combining geomorphic and geophysical datasets to extend the geodetic record back in time can help determine the style and magnitude of magma transport in volcanic systems.

3.2 Introduction

The relatively recent discovery of actively uplifting volcanoes in the Central Volcanic Zone of the Andes (14°-28°S) using InSAR geodesy (Pritchard and Simons, 2002) has spurred much research devoted to monitoring surface deformation and understanding the magmatic inflation processes that are thought to be driving these systems (e.g., Singer et al., 2014). The uplift patterns of Volcán Uturuncu in southern Bolivia (22°16'S, 67°11'W) and the Lazufre volcanic complex on the border of Chile and Argentina (25°18'S, 68°26'W) are particularly noteworthy as the 10-100 km footprint of their deformation is on the spatial scale of large caldera systems in the Central Andes (Fig. 3.1) (Pritchard and Simons, 2002; Sparks et al., 2008; Ruch et al., 2008).

Large silicic magma chambers tend to grow and evolve over much longer

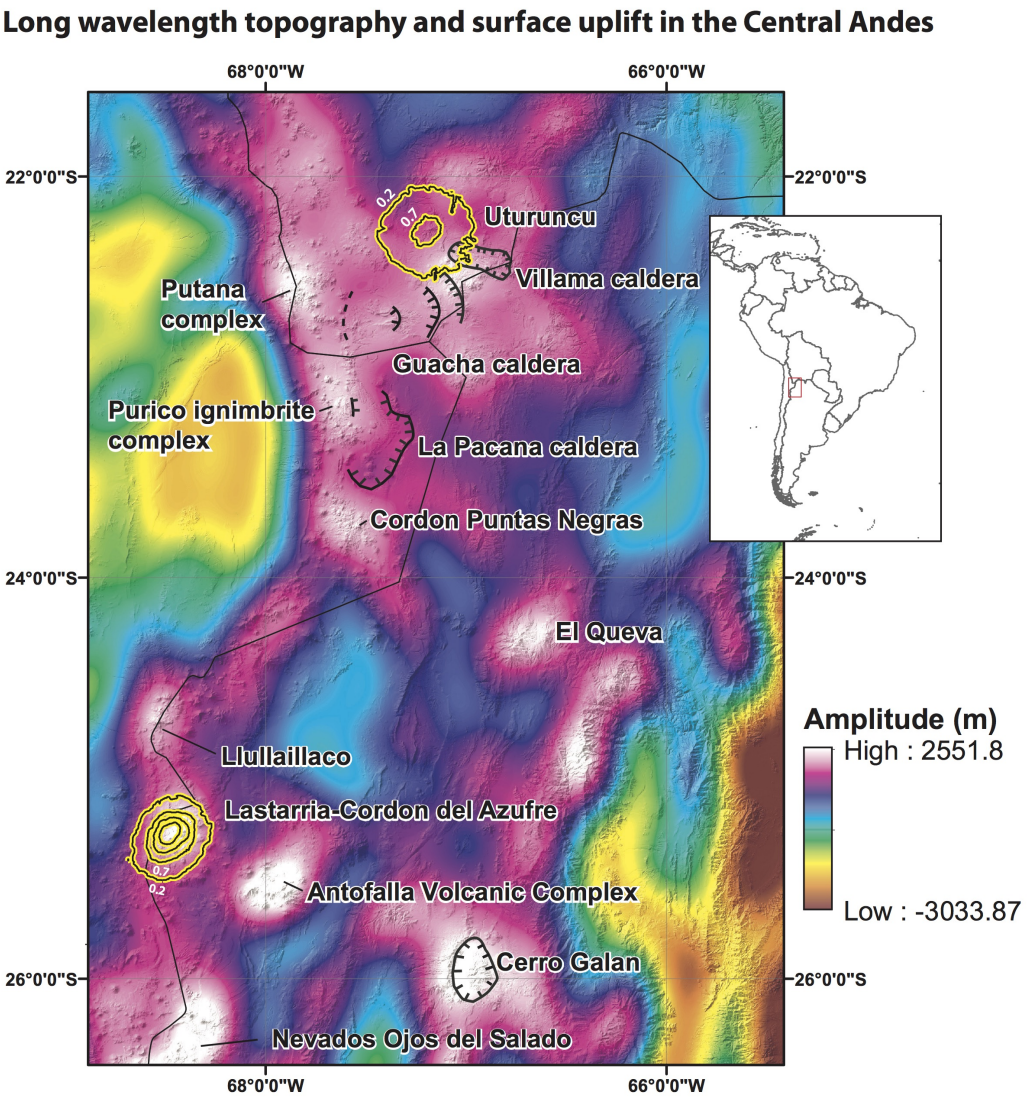

Figure 3.1: Overview map of the Central Andes showing modern surface displacement anomalies (yellow/black contours), caldera locations (black hatched lines), and long wavelength topography over a hillshade of the region. High amplitude, long wavelength anomalies tend to occur either at caldera locations or large volcanic complexes within the Central Andes. The uplift at Lastarria-Cordón del Azufre ("Lazufre") coincides with a long wavelength dome, however the uplift at Uturuncu appears at a relative topographic low.

timescales (10^4-10^5 yrs) than can be captured by decade-scale geodesy (Vasquez and Reid, 2002; Lindsay et al., 2001), and therefore the picture of magmatic evolution gleaned solely from satellite data is often incomplete. Geomorphic processes operate over timescales similar to magma chamber growth, and thus topography has the potential to offer additional constraints on the growth history of large volcanic systems. Tectonic geomorphology as a field has developed many tools devoted to tracking the paleo-geodetic history of landscapes (e.g., Burbank and Anderson, 2011), and lake shorelines and river deposits and their characteristic morphologies have proven to be effective strain markers in tracking surface deformation from magmatism specifically (e.g., Pierce et al., 2002). Additionally, the large spatial and temporal scales associated with magmatic systems imply that signatures of deformation may even appear in long wavelength topography (e.g., Froger et al., 2007; Gregg et al., 2012). Figure 3.1 shows that many volcanic complexes in the Central Andes correlate with long wavelength topographic anomalies. Notably, the 70 km diameter uplift field at Uturuncu appears to be centered on the edifice of the 15 km wide volcano with no underlying long wavelength anomaly (Fig. 3.2a), while the 60-70 km deformation field at Lazufre is correlated with a long wavelength dome and no central stratovolcano (Fig. 3.2b). This simple observation suggests either that Lazufre and Uturuncu are at differing stages in their evolution, or that they are operating by different magmatic processes entirely.

In this paper we integrate data from satellite geodesy, paleo-geodetic measurements from the geomorphology of lakes, rivers, and lava flows, and bulk topographic characteristics to infer the spatial and temporal scales of surface uplift at Uturuncu and Lazufre. In doing so, we hope to provide observational constraints that allow differentiation between end-member models of how magma

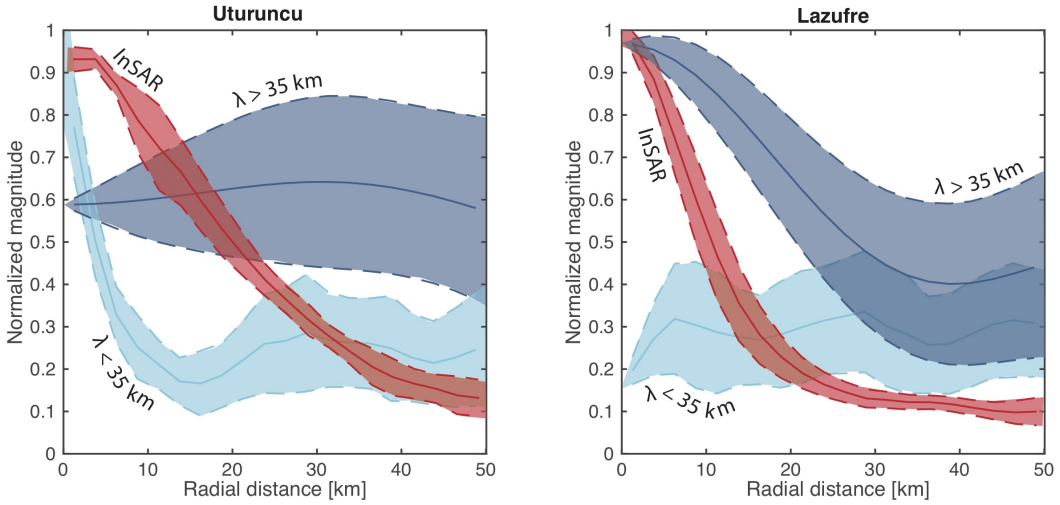

Figure 3.2: Normalized radial profiles of line-of-sight (LOS) velocity and the long wavelength (>35 km) and short wavelength (< 35km) components of topography at Uturuncu and Lazufre. LOS velocity data are from stacked interferograms created along Envisat descending track 282. Topography data comes from the global 90 m SRTM dataset. Solid lines represent the average radial value as a function of distance from the peak LOS velocity anomaly, and dashed lines represent $\pm 1\sigma$.

is being transported, stored, and potentially erupted at these sites. Below we describe the background of each case study and the hypotheses that our methods will be able to test.

3.2.1 Volcán Uturuncu

Uturuncu is a 6,008 m high Pleistocene stratovolcano located in southern Bolivia within the Altiplano Puna Volcanic Complex (APVC), an extensive region of silicic calderas and voluminous ignimbrite sheets from 21°S-24°S (de Silva, 1989). It was primarily active from 1050 ka to 250 ka and has yielded 50 km^3 of high-K dacite and silicic andesite from effusive eruptions over its lifetime (Muir et al., 2015; Sparks et al., 2008). Recent and rapid uplift at Uturuncu was first discovered through an InSAR investigation by Pritchard and Simons (2002), who documented a peak uplift of >1 cm/yr since the onset of InSAR measurements in the region in 1992. Estimated source depths from inversion of the geodetic data suggest that the deformation could be coming from magma inflation at the top of a large regional zone of partial melt known as the Altiplano Puna Magma Body (APMB), which is thought to be the magmatic source for the flare-up of ignimbrite volcanism in the APVC (Zandt et al., 2003). Recent swarms of seismicity are additionally thought to reflect pressurization of upper crustal rocks by magma inflation at depth (Jay et al., 2011). More recent InSAR investigations using multiple look angles (Fialko and Pearse, 2012; Henderson et al., 2013, 2015) have shown evidence of a deflationary moat along the outer edges of the uplift field at Uturuncu. Two primary end-member models have been put forward to account for simultaneous inflation and peripheral deflation: lateral migration of melt and growth of a diapir from the APMB (Fialko and Pearse, 2012), or upward migration of melt out of a deeper (55-80 km) reservoir and

into to the top of the APMB (Henderson and Pritchard, 2013). Both gravity (del Potro et al., 2013) and magnetotelluric (Comeau et al., 2015) surveys show a low density, melt-rich body at the top of the APMB; however, the lack of spatial resolution of these techniques at depths below the APMB prevent them from being able to uniquely identify the mode of magma transport at Uturuncu. Integrated over the 10^5-10^4 year timescales that are relevant to the growth of large silicic magma chambers, however, these two models yield different predictions of long-term surface uplift. As diapirism is a buoyancy-driven viscous process and should be relatively continuous in time (e.g., Burov et al., 2003), we expect there to be a record of long-term surface uplift at Uturuncu. Alternatively, if Uturuncu is experiencing transient pulses of inflation from magma flux between shallow and deep reservoirs, separated by periods of relative quiescence, then we may not expect to see a record of long-term net surface uplift (e.g., Pierce et al., 2002). The systems of rivers and Pleistocene lakes that flank Uturuncu (Fig. 3.3) provide constraints on surface deformation going back tens of thousands of years; therefore we may be able to use the rich paleo-geodetic record to unravel the long-term relationship between magmatism and surface deformation here.

3.2.2 Lazufre

The name "Lazufre" is a portmanteau that joins together the names of Lastarria Volcano (25°10'S 68°30'W) and Cordón del Azufre (25°20'S 68°31'W), two 0.6-0.3 Ma volcanoes on the periphery of a rapidly uplifting 60 km diameter elliptical zone that has accelerated to 2.5 cm/yr since 2005 (Naranjo and Cornejo, 1992; Froger et al., 2007; Ruch et al., 2008; Henderson and Pritchard, 2013). On the basis of InSAR inversions, the source of deformation is thought to be either an inflating sill or a flat topped magma chamber at 10 km depth (Ruch et al, 2008).

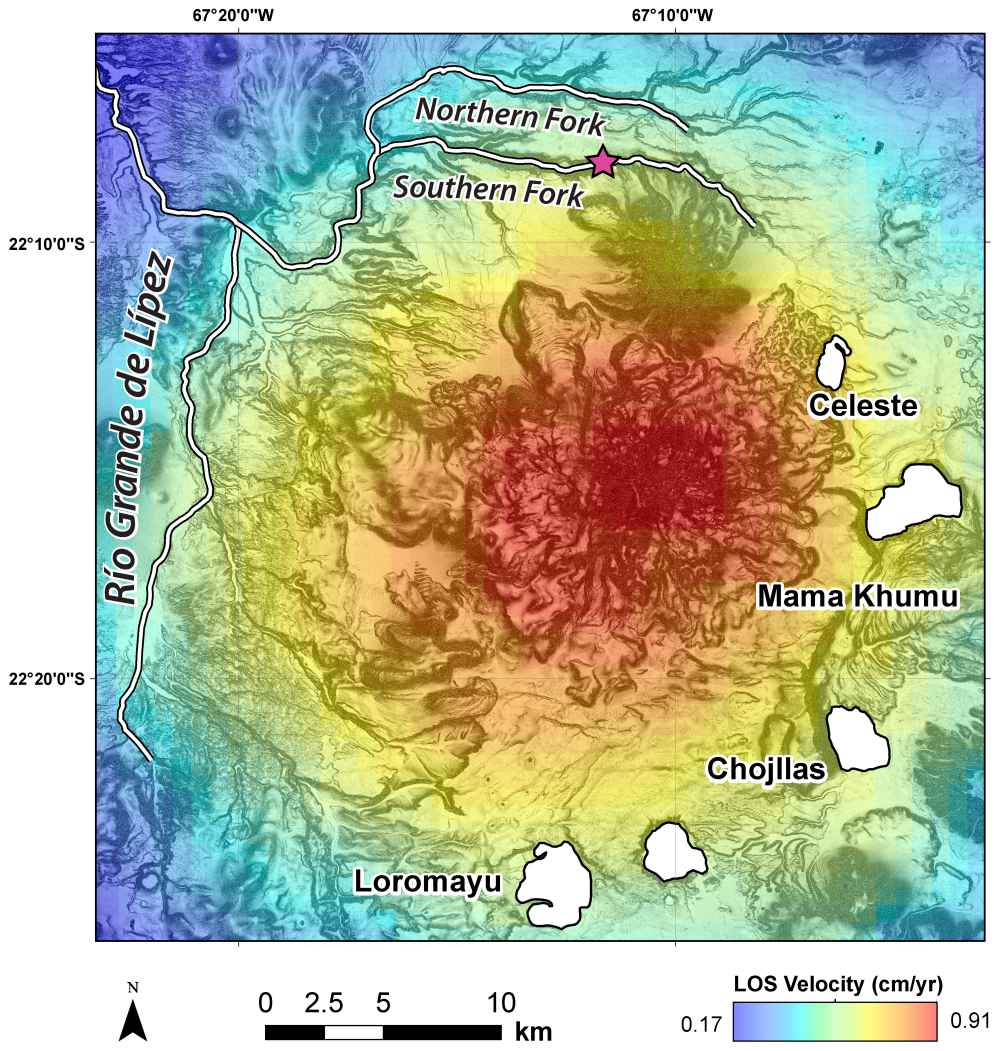

Figure 3.3: Overview map of the Uturuncu study area. InSAR surface displacement rates are shown in color beneath a slope map created with our photogrammetry-derived DEM. Prominent Pleistocene lakes are shown in white, as are tributaries of the Rio Grande de Lipez. The pink star denotes the location of a knickpoint above the alluviated reach of the "Southern Fork," which spatially coincides with a change in planform orientation of the river as it arcs around the adjacent, older Cerro San Antonio.

Observations of regional vent orientations and faults suggest the elliptical shape of Lazufre may be due to a regional maximum horizontal compressive stress oriented NW-SE (Ruch and Walter, 2010). The uplift field at Lazufre is not centered on any particular volcano, but rather on a long wavelength, 70 km diameter and 500 m high topographic dome (Froger et al., 2007; Figs. 3.1 and 3.2). The dome is flanked by a series of smaller Pleistocene volcanoes, all of which are hypothesized to be part of a larger pre-caldera system (Froger et al., 2007). Implicit in this hypothesis is the idea that the magma reservoir beneath Lazufre was active during the formation of the peripheral ring volcanoes, and therefore a key test is whether the dome pre-dates these eruptions. A primary goal of this study is then to constrain the rate and timing of dome growth at Lazufre using a variety of geomorphic tools in order to better understand its potential as a rapidly inflating pre-caldera system.

3.3 Methods

3.3.1 High-Resolution DEM Generation

Mapping lake shoreline deposits requires a DEM of sufficient resolution to resolve the subtle slope breaks that characterize these features. In areas like the Central Andes where LiDAR data are difficult to obtain and abundant vegetation is not an issue, satellite photogrammetry can produce digital elevation data of comparable resolution for a significant fraction of the cost. We acquired 0.5 m resolution, stereo-paired Worldview-1 satellite imagery for a 35 x 35 km zone containing Uturuncu and its surrounding area and produced a DEM using the open source StereoPipeline software developed by NASA (Moratto et al., 2010). To produce an absolute DEM we corrected relative elevations using 90 m SRTM

data. To validate the DEM elevations we then compared them to high-precision campaign GPS measurements (del Potro et al., 2013) as well as our own kinematic dGPS surveys (Fig. 3.4). There is generally very good agreement between the campaign GPS data and the Worldview DEM, with a RMSE of 1.4 m including the kinematic dGPS surveys, and 1.0 m without (Fig. 3.4b). Figure 4c shows a zoomed-in comparison between the kinematic GPS data and the DEM data that indicates a slight bias toward higher GPS elevations at high SRTM-corrected elevations, as well as some noise that produces horizontal excursions on the 1:1 line. These excursions are due to the fact that the photogrammetry algorithms have difficulty correlating imagery with steep slopes, which leads to the generation of noise toward the summit of Uturuncu as well as the steep-sided boundaries of Laguna Mama Khumu.

3.3.2 Topographic Analysis

We use three different methods of topographic analysis to measure surface deformation in response to magmatic uplift at Uturuncu and Lazufre. As the modern uplift fields are relatively long wavelength, we examine the spatial correlation between uplift and various wavelengths of topography (e.g., Froger et al., 2007). Additionally, we utilize the well-preserved erosional and depositional landforms produced by both lakes and rivers within our study areas as topographic strain markers. Below we describe our topographic and geomorphic approaches to constrain long-term surface uplift.

3.3.3 Radial Topographic Profiles

To look for spatial correlations between topography and the radial patterns of surface uplift, we stack radial topographic profiles outward from the local maxima

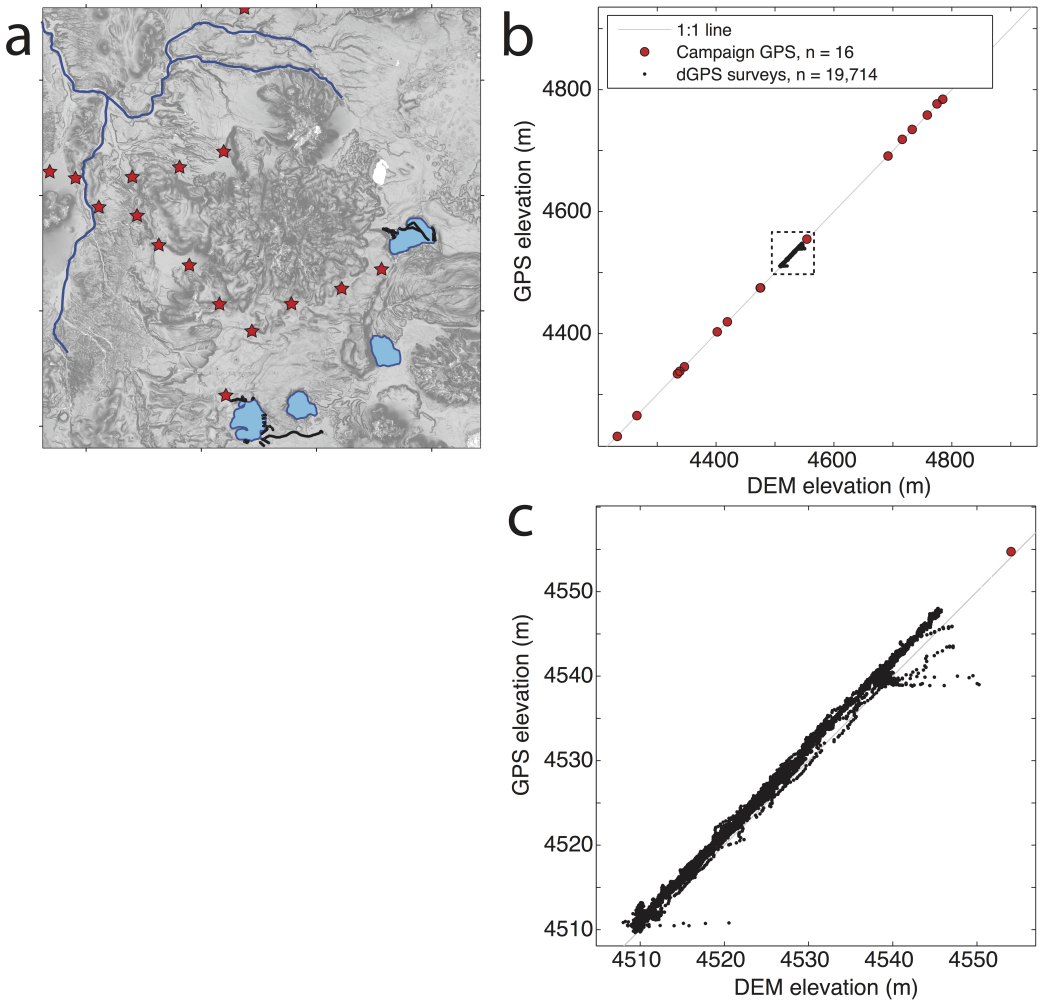

Figure 3.4: A comparison of campaign GPS and photogrammetry-derived DEM elevations across the study area. Panel **a** shows the location of campaign GPS surveys from del Potro et al. (2013) (red stars), prominent lakes and rivers around Uturuncu (blue blobs and lines), and differential GPS surveys from this study (black dots). **b** is a plot of GPS elevation vs. DEM elevation along a 1:1 line. **c** is a zoomed in look at the dGPS data from Laguna Mama Khumu and Laguna Loromayu, which fall slightly above the 1:1 line at higher elevations.

of the Line-of-sight (LOS) velocity field at both Uturuncu and Lazufre (e.g., Henderson et al., 2015; Froger et al., 2007) (Fig. 3.2). We do this for both long and short wavelength topography by taking the fourier transform of a 90 m SRTM DEM and applying a lowpass filter with a cutoff wavelengthof 35 km. We choose 35 km as a cutoff wavelength because it is larger than the wavelength of an individual arc volcano (15 km) and smaller than the wavelength of the modern uplift field (70 km) at both study areas.

3.3.4 Lakes as tiltmeters

The bell-shaped uplift patterns at Uturuncu and Lazufre produce uplift gradients radially away from their peaks (e.g., Figures 3.1 and 3.3). Thus, any planar surface subjected to this forcing will be tilted outward over time. Lake shorelines make excellent strain markers as they represent equipotential surfaces and are thus horizontal at the time of their formation. Using both field surveys and high-resolution topographic data from the DEM we produced, we map shorelines along the lakes within the modern uplift field at Uturuncu and Lazufre (Figs. 3.5 and 3.6). We then radially project shoreline elevations outward from the peak in LOS velocity. The high resolution of our photogrammetry-derived Worldview DEM allows for remote mapping of paleo shoreline features (Fig. 3.7). The subtle break in slope that characterizes a shoreline inner edge (a proxy for lake level during the period of shoreline cutting) becomes apparent in a slope raster of the elevation data (e.g., Fig. 3.7). We use the standard slope algorithm in ArcGIS to calculate the local 2D gradient of the topography. We then map inner edges directly on the slope map for Laguna Celeste, Laguna Mama Khumu and Laguna Chojllas (Fig. 3.3).

During our field campaign we also surveyed lake shoreline elevations using

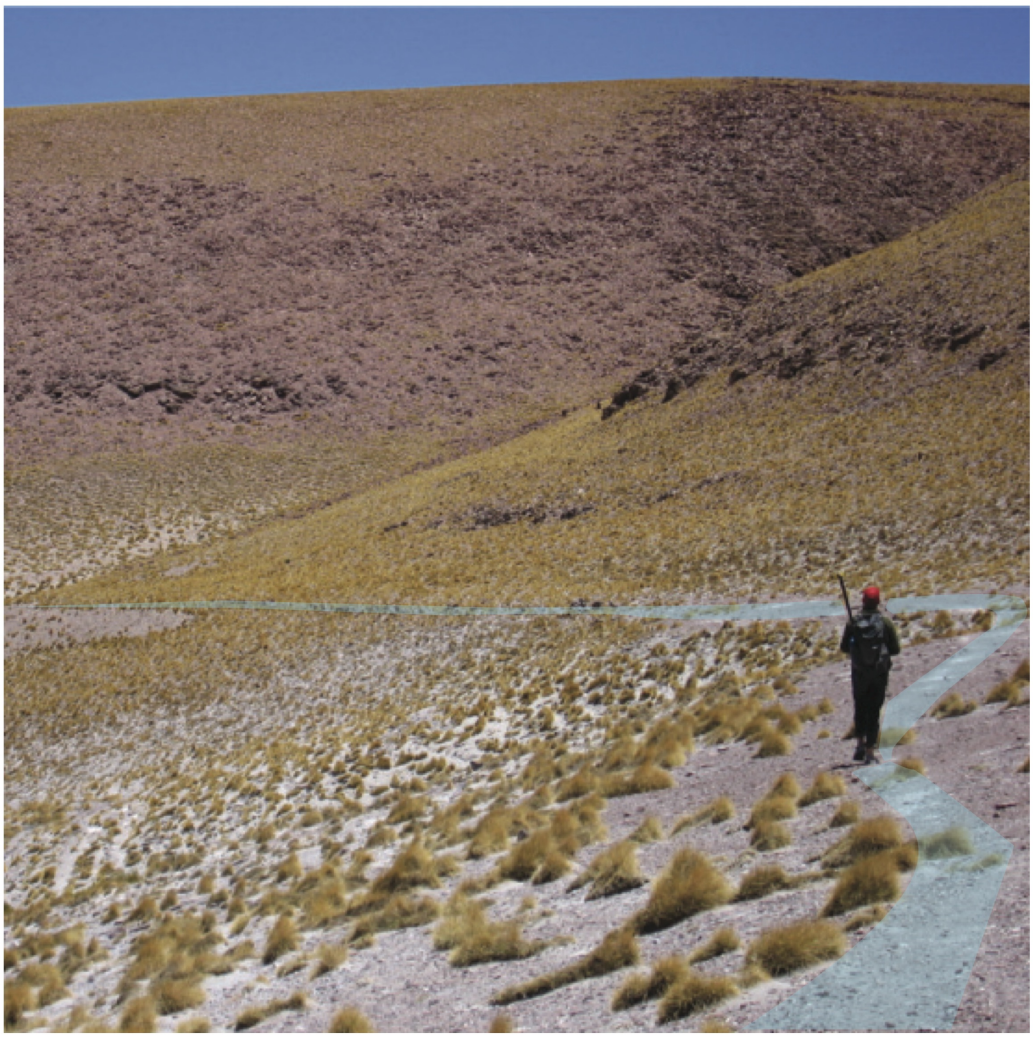

Figure 3.5: Photo looking to the east along the southern shore of Laguna Mama Khumu. A prominent strandline is highlighted in translucent blue. To survey shoreline elevations at Mama Khumu, we walked along them with a kinematic differential GPS receiver mounted on a pole in a backpack. Though in this image the pole is slightly askew, vertical uncertainties in elevation are on the order of 50 cm with this method.

a kinematic differential GPS (dGPS) with Trimble Terrasync software. Given its favorable orientation relative to the active uplift field and the clarity of its geomorphology, we focused our survey efforts at Uturuncu along Laguna Mama Khumu (Fig. 3.3). Shoreline inner edges and delta fronts (another proxy for water level, e.g. Gilbert, 1890) are present at both the proximal and distal edges of the lake, allowing us to walk along these features with the dGPS (Fig. 3.5). To allow for direct comparison between the field and remote surveys, we extract DEM elevations from the field-mapped shoreline traces at Laguna Mama Khumu (Fig. 3.8b).

At Lazufre, only one lake (Laguna de la Azufrera) is proximal to the modern uplift field; however, its position at the outer edge of the uplift field means it is likely not experiencing a significant amount of deformation. Additionally, because its long axis is roughly perpendicular to the uplift gradient it does not experience significant tilting (Fig. 3.9). However, it is within the bounds of the long wavelength topographic anomaly (Fig. 3.1). Much like the lakes surrounding Uturuncu, Laguna de la Azufrera has two prominent paleo shorelines (Fig. 3.10). Additionally, the east shore of Azufrera has a well-expressed beach ridge that runs parallel to the uplift gradient that we surveyed along its entire length in the field using kinematic differential GPS (Fig. 3.9a).

3.3.5 Rivers

River longitudinal river profiles can also serve as long wavelength recorders of surface deformation. At Uturuncu, three prominent tributaries of the Rio Quetena flow northward past the volcano into the Uyuni basin (Fig. 3.3). Valley bottoms along these drainages are typically comprised of fluvial gravels, and their margins are often confined by near vertical bedrock walls (typically

volcanic deposits) (Fig. 3.11). Presently, however, the floodplains are typically comprised of wetlands with bunch grasses and small, anastomosing channels (Fig. 3.11). The presence of wetlands and the small size of streams suggest that rivers are currently underfit relative to their valleys around Uturuncu. River channel change in gravel bedded rivers is driven by the divergence in sediment transport capacity downstream, which itself is governed by channel slope. Hence, tilting of alluvial channels can drive incision or aggradation depending on the orientation of the channel relative to the tilt (Ouchi, 1985). The apparent inability of the rivers around Uturuncu to transport their underlying gravels (as indicated by wetlands at present in these channels) implies that the channels are likely not dynamically responding to any surface perturbations. In the Atacama basin to the west of Uturuncu, Nester et al. (2007) dated buried woody debris along fluvial terraces to show that material was last being transported at this location during the Tauca highstand at 16-13 ka. If channels at Uturuncu have been dormant for an equivalent length of time, then the longitudinal river profiles of the Rio Quetena tributaries may be passively responding to surface uplift over this timescale without readjusting their profiles (and hence erasing the signature of deformation). Therefore, we hypothesize that their longitudinal profiles should directly reflect the uplift field and provide valuable strain indicators over this time period. Longitudinal profiles along Uturuncu were mapped by hand in ArcGIS using our high-resolution Worldview DEM. As the presence of wetlands within channels produces many anastomosing streams and frequently obscures channel thalwegs, the valley axis was used as a best approximation of the thalweg. Both elevation and InSAR LOS velocity data were extracted at points along the valley axis profiles. Elevation data were extracted at every meter, and InSAR data were interpolated to the smaller grid size of the DEM.

3.3.6 Mapping lava flow orientations at Lazufre

At Lazufre, the high degree of internal drainages created by overlapping lava flows coupled with the extremely arid conditions make for a conspicuous lack of through-going river networks. Therefore, we omit any analysis of drainage networks surrounding Lazufre and instead use the quaternary lava flows themselves to constrain the timing of uplift. If the lava flows radiate outward from the peak of the long wavelength topography, then the topography was likely present before the flows erupted. If the flow directions are de-correlated from the long wavelength topography, however, that suggests the doming occurred after they erupted. This simple hypothesis is complicated by the fact that short wavelength features such as individual volcanoes and neighboring lava flows can influence flow direction, so we limit our analysis to flows greater than 5 km in length. We map the orientation of each lava flow by mapping flow ridges from satellite imagery within ArcGIS. As flow ridges form perpendicular to flow direction (Fink, 1980), we trace lines orthogonally to each observed ridge train.

3.3.7 Geochronology

Calculating rates of surface deformation using lake shorelines requires knowledge of the shoreline ages in addition to their displacement. Though the lake level history of the Uyuni and Poopo basins to the north of Uturuncu are well understood (e.g., Placzek et al., 2006), given the local hydrologic conditions and glacial history of Uturuncu (Blard et al., 2014) it is unclear how the large lake level changes in the Altiplano translate to these smaller, high elevation basins. To constrain the ages of prominent paleo shorelines along lakes that flank Uturuncu, we dated two well-preserved beach terraces on the northern shore of Laguna Loromayu using optically stimulated luminescence (OSL) (Fig. 3.6). Within each

beach terrace deposit we dug 1m deep pits and took two unique samples from sub-horizontal beds of coarse to fine sand at different depths (Fig. 6c, Table 3.1). Samples were processed at the Utah State University Luminescence Laboratory to extract quartz sand for analysis following the single-aliquot regenerative dose (SAR) protocol (e.g., Murray and Wintle, 2000) and calculated using the early background subtraction method of Cunningham and Wallinga (2010) and the Central Age Model of Galbraith and Roberts (2012). Samples for environmental dose rate determination were analyzed for radioisotope concentration using ICP-MS techniques (Table 1) and converted to dose rate following the conversion factors of Guérin et al. (2011). Sediments collected in air-tight containers were dried to determine in-situ water content. Contribution of cosmic radiation to the dose rate was calculated using sample depth, elevation and latitude/longitude following Prescott and Hutton (1994). Total dose rates were calculated based on water content, radioisotope concentration, and cosmic contribution (Aitken, 1998).

3.4 Results

3.4.1 Uturuncu

Shoreline OSL ages at Laguna Loromayu

The OSL ages for the two prominent beach terraces at Laguna Loromayu range from 13-17 ka, consistent with the Tauca highstand seen in the Poopo and Uyuni basins of the Altiplano (e.g., Placzek et al., 2006) (Fig. 3.12, Table 3.1). This timing also corresponds to a period of rapid glacial retreat signaled by a rising equilibrium line altitude (ELA) at Uturuncu (Blard et al., 2014) (Fig. 3.12). Interestingly, the higher terrace at 4730 m has a lower combined age (16.6 +/-

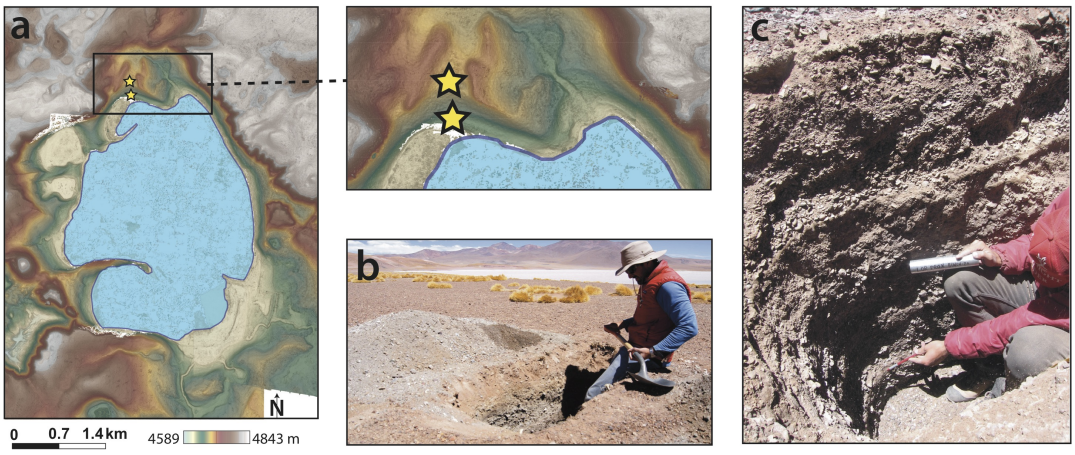

Figure 3.6: Locations and images of our geochronology sample sites on the northern shore of Laguna Loromayu (Fig. 3). **a** is a shaded elevation map of Loromayu from our high resolution DEM, and the yellow stars show the locations of our OSL pit locations on each of the two prominent beach terraces that can be seen in the inset map. **b** is a field photo of our lower sample location (Lor-1a and Lor-1b) during the pit excavation. c shows a photo of the stratigraphy within the pit, which consists of alternating layers of sub-planar bedded sand and gravel.

3.3 ka) than the lower 4715 m terrace (14.3 +/- 2.8 ka). This signals that the rise and fall of lake levels must have occurred rapidly in order to preserve the lower shoreline, which is consistent with the rapid shoreline ascent and descent seen during the Tauca highstand in the Uyuni basin (Placzek et al., 2006) (Fig. 3.12).

Deformation timescales at Uturuncu from lake surveys

At Uturuncu, none of the surveyed shorelines show evidence for sustained tilting. Figure 3.7 shows mapped shorelines and radial projections from Laguna Celeste, Laguna Mama Khumu, and Laguna Chojllas. The pink lines within the lower panels of Figure 3.7 represent the amount of tilting expected at each lake assuming the modern uplift rate has been consistent since the Tauca highstand (16 ka). Table 3.2 shows the average slopes in the direction of tilting and tilt rates

Sample	USU-#	% K	Rb (ppm)	Th (ppm)	U (ppm)	Num. of Aliquots1	Equivalent Dose (Gy)2	Dose Rate (Gy/ka)	OSL Age (ka) Âś 2 se
Lor -1a	USU-957	1.86	126.5	12.9	2.8	20 (36)	58.33 Âś 3.52	3.48 Âś 0.16	16.77 Âś 1.89
Lor -1b	USU-958	1.70	120	11.4	3.3	20 (34)	56.34 Âś 4.78	3.43 Âś 0.16	16.44 Âś 2.09
Lor -2a	USU-959	1.82	105.5	7.7	2.3	19 (34)	47.72 Âś 5.52	3.11 Âś 0.14	15.36 Âś 2.29
Lor -2b	USU-960	2.35	156	15.3	3.7	29 (58)	58.61 Âś 6.74	4.41 Âś 0.20	13.29 Âś 1.98

Table 3.1: OSL age information. Age analysis using the single-aliquot regenerative-dose procedure of Murray and Wintle (2000) on 2-mm small-aliquots (SA) of quartz sand. Number of aliquots used for age calculation, number of aliquots measured in parentheses. Rejection of aliquots follows standard rejection criteria (see Rittenour 2005 for example). Equivalent dose (DE) is calculated using the early background subtraction method of Cunningham and Wallinga (2010) and the Central Age Model of Galbraith and Roberts (2012), error on DE and age is 2-sigma standard error.

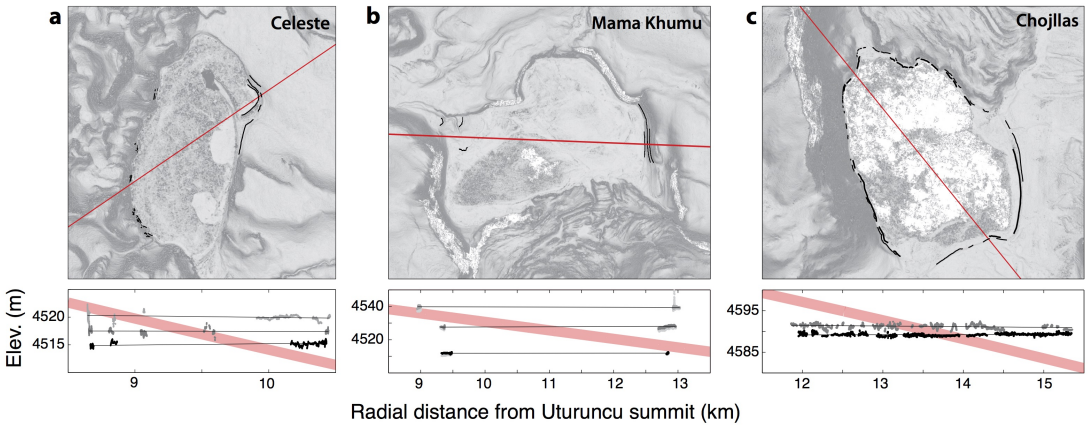

Figure 3.7: Shoreline elevation data from lakes at Uturuncu. Upper panels show mapped shorelines (black lines) and a radial projection line (in red) from the summit over a slope map derived from our 0.5 m DEM. Lower panels show radial projections of shoreline elevations away from the summit. Thin black lines are best-fit lines through mapped elevations of each shoreline, and the pale red lines represent a prediction of tilting for each lake estimated by integrating the modern uplift field back to the Tauca highstand at 16 ka. In panel **b** the map traces are taken from GPS surveys in the field, and elevations from both GPS and the DEM are plotted in the lower panel (DEM in the background in light grey). The GPS data overlap the DEM data nearly completely, with a small excursion on the distal margin of the upper shoreline. This likely occurs because of DEM noise due to the steep sidewalls of the basin, but in general the overlap between the datasets suggests the DEM is accurately representing absolute elevations.

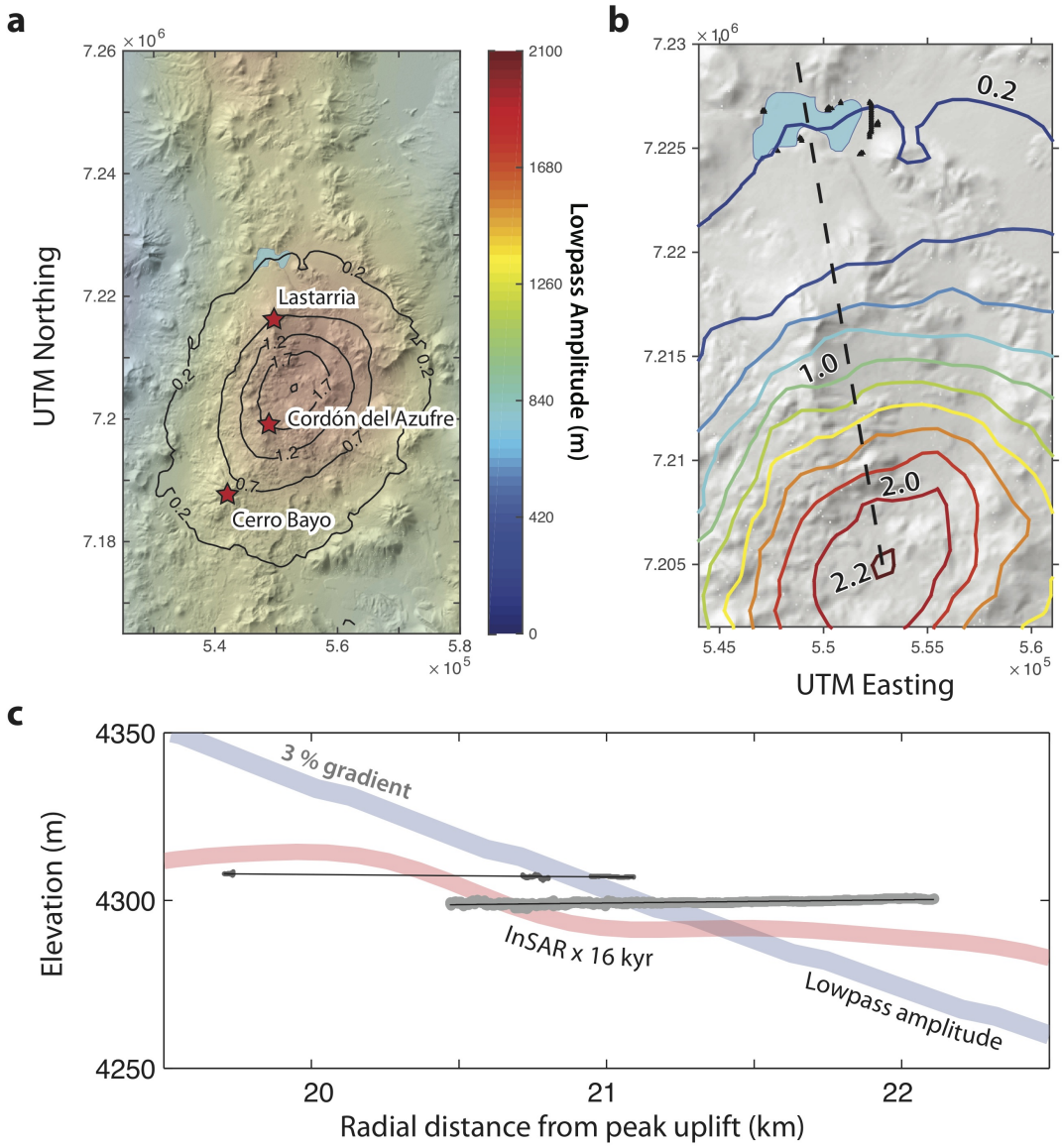

Figure 3.8: Long wavelength topography, surface uplift, and shoreline levels at Lazufre. Panel **a** shows an SRTM 90 m hillshade colored by the long wavelength topographic amplitude. Contours are LOS velocities derived from Envisat track 282 descending interferogram stacks (Henderson et al., 2015). textbfb shows a zoom in of a with kinematic GPS data collected along shorelines (black triangles) and a radial projection line from the maximum uplift (dashed line). The same InSAR data are in colored contours with a 0.2 cm/yr interval. **c** shows a radial projection of shoreline survey data along the projection line in **b** against long-term uplift predictions. The red line represented a scenario of constant uplift at modern rates going back to the Tauca highstand (16 ka), and the blue line is a profile through the background long wavelength topography. Thin black lines are best-fit lines through the survey data for each shoreline

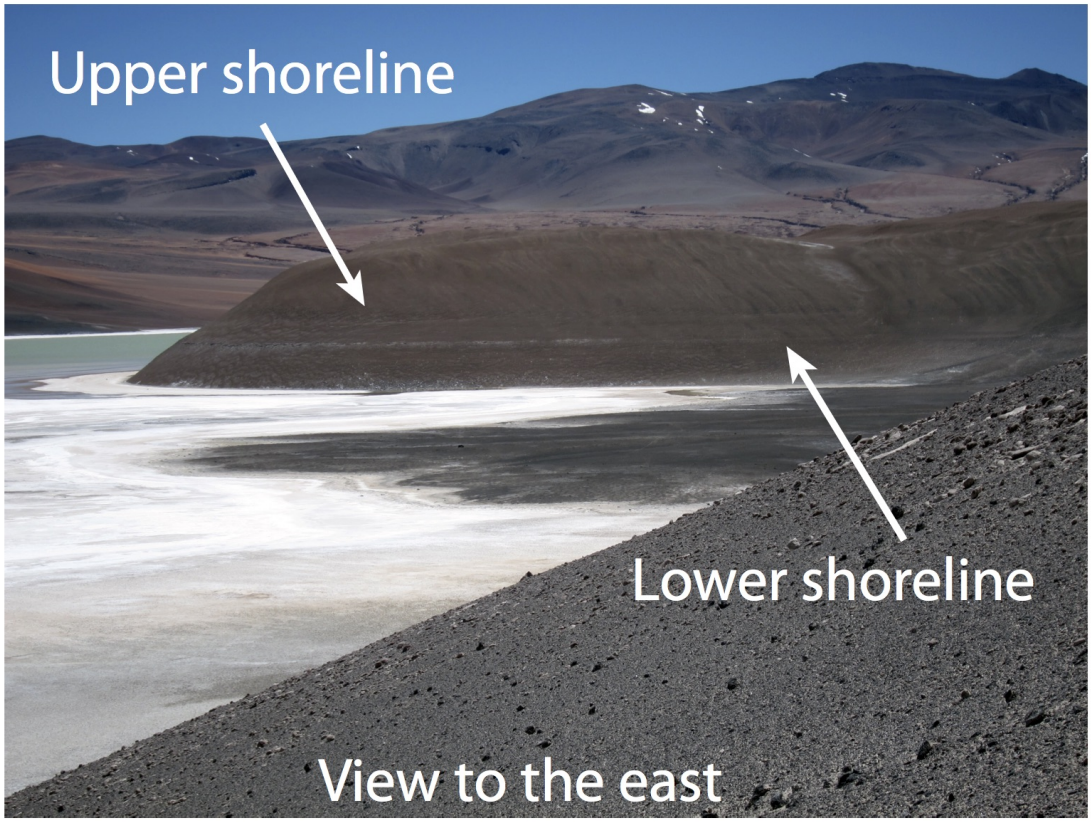

Figure 3.9: Photo from southern shoreline of Laguna de la Azufrera at Lazufre. Two predominant strandlines are visible here along the walls of the salar, and occur frequently along the basin margins.

Lake	Average shoreline slope	ΔLOS velocity gradient (yr-1)
Laguna Celeste	$-3.1x10^{-5}(n=3)$	$-3.4x10^{-7}$
Laguna Mama Khumu	$2.61x10^{-5}(n=3)$	$-3.2x10^{-7}$
Laguna Chojllas	$-5.8x10^{-5}(n=2)$	$-2.8x10^{-7}$
All Uturuncu lakes	$-2.1x10^{-5} \pm 4x10^{-5}(n=7)$	$-3.1x10^{-7} \pm 3x10^{-8}$

Table 3.2: Radial shoreline profile and InSAR ΔLOS velocity gradients for lakes surrounding Uturuncu. Negative slopes imply tilting away from the volcano.

for shorelines at Laguna Celeste, Laguna Mama Khumu, and Laguna Chojllas. We omit shoreline surveys at Laguna Loromayu because it is located along the seam of smaller DEM tiles that were mosaicked together, and thus has a slight elevation discrepancy that makes shoreline correlation more difficult.

Comparing the tilt of measured shoreline profiles to the gradient of the surface uplift along the lakes allows us to approximately constrain the longevity of the modern uplift at Uturuncu. Assuming that uplift began after the formation of all shorelines, we calculate an average tilt for our measured profiles of 10^{-5} away from the summit of Uturuncu (Table 3.2). Our average tilt rate across each lake is 10^{-7} yr^{-1}, so dividing the measured shoreline tilt by the observed tilt rate yields an estimate of 10^2 years for the persistence of the present uplift. We can also place more conservative upper bounds on our timing constraints by estimating the inherent uncertainty in measuring shoreline elevations. Assuming a vertical uncertainty of approximately +/- 0.5 m for a strandline it is possible to estimate, for a given lake, the amount of time it would take for a clear deformation signal to be measurable above this uncertainty. For example, given the modern tilt rate of $-3.2x10^{-7}$ yr^{-1} over the 3.9 km distance of Laguna Mama Khumu, it would take 800 years to achieve a 1 m differential elevation of shorelines on either side of the lake. Therefore, from this order of magnitude analysis of the topography and survey data we estimate the age of the modern uplift episode at Uturuncu to likely be less than 100 years and almost certainly less than 1000 years.

River profiles along Uturuncu

The profiles of alluvial rivers that circumnavigate the periphery of Uturuncu do not correlate with any gradients in surface uplift (Fig. 3.13). The best candidate for measuring changes in surface slope related to deformation is the mainstem of the Río Grande de Lípez (bold lines in Fig. 3.13). Here the uplift gradient linearly decreases from km 13 to km 36 along the mainstem, resulting in a tilt rate of 1.1×10^{-7} yr^{-1}. Integrating the present tilting rates forward from the Tauca highstand would result in a doubling of surface slope along this section; however, the slope of the Río Grande de Lípez remains unchanged through the uplift field. There are also two prominent knickpoints along each of the tributaries, which can often results from either spatial gradients in surface uplift or impulsive changes in uplift rate, but these do not appear to be correlated with an LOS velocity anomaly (Fig. 13). One knickpoint occurs at the junction of the northern and southern tributaries, which commonly results from a change in sediment load between the two rivers (e.g., Finnegan and Pritchard, 2009). The large knickpoint along the southern tributary is located at the northwestern base of Cerro San Antonio where the river appears to be diverting around the volcano (Fig. 3). As Cerro San Antonio is significantly older than Uturuncu (de Silva, 2010, personal communication), this knickpoint is very likely unrelated to the volcanism there.

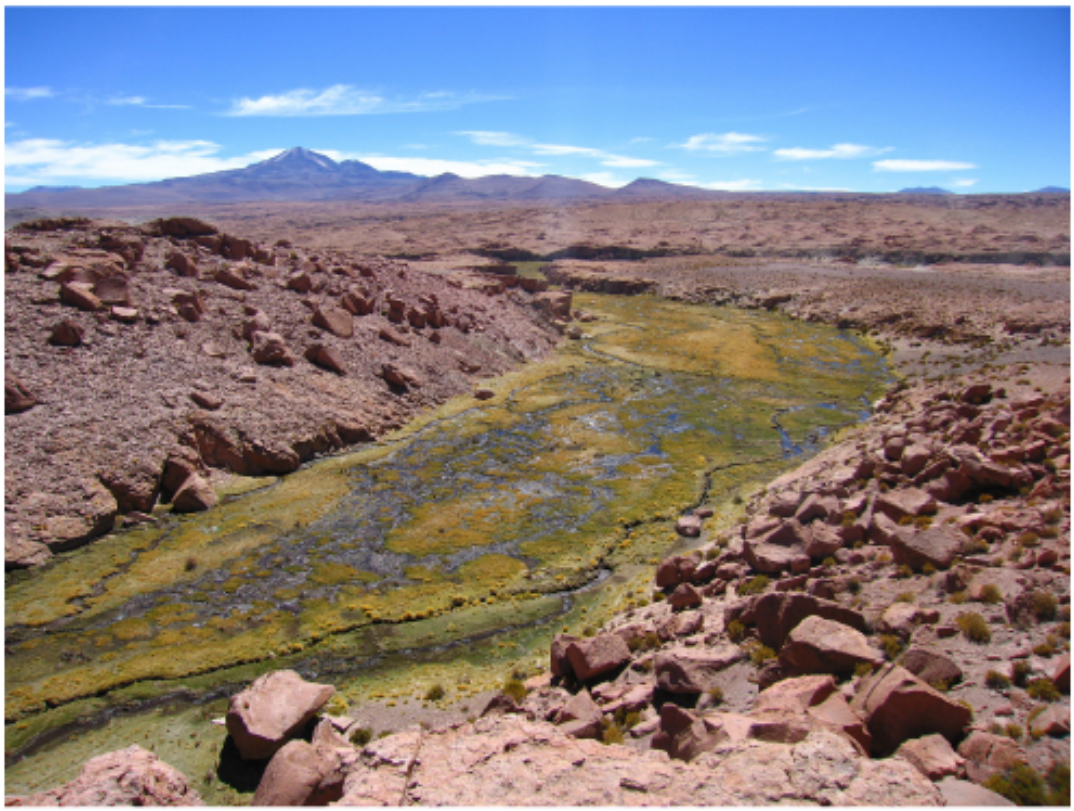

Figure 3.10: Photo from the southwest of Uturuncu showing tributaries of the Río Grande de Lípez. The narrow floodplains of these bedrock rivers now consist of small, anostomosing channels and wetlands.

3.4.2 Lazufre

Constraints on deformation at Lazufre

At Lazufre, Laguna de la Azufrera is at the distal margins of the observed uplift but within the bounds of the long wavelength topographic anomaly (Figs. 3.1 and 3.9). However, like the lakes that surround Uturuncu its shorelines are remarkably flat. Figure 3.8 shows the survey data collected along the shorelines of Laguna de la Azufrera, and a radial projection of their elevations away from the peak LOS velocity anomaly. In this projection the upper shoreline has a negative slope (tilting away from the uplift) of 10^{-4}; however, the lower shoreline that we

surveyed for over a km has a positive slope (tilting down towards the uplift) of 10^{-4}. As the mean slope of the differing shorelines are nearly flat and have an average slope of approximately zero, there does not appear to be any signal of long-term deformation in the shorelines preserved at Laguna de la Azufrera. The horizontal lake shorelines are superimposed on the long wavelength topographic bulge, which has a topographic slope of 3% across the lake (Fig. 3.9). This implies that the majority of surface uplift across the dome was accomplished before the highstands at Laguna de la Azufrera, which are likely Tauca in age.

Uplift constraints from lava flow deflections at Lazufre

Mapped lava flows greater than 5 km in length in the vicinity of Lazufre, in general, tend to radiate outward from the peak long wavelength topographic high. Figure 3.11 shows a map of lava flow directions superimposed on the geophysical and topographic datasets. This type of analysis is inherently noisy as short wavelength topography like individual volcanoes can greatly influence the local direction of lava flows, and indeed some of the longer flows are more controlled by this local effect (Fig.3.11). However, most of the flow orientations are down gradient of the long wavelength topography. This suggests that at the time of eruption for the quaternary volcanoes proximal to Lazufre there was already a topographic high roughly where we find one today. Unfortunately there is not excellent age control for most of these lava flows, but rough constraints exist at Lastarria, Volcán La Moyra at Cordon del Azufre, and Cerro Bayo from K-Ar ages (Naranjo and Cornejo, 1992). The flows at Lastarria range from 0.6 $\pm$ 0.3 Ma to <0.3 Ma, 0.3 $\pm$ 0.3 Ma at Volcán La Moyra, and 1.6 $\pm$ 0.4 Ma at Cerro Bayo (Naranjo and Cornejo, 1992). Because the longest flows at Lastarria and La Moyra appear to reflect the long wavelength topography, it is reasonable to

suggest that the there was a topographic high at Lazufre since at least before 0.3 Ma. A >0.3 Ma magma chamber beneath Lazufre is consistent with structural and volcanological evidence for a long-lived stress orientation similar to that observed today (Ruch and Walter, 2010), as well as magnetotelluric imaging of a partially molten body emanating from the upper mantle into the mid-crust (Budach et al., 2013). Thus, the magma body beneath Lazufre has possibly been causing punctuated surface inflation for hundreds of thousands of years.

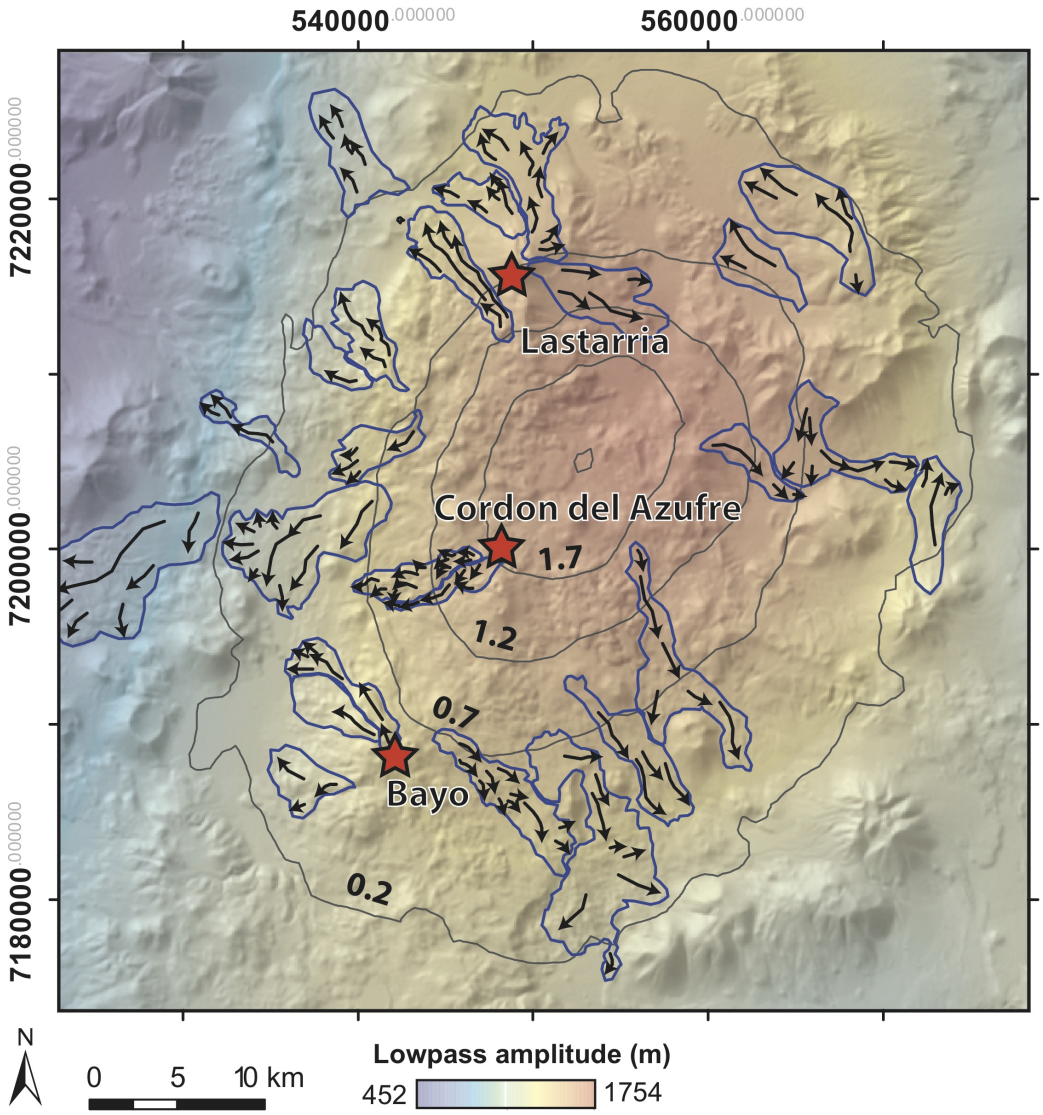

Figure 3.11: Lava flow orientations relative to the long wavelength topography (color gradient) and InSAR line-of-sight velocities (contours at 0.5 cm/yr intervals) at Lazufre. Lava flows $>$ 5 km are denoted by blue outlines, and arrows correspond to local flow direction perpendicular to mapped flow ridges.

3.5 Discussion

The long-term constraints on surface deformation provided by the local geomorphology and volcanology of both Uturuncu and Lazufre may help to discriminate between geophysical models of the plumbing systems beneath each region. Below we address how our data fit with various interpretations of subsurface magma movement.

3.5.1 Diapirism and deflation at Uturuncu

The non-uniqueness of geodetic inversions at Uturuncu makes interpreting the source properties of the surface deformation difficult (e.g., Yun et al., 2006; Henderson and Pritchard, 2013). However, with our long-term topographic constraints we can provide additional context for various model interpretations. Fialko and Pearse (2012) use geodetic observations of a peripheral deflationary moat around Uturuncu to justify a model of a rising diapir from the zone of partial melt beneath the volcano. Though their model matches well with the 18-year time series of surface deformation, they do not consider the effect of a rising diapir over centuries to millennia. In a numerical modeling study, Burov et al. (2003) simulate topographic effects from brittle (plastic), viscous, and elastic deformation by a buoyantly rising magma body over an 1 Myr model run. Model scenarios of early diapiric rise from 10-15 km depths, as is thought to be the case at Uturuncu (e.g., Fialko and Pearse, 2012), show a slowly evolving 200-600 m high topographic dome as the magma body ascends. This topographic effect diminishes over time in their purely viscous scenarios as the diapir impinges on a viscosity contrast in the upper crust and begins to spread laterally, but given that geophysical (del Potro et al., 2013; Comeau et al., 2015) and geodetic (Henderson, G3; Fialko and Pearse, 2012; Hickey et al., 2013) inversions suggest

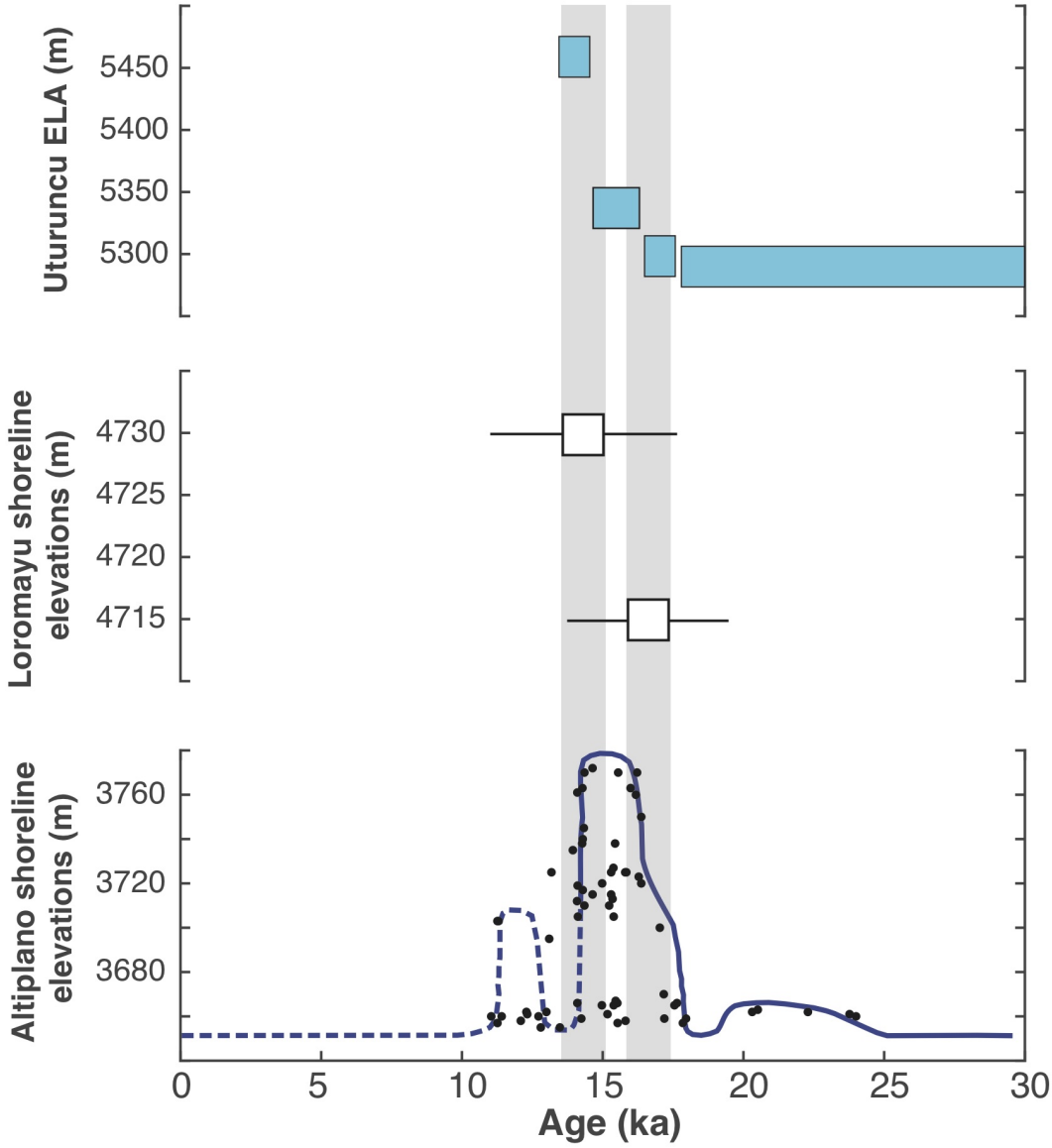

Figure 3.12: Modified figure from Blard et al. (2014) illustrating how the upper OSL shoreline ages at Laguna Loromayu (middle row, our data) fit within the context of both receding equilibrium line altitudes (ELAs) of glaciers at Uturuncu (top row, data from Blard et al., 2014) as well as the Tauca highstand seen in the immense Uyuni and Poopo basins to the north (bottom row, data from Placzek et al., 2006). The consistency of these data suggest a broad climatic signal felt across the central Andes during this time.

a source depth of 15 km, lateral spreading of the diapir at shallow crustal levels is likely not occurring. Furthermore, given the presence of seismicity thought to result from pressurization by the underlying magma chamber (Jay et al., 2011), we can infer that Uturuncu is susceptible to brittle deformation. These modeling results then suggest that topographic doming should accompany a rising diapir at Uturuncu, which we do not see in background topography of (Fig. 2). An alternative model involving deflation of a deep source and inflation of a shallow reservoir at Uturuncu has been proposed by others (e.g., Henderson and Pritchard, 2013). This model can also resolve the observed deflationary moat, and although its viability relies on assuming a much lower viscosity in the lower crust than the mid crust to account for mass balance discrepancies between source and sink (Henderson and Pritchard, 2015), it suggests inflation is periodic and transient rather than continuous over long time intervals. Viscous relaxation time in the crust may be on order of 10^2 years at Uturuncu (Henderson and Pritchard, 2015); therefore if inflation episodes are transient, as geodetic observations suggest, then long-term deformation could relax viscously and hence go unrecorded in the topography. Alternatively, Walter and Motagh (2014) use mapped lineations proximal to Uturuncu to infer a model of long term subsidence from normal faulting triggered by deflation at depth; however, interpreting the origin of lineations at Uturuncu is difficult given the presence of linear geomorphic features such as rivers and wind streaks whose planview orientations are not necessarily dictated by surface fracturing (e.g., Bailey et al., 2007). However, both ideas are consistent with the lack of observed long-term surface uplift at Uturuncu. Taking the observational and theoretical evidence together, it is most likely that Uturuncu experiences pulses of transient inflation/deflation and viscous relaxation over millennial timescales with no net surface uplift, possibly from a lower crustal

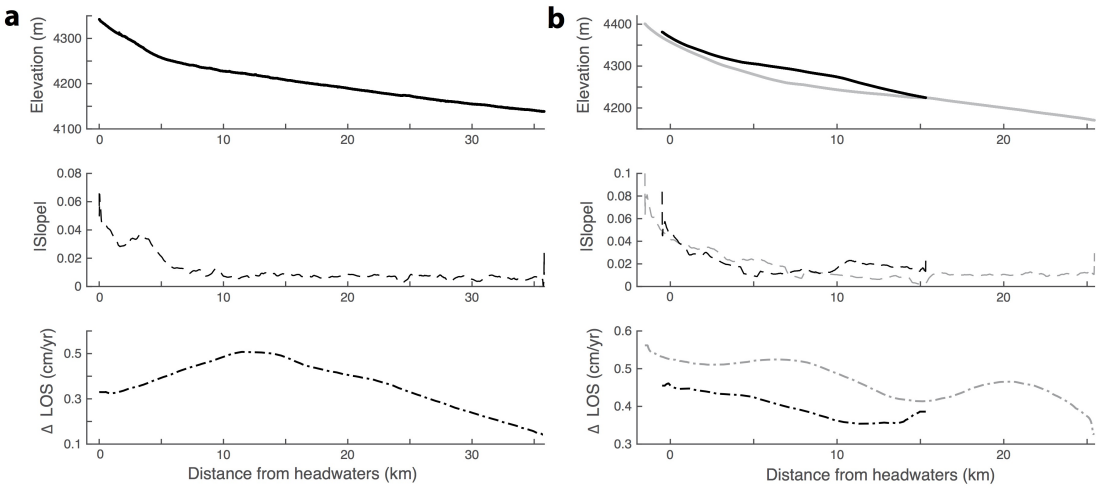

Figure 3.13: Longitudinal profiles, channel slope, and InSAR line-of-sight (LOS) velocities from tributaries of the Río Grande de Lípez proximal to Volcán Uturuncu. Column **a** shows data from the mainstem west of Uturuncu, and column **b** shows data from the two tributaries north of the volcano. The bold lines in **b** refer to the southerly drainage that abuts Cerro San Antonio. Note the 4 mm/yr decrease in LOS velocity from km 12 to km 35 along the mainstem in **a**, and the constant surface slope along this section.

reservoir feeding magma into the APMB. This long-term "heavy breathing" is seen in other active silicic magmatic systems like Yellowstone (e.g., Pierce et al., 2002); however, at Yellowstone there is a complex relationship between magmatic intrusion, migration of hydrothermal fluids, and surface deformation (Wicks et al., 2006). Furthermore, the known deformation patterns associated with pressurization and depressurization by groundwater flow (e.g., Wicks et al., 2006) are not observed in the geodesy of Uturuncu. Alternatively, if we are observing a rising diapir from the upper surface of the APMB, then we must be witnessing the birth of the magma body because there has not been sufficient growth to be observed in either the long wavelength topography or shoreline deflections.

3.5.2 Pre-eruption doming at Lazufre

The long-lived topographic dome, lack of observed short-term peripheral subsidence and shallower source depth make Lazufre's deformation history unique from Uturuncu and more likely associated with a pre-caldera magmatic system (e.g., Ruch et al., 2008). As such, there are a number of questions that arise regarding the nature of long-term deformation here.

Why is the wavelength of the long-lived topographic dome different from the observed short-term deformation?

Figure 3.2 shows that the radius of the topographic dome is wider by 10-15 km than the deformation footprint measured by InSAR. One explanation for this difference in wavelength could be that mechanisms of inflation have changed over the life of this volcanic center. The surface deformation pattern at Lazufre can be fit equally well by intrusion from either a thin sill or a flat-topped magma chamber (Ruch et al., 2008; Lundgren and Pearse, 2013; Remy et al., 2014). This non-unique result is predicted from modeling (Yun et al., 2006), and so evaluating the magma chamber source geometry requires additional constraints. The fact that the topographic dome is >300 ka at Lazufre suggests the presence of a much larger magma chamber beneath the inflation source. Hence, the topography and apparent longevity of the dome at Lazufre may reflect chamber overpressure from accumulation of magma over many such transient sill intrusion events. An additional mechanism for the difference in observed wavelength is the possible time-dependent deformation of a magma chamber with a viscoelastic shell. Given the topographic evidence for a long-lived central magma chamber beneath Lazufre, it is likely that the rocks adjacent to the magma chamber have been thermally weakened beyond the brittle-ductile transition (e.g., Remy et al., 2014). In this

scenario, over short timescales the pattern of surface deformation would reflect the elastic component of deformation from the inner magma chamber. Over time as the stress is transmitted outward toward the edge of the shell, the magnitude of radial displacement increases but at an exponentially decaying rate (Segall, 2010). Dragoni and Magnanensi (1989) estimate the characteristic response time ÏĎ as a function of the shear modulus μ, Poisson's ratio ν, the viscosity η, and the ratio of the shell radius R_2 to the chamber radius R_1. Assuming a Poisson's ratio of $\nu = 0.25$, the relationship simplifies to $\tau = 1.8(\tau/\mu)(R_2/R_1)^3$. For a viscosity of 10^{18} Pa s, a shear modulus of 20 GPa (e.g., Ward et al., 2014), and various combinations of shell thickness to chamber radius the relaxation timescale can range from 5-25 years. As the present deformation phase began at approximately 2002 (Henderson and Pritchard, 2013), we may have yet to see a change in the wavelength of deformation due to viscoelastic effects. However, given that the viscosity of the shell is likely smaller than 10^{18} Pa s, it seems more likely that the effect of a viscoelastic shell is a secondary effect.

How does Lazufre's spatiotemporal deformation fit in with our understanding of caldera magmatism?

Recent thermo-mechanical models of caldera-scale magma chamber pressurization show uplift signals of 1 km as systems progress toward eruption (Gregg et al., 2012). Existence of the dome during the formation of peripheral volcanoes along Lazufre at from 500-300 ka provides further evidence that they could be related to zones of high tensile stress at the margins of a large silicic chamber (e.g. Froger et al., 2007), and thus it seems increasingly likely that the peripheral volcanoes at Lazufre are genetically related to a single pre-caldera magmatic system (e.g., Lipman, 1984; Froger et al., 2007; Karlstrom et al., 2015).

As Froger et al. (2007) state, examining the bulk geochemistry of the peripheral volcanism may help test this hypothesis. If Lazufre's dome began inflating at 500 ka, then it would have a long-term average uplift rate of 1 mm/yr, which likely represents periods of quiescence separated by episodes of rapid inflation like we see today. If sill intrusions tend to cause surface uplift at 2.5 cm/yr, that implies that Lazufre has been quiescent over 96% of its lifetime. Presently 0.4 % of the 900 volcanoes that comprise the Central Andes are actively deforming, (Hualca Hualca, Peru; Uturuncu, Bolivia; Lazufre, Chile/Argentina; Cerro Blanco, Argentina). Depending on the longevity of active uplift pulses, which an extended time series of InSAR measurements will help uncover in the future, this could provide an explanation why we only see active uplift at a small percentage of volcanic systems in the Central Andes. If Lazufre is indeed a pre-caldera system, then an interesting question arises as to whether we can use measurements of the system geometry to learn anything about its potential eruption style. A critical metric for determining the mode of failure in models of caldera eruption is the caldera roof aspect ratio R, which is the ratio of magma chamber width to depth below the surface (Gregg et al., 2012). With a modeled source geometry of 35 km width at 10 km depth for the inflating sill or chamber roof (Ruch et al., 2008), the magmatic system at Lazufre has a roof aspect ratio of R 0.28, which puts it near the threshold of critical failure via roof collapse for modest overpressures (20 MPa) if the chamber is sufficiently large (10^3 km^3) (Gregg et al., 2012). However, an estimate of the entire magma chamber volume beneath Lazufre remains elusive. If the modeled deformation source corresponds to the top of a thicker chamber rather than a thin sill, a chamber height of 1-2 km would yield a volume of 700-1400 km^3 for a 30 km diameter magma body, indicating that overpressures not significantly greater than the 10 MPa presently

observed at Lazufre (Ruch et al., 2008) could potentially lead to eventual failure of the overlying roof. Geophysical imaging of the magmatic plumbing system at Lazufre may help determine what the true geometry of the magma chamber is, and hence what mechanical conditions are necessary for a future eruption at the caldera scale.

3.6 Conclusions

Our observations using geomorphic markers to infer the paleo-geodetic history of Uturuncu and Lazufre reveal similar characteristics yet distinct deformation histories for each region. Uturuncu shows no evidence for net inflation since 16 ka from our lake shoreline and river profile measurements, and has no signal of long-wavelength uplift that is predicted for a buoyantly rising diapir. This is likely because either: 1) the inflation is due to transient upward migration of melt from a deep source to a shallow sink, and either dissipates or deflates over time; or 2) we are witnessing the first century of its development. At Lazufre, we find that the observed 500 m amplitude long wavelength dome has likely existed as a local topographic high since at least 300 ka. Though the rate of change of surface elevation may be too slow to measure using 10^4 year timescale measurements like paleo-shorelines, the longevity of deformation suggests the presence of a large magma chamber below the active sill-like intrusion at 10 km depth. Knowledge of surface displacements over the long timescales associated with magma intrusion can therefore be a useful tool in understanding the processes that shape large silicic magmatic systems.

3.7 Acknowledgements

We would like to thank Shan de Silva and Kerri Johnson for field assistance and many conversations about volcanoes and geomorphology. We would also like to thank our drivers and Linda Hauge Kossatikoff from Lipiko Tours for their logistical support. This work was supported by National Science Foundation Grant EAR 0908850 to N.J.F.

Chapter 4

Amplification of bedrock canyon incision by wind

4.1 Abstract

Bedrock canyons are ubiquitous on Earth and Mars, and river canyon morphology is commonly used to interpret the climatic and tectonic histories of landscapes (Ferrier et al., 2013; Howard et al., 1994; Schoenbohm et al., 2004). On both planets, however, many bedrock canyons exist in dry, wind-dominated environments (Goudie, 2008; Baker, 2001; Howard et al., 2005). Although wind abrasion can significantly influence the evolution of arid landscapes (e.g., Goudie, 2008; McCauley, 1973), the role of wind in shaping arid bedrock canyon systems is poorly understood and thus typically neglected. Here we exploit a natural experiment on the western slope of the central Andes that allows direct comparison of 36 wind-affected and wind-protected canyons, and show through a combined analysis of canyon morphology and topographic wind modeling that wind abrasion can amplify bedrock canyon incision rates by an order of magnitude above fluvial

rates. Our results imply that wind can propagate bedrock canyons, landforms traditionally thought only to evolve from flowing water. Furthermore, our analyses reveal a direct relationship between aerodynamics and landscape evolution at varying scales. Topographic shielding of high winds by mountains modulates the pace of canyon retreat, while individual canyon profiles become aerodynamically streamlined. We conclude that wind abrasion can exert a dominant control on landscape evolution even in landscapes where large river gorges are present.

4.2 Introduction

On Mars, bedrock canyons are one of the most commonly measured features employed for understanding hydrologic conditions throughout the planet's history (Baker, 2001; Howard et al., 2005; Pieri, 1980; Carr and Clow, 1981; Aharonson et al., 2002). Although most Martian canyons are thought to originate from either prolonged surface runoff (Howard et al., 2005; Aharonson et al., 2002), groundwater sapping (Pieri, 1980; Aharonson et al., 2002), or megafloods (Baker, 2001; Lamb et al., 2008), persistent surface water on Mars vanished at the end of the Hesperian period (Carr and Head, 2010), leaving its surface exposed primarily to atmospheric winds for the past 3 Ga. As modern-day wind abrasion rates on Mars are comparable to those on Earth (Bridges et al., 2012), there is potential for substantial modification of Martian valley networks by wind (e.g., Fig. 4.1).

In Kasei Valles, for example, flood discharges estimated using canyon geometry are two orders of magnitude larger than any megaflood event measured on Earth (Baker, 2001). Given that *1)* evidence for wind abrasion along the canyon floors of Kasei Valles suggests a deepening of the channel (e.g., Fig. 4.1c), and *2)* that the encompassing region has been shown through global climate modeling to exist in a net wind erosional environment for the past 1 Gyr (Armstrong and Leovy, 2005),

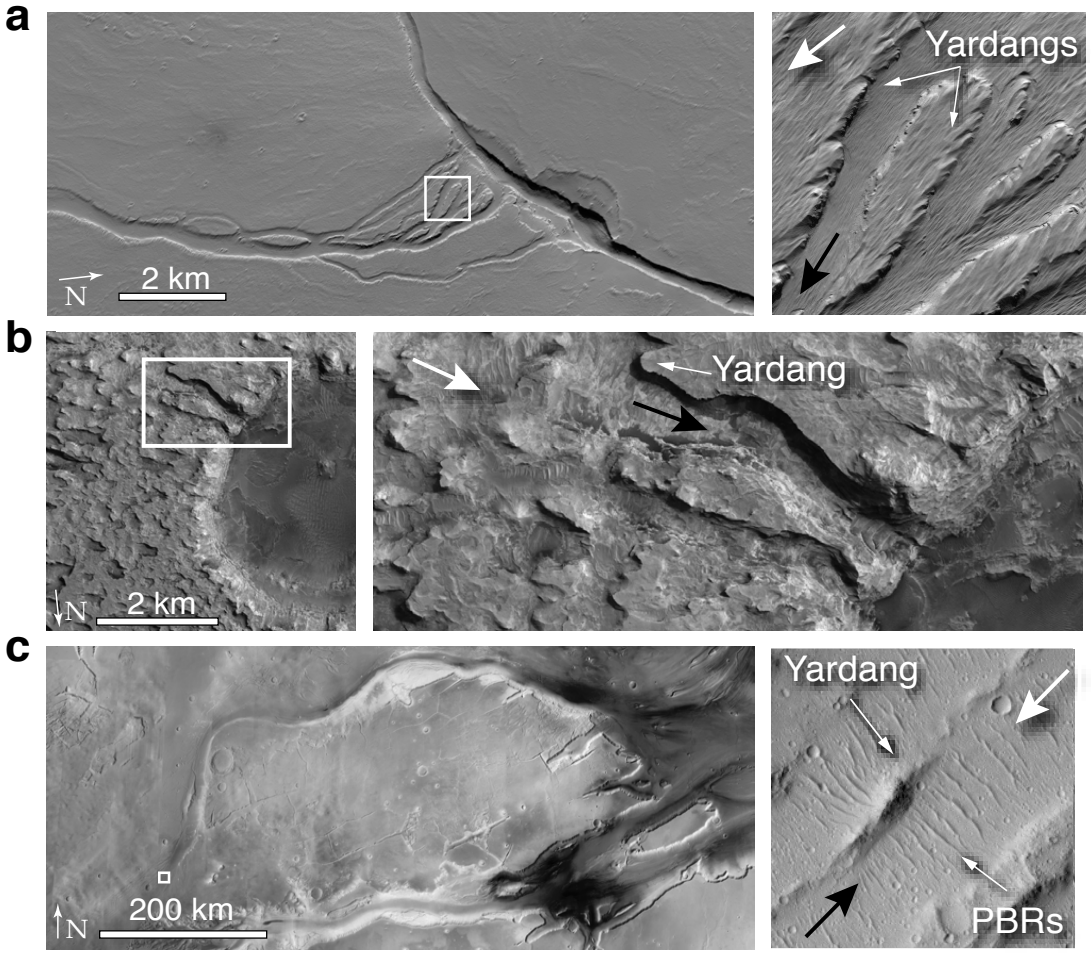

Figure 4.1: Satellite images showing evidence for wind abrasion along Martian bedrock canyons. White arrows indicate wind direction; black arrows indicate the direction of water flow. **a.** HiRISE image (PSP 002486 1860) of a distributary channel network near Ascraeus Mons. Islands between the branching channels are evolving into megayardangs. **b.** HiRISE image (ESP 013097 1850) shows a canyon entering Crommelin Crater whose headwaters are evolving into a yardang field. **c.** Image of Kasei Valles (ESA ID 292688). Inset image (HiRISE PSP 010462 2035) shows a field of yardangs and periodic bedrock ridges (e.g., Montgomery et al., 2012) along the broad channel floor oriented opposite the direction of water flow.

it is reasonable to suspect wind may have played a role in modifying the channel morphology here. Though wind abrasion may ultimately be less important to shaping Kasei Valles than flood incision, these observations nevertheless provide motivation for exploring the role of aeolian processes in shaping bedrock canyons in arid landscapes.

The 4.09 Ma Puripicar ignimbrite (Salisbury et al., 2011), located on the western slope of the Andes in northeast Chile (Fig. 4.2a), provides a natural experiment that isolates the effect of wind abrasion on bedrock canyon morphology. Bounded at its western edge by a 70 km, N-S trending escarpment that ranges in height from 15-150 m, the Puripicar exhibits a series of 46 bedrock river gorges that bite into the escarpment along its entire length. Deflection of the zonal westerlies over the Andes (Vuille, 1999) results in a regional scale unidirectional wind pattern (Vuille, 1999; Kreuels et al., 1975), and NW-SE trending wind abrasional features across an array of ignimbrite surfaces spanning 1-5 Ma from 21°S-24°S suggest this pattern has been relatively consistent over a very large area since the Pliocene (Bailey et al., 2007).

The southern half of the Puripicar frontal escarpment abuts a prominent ridge of Paleozoic basement rock that serves to shield the escarpment face from the predominantly northwesterly winds and results in a first-order difference in canyon form (Fig. 4.2b, c). This natural control allows us to quantify rates of canyon retreat into the frontal escarpment for both the wind-affected and wind-protected populations. Below we discuss the unique conditions of this natural experiment, describe in detail the morphologic evidence for wind-driven canyon retreat, and show conceptually using both a static topographic wind model and a forward abrasion model how aerodynamically forced wind abrasion can propagate canyons and streamline them in the process.

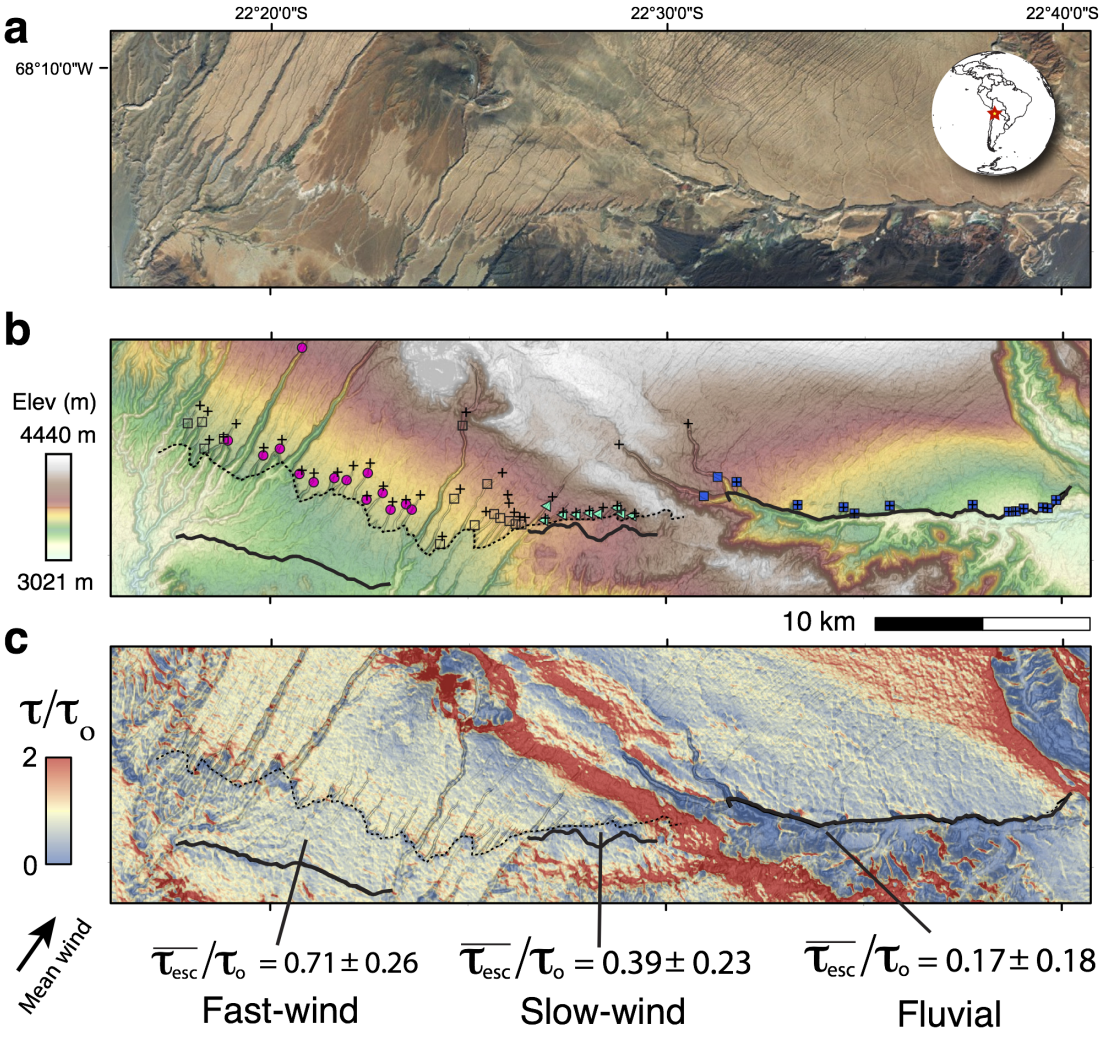

Figure 4.2: Overview of the Puripicar frontal escarpment. **a.** Satellite image showing canyon morphology **b.** Shaded elevation map derived from ASTER digital elevation model. Magenta circles are canyons in the fast-wind regime; cyan triangles are canyons in the slow-wind regime; blue squares are wind-protected canyons in the fluvial regime. Plus symbols (+) are locations of canyon heads. Empty squares are canyons omitted from the analysis. **c.** Results of a topographic wind model run showing normalized surface shear stress with incident winds from the northwest. Labeled values correspond to mean normalized shear stress ($\pm 1\sigma$) along each escarpment location ($\overline{\tau_{esc}/\tau_o}$).

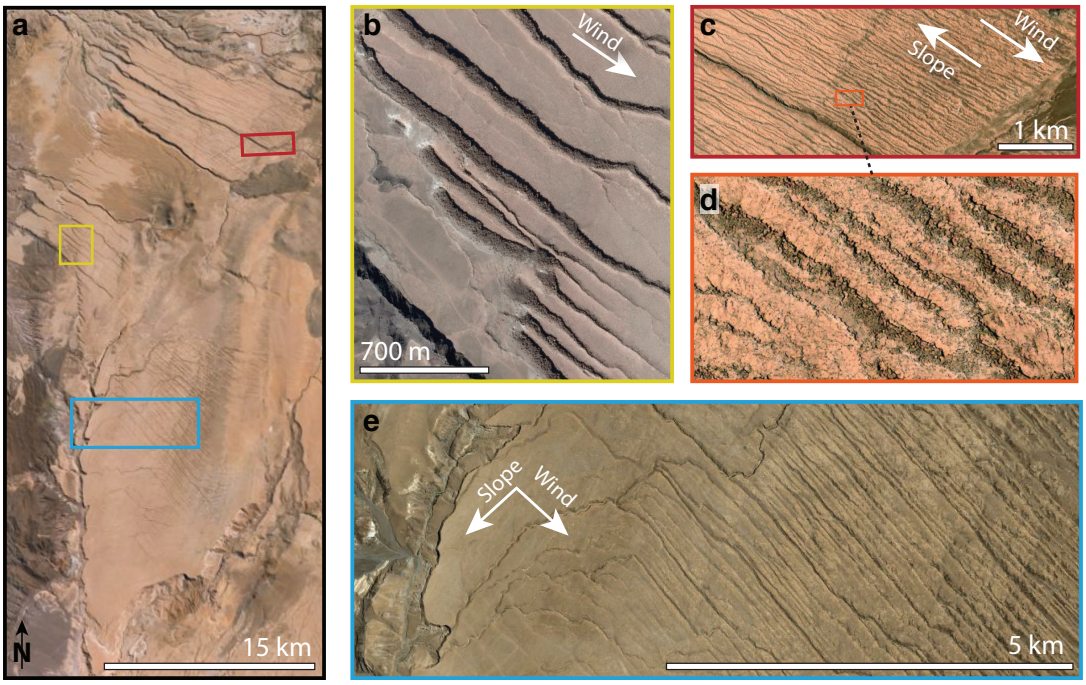

Figure 4.3: **a.** Overview image of the Puripicar ignimbrite. **b.** Inset from **a** showing the destruction of fluvial networks by wind-driven escarpment retreat. **c.** Inset image showing a complex channel network morphology that results from the combined effects of wind and water erosion (Bailey et al., 2007). What look like river channels at the NW edge of the image become increasingly more closely spaced, linear, and extend off the back edge of the ignimbrite (SE corner of the image). **d.** Inset from **b** showing interfluves which disaggregate into megayardangs. **e.** Inset showing a different morphology that results when the prevailing northwesterly winds blow obliquely to the slope direction of the ignimbrite surface (Bailey et al., 2007). Here the river channels flow down to the southwest, and the erosional fabric of extremely linear and parallel channels formed by wind abrasion is oriented to the southeast, producing a channel network whose tributaries dogleg to the southwest as they approach the frontal escarpment. Images ©Esri, ArcGIS 10.

The Puripicar is a 1400 km^3, crystal-rich, dacitic ignimbrite erupted during a phase of intense silicic volcanism within the Central Volcanic Zone of the Andes in the mid Pliocene (de Silva, 1989b). Erupted from the western edge of the Altiplano at 4500 m, the pyroclastic flows descended downslope along the western Andean front to an elevation of 3500 m (de Silva, 1989b). Vapor phase alteration from post-emplacement gas escape resulted in a resistant caprock of several meters thickness along the Puripicar's upper surface that overlies the much weaker, lower tuff unit (de Silva, 1989b). Westerly wind erosion scars the headwaters of the Puripicar along the caprock surface, carving tributaries into a complex suite of wind-parallel streaks and yardangs (Bailey et al., 2007) (Fig. 4.3).

The frontal escarpment of the ignimbrite appears to have initiated from incision into transverse valleys created where the ignimbrite pooled behind local topographic highs (Fig. 4.2b). The escarpment-perpendicular canyons we observe within the Puripicar are thus likely incising as a transient response to the change in local base level produced by creation of the frontal escarpment shortly after its emplacement. In bedrock river systems, these incisional pulses tend to migrate upstream as kinematic waves referred to as knickpoints (e.g., Seidl and Dietrich, 1992). As channels re-adjust to a new equilibrium, knickpoints migrate upstream, and canyons propagate farther into the deposit.

We observe, however, a first-order difference in canyon morphology between the northern and southern segments of the Puripicar ignimbrite, suggesting a fundamental change in erosional process that corresponds to the transition from wind-affected to wind-protected canyons (Fig. 4.2b,c). Canyons along the northern escarpment of the deposit are both more elongate and more v-shaped in plan view than canyons to the south (Fig. 4.4a,b). The interfluves along the northern section have been characterized as megayardangs that retreat via wind

erosion of the lower, weaker tuff and subsequent block collapse of the resistant caprock (de Silva et al., 2010). Additionally, geologic and geomorphic evidence suggest portions of the northern escarpment originated more than 3 km to the west at the feet of small transverse ridges (bold lines in Fig. 4.2, Fig. 4.5).

Conversely, canyons along the southern 20 km of the Puripicar are stubby in plan view, theater-shaped, and nested behind an escarpment that has not retreated far beyond its initial edge (Figs. 4.2b, 4.4a). The theater-headed shape and steep headwalls of the southern canyons are consistent with knickpoint retreat from vertical drilling of the weak lower rock and undercutting of the caprock by plunge pool erosion (Lamb et al., 2007). Though the caprock appears to thicken gradually to the south, this gradual change does not correlate spatially with the abrupt change in canyon form and is thus not likely a primary control. Here the escarpment is located behind a 500-700 m ridge of Paleozoic basement rock (de Silva, 1989), which acts as a barrier to shield the lower canyon mouths from regional northwesterly winds (Fig. 4.2c).

Given that lithology and climate do not vary systematically between our two primary populations, we hypothesize that wind abrasion of the exposed knickpoint faces accounts for the morphologic difference in canyons along the escarpment. Figure 4.6 illustrates how differences in erosion process between wind and water along the Puripicar yield different predictions of local erosion rate and consequently canyon morphology.

4.3 Methods

Here we describe our methods and justifications of our topographic analysis, as well as our numerical modeling schemes.

4.3.1 Mapping the initial position of the Puripicar escarpment

We map the initial position of the escarpment using the following lines of evidence. *1)* Across the entire deposit, the ignimbrite appears to have terminated by pooling behind local topographic highs (Fig. 4.2b). A natural consequence of this pooling is the creation of valleys parallel to the margin of the deposit along the base of the topographic ridge. Surface water gets channeled along this margin, providing a mechanism to generate relief and form an escarpment. *2)* The ignimbrite surface behind the wind-affected escarpment projects directly to the escarpment-parallel valley axis approximately 3 km upwind. Figure 4.5 shows the downslope projection of a 1D best-fit quadratic polynomial through the upper ignimbrite surface ($R^2 = 0.99$). We map two locations where the Puripicar appears to have initially pooled at the base of a local ridge (Fig. 4.2b).

4.3.2 Analysis of canyon incision using topographic and imagery data

We identify 46 bedrock canyons along the Purpicar modern frontal escarpment using both Worldview satellite imagery and ASTER elevation data, and restrict our analysis to 36 canyons that correlate to our mapped initial escarpment locations. To quantify canyon incision rates for each channel we measure the horizontal along-channel distance that each knickpoint has migrated behind its mapped initial escarpment ($\Delta x = x_{final} - x_{initial}$) and divide by the age of the deposit (4.09 Ma, from Salisbury et al., 2011), assuming that creation of the escarpment occurred shortly after emplacement of the ignimbrite. We map channel pathways using a flow-routing algorithm within ArcGIS, and identify

knickpoint crests as the large downstream break in slope along each channel's longitudinal profile (e.g., Fig. 4.4b). We calculate upstream drainage area at each knickpoint crest using a flow-accumulation tool within ArcGIS. Figure 4.7 shows the distribution of drainage areas for both the windward and wind-shielded canyons. The range of drainage areas between wind-affected and wind-protected populations overlaps nearly completely, indicating that drainage area differences are likely not responsible for the discrepancy in knickpoint retreat rates between the two populations. We divide our canyons into three populations: *fluvial*, *slow-wind*, and *fast-wind*, that correspond to broad zones along the Puripicar's frontal escarpment whose mean normalized shear stress values in front of the escarpment ($\overline{\tau_{esc}/\tau_o}$) differ significantly as a result of shielding by large topographic obstacles. We calculate knickpoint slopes by measuring the approximate vertical and horizontal step dimensions along each channel. We first mark the upper and lower bounds of the step by hand, which we identify as marked deviations in channel slope from the upstream and downstream channel segments (e.g., Fig. 4.4b). We then measure the absolute vertical (H) and horizontal (L) distances between the upper and lower bounds of the step, and take the knickpoint slope as the ratio H/L.

Using Worldview-1 satellite imagery within ArcGIS, we identify canyon heads as locations where channel walls begin to substantially widen toward the escarpment (e.g., Figures 4.4a,b). Wind-protected canyon heads are co-located with topographic knickpoint crests (Fig. 4.4a). Wind-affected canyon heads are located downwind of topographic knickpoint crests and correspond to the upper-most fracture plane in the caprock where blocks are being delivered to the channel (Fig. 4.8, 4.9). We estimate variations in canyon width between our windward and wind-protected canyons by measuring across-canyon horizontal

distance along the modern escarpment.

4.3.3 Topographic wind modeling using digital elevation models and idealized ramps

We use a mass-conserving topographic wind model (WindNinja) together with a 30 m ASTER digital elevation model to constrain the influence of large topographic structures on the regional wind field across the Puripicar ignimbrite's frontal escarpment. Because we are interested primarily in the relative change of surface shear stress induced by topography, we normalize all shear stress measurements to the upstream flow condition in our model, and use generic values of incident shear velocity and surface roughness (1.0 m/s and 0.01 m, respectively). We assign an incident wind direction of 305^o, parallel to wind abrasion features along the Puripicar surface and consistent with measurements of paleo-wind direction across the central Andes since the Pliocene (Bailey et al., 2009).

We model wind speed variations over knickpoint topography by generating 2D sigmoidal ramps of the form $1/(1 + ce^{-x})$ with step dimensions equal to our fluvial, slow-wind, and fast-wind populations (e.g., Figs. 4.11 and 4.13). We estimate local surface shear stress by measuring the vertical gradient in velocity (e.g., Deaves, 1975):

$$\frac{\tau}{\tau_o} \approx \lim_{z \to 0}(1 + \Delta s)^2 \tag{4.1}$$

where

$$\Delta s = \frac{u(x, z)}{u(x_o z - hf(x))} - 1 \tag{4.2}$$

is the fractional speed-up ratio directly above the bed and hf(x) is the

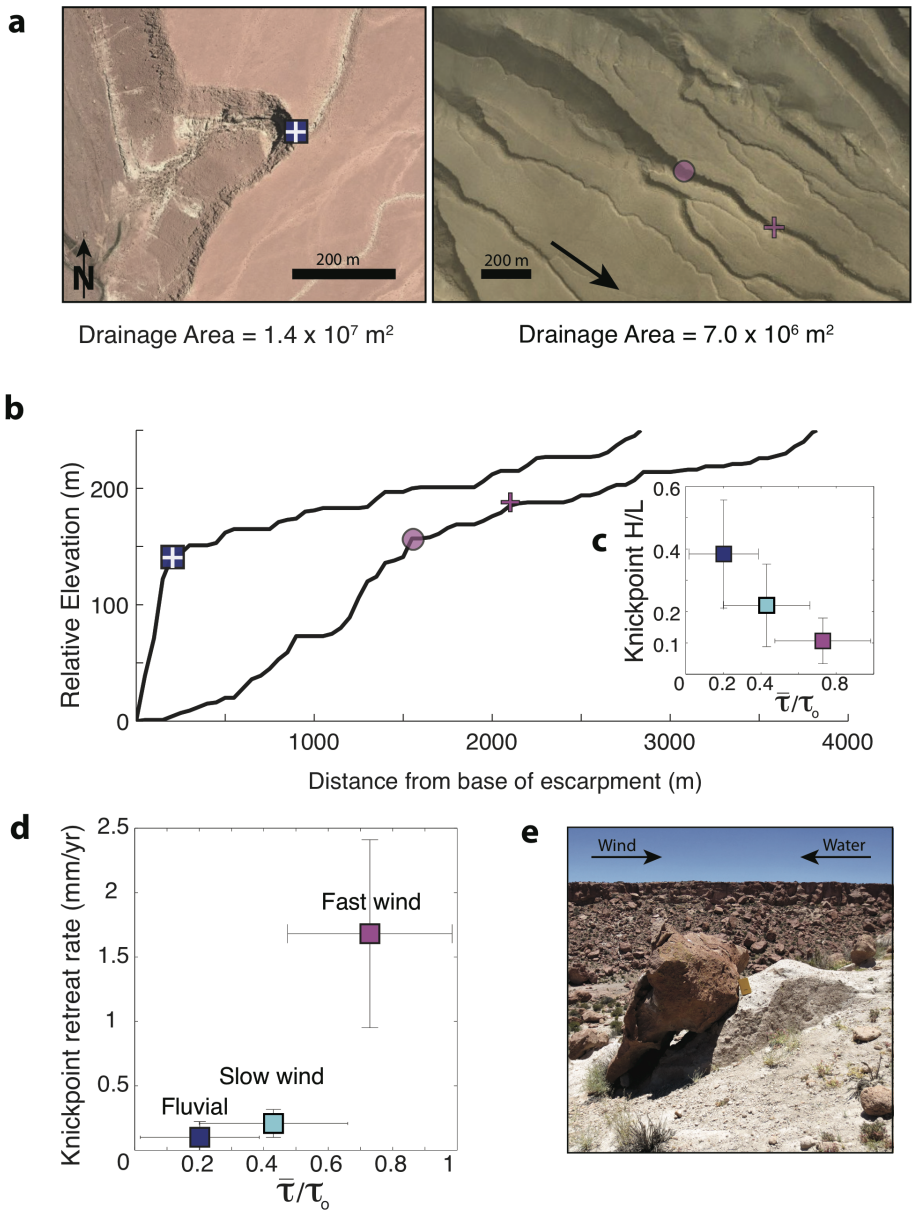

Figure 4.4: Comparison between wind-protected and wind-affected channels. **a.** Satellite images showing representative shapes of wind-protected and wind-affected canyons of comparable drainage areas. Plus symbols represent canyon heads; shapes correspond to knickpoint crests **b.** Profiles of channels in **a.** **c.** Mean ($\pm 1\sigma$) knickpoint slopes as a function of mean ($\pm 1\sigma$) normalized shear stress at the escarpment ($\overline{\tau_{esc}/\tau_o}$). **d.** Mean ($\pm 1\sigma$) canyon retreat rate as a function of mean ($\pm 1\sigma$) normalized escarpment shear stress ($\overline{\tau_{esc}/\tau_o}$). **e.** Photo looking across a wind-abraded canyon where a fallen boulder casts an erosional shadow within the weak underlying tuff.

elevation of the bed topography. We measure velocity speed-up (Δs) at $z = 10$ cm, and normalize the measurements to our upstream flow condition along a flat surface (τ_o). ASTER topographic data is publically available and can be found at (gdem.ersdac.jspacesystems.or.jp/). Data from our topographic analysis is available as a spreadsheet within our Supplementary Information (Supplementary Table 1). WindNinja is freely available at (http://www.firelab.org/project/windninja).

4.3.4 Forward modeling profile retreat from wind abrasion

As our static wind model suggests, we hypothesize that the topographic forcing of wind over a knickpoint leads to enhanced abrasion at its crest and consequently a more aerodynamic canyon geometry. It is well known that winds speed up at topographic highs due to slight compression of the boundary layer (e.g., Jackson and Hunt, 1975), and that wind abrasion rate is very sensitive to changes in the boundary shear stress (e.g., Anderson et al., 1986), therefore topography should exert an influence on local wind abrasion rates. To test this idea we develop a numerical model coupling an empirical model for windflow over an escarpment (e.g., ASCE, 2010) to a wind abrasion model (e.g., Greeley et al., 1982; Anderson et al., 1986; Bridges et al., 2012), expressed by:

$$\dot{A} = \frac{S_a Q_v}{z}(\alpha \cos\theta + \sin\theta), \tag{4.3}$$

where Sa is defined as the abrasion susceptibility, defined as mass removed per mass of incoming particles; z is the saltation hop height, α is the ratio of hop height to hop distance, and θ is the slope of the ground beneath the particles. Q_v is the volumetric saltation flux (Bridges et al., 2012), which is equivalent to the saltation mass flux Q_m divided by the density of the sediment (ρ_s). We use an

expression for steady-state saltation mass flux derived by Kok et al., 2013:

$$Q_m = C\frac{\rho_a}{g}u_{*it}(u_*^2 - u_{*it}^2), \tag{4.4}$$

where C is an empirically derived constant equal to 5 for 250 micron sand, u_* is the local shear velocity, and u_{*it} is the impact threshold for saltation, which is found empirically to be 0.2 m/s (Bagnold, 1941).

Greeley et al., 1982 perform experiments to constrain the parameter Sa for a variety of rock types find that: 1) Sa is directly proportional to grain kinetic energy; and 2) that Sa for lithified tuffs is a factor of 10 greater than unlithified tuffs. Here we set up our domain to account for the rock type variability (Fig. 4.13), but we let the knickpoint face evolve at a rate dependent on the abrasion of the underlying weaker rock since it will undermine the more indurated caprock and ultimately govern surface evolution. Additionally, since we are viewing this model as a heuristic exercise in examining the relative controls of different parameters on the evolution of the channel profile rather than focusing on the absolute values of rates, we cast S_a as being directly proportional to the square of the particle velocity, V_p and the cube of the grain diameter, D_p. In experiments of saltation particle trajectories (Greeley et al., 1982), it is found that on Earth particle velocities travel at about 90% of the free-stream velocity. We can then find the free-stream velocity by assuming a logarithmic velocity profile that generally describes flow within a turbulent boundary layer, given by:

$$U(z) = \frac{u_*}{K}ln(\frac{z}{z_o}), \tag{4.5}$$

where K is equal to von Karman's constant (0.4), z is height above the bed, and z_o is the aerodynamic roughness height, which we approximate as $D_p/30$ (Greeley and Iverson, 1984) since it is usually observed that the saltation cloud tends to

break up the viscous sub-layer during transport events (Kok et al., 2013).

Equation 4.4 assumes a transport-limited saltation mass flux of sand during wind transport events, which will inevitably lead to over-prediction of abrasion rates for our supply-limited landscape. Again, here our primary goal is to study the morphologic change of the canyons brought about by wind abrasion, so constraining model rates is beyond the scope of this study.

At each time step, we utilize the geometry of the channel profile to inform an empirical model for wind shear over an escarpment (ASCE, 2010), which depends primarily on the vertical length scale of the step H relative to the horizontal length scale L. We objectively measure these length scales at each time step using a least-squares approach for detecting hinges in a linear profile. Starting from the center of the knickpoint at the previous time step, we find the upper and lower bounds of the knickpoint from the most statistically significant break in the linearity of the profile both upstream and downstream. We can then calculate both the step height and width (Fig. 4.13).

We approximate a representative shielded canyon profile as a sigmoidal ramp for our initial condition, and we use a logarithmic velocity profile at the domain boundary. Figure 4.14 shows the effect of knickpoint topography on the modeled velocity field, with speed-up concentrated toward the crest. As the knickpoint propagates downwind over time, preferential abrasion at the crest causes the knickpoint slope to relax (Fig. 4.14). This relaxation extends the horizontal lengthscale of the knickpoint relative to the elevation lengthscale, which in turn decreases the speed-up effect. The knickpoint continues to relax as it propagates downwind, resulting in an aerodynamically sculpted river canyon much like a yardang.

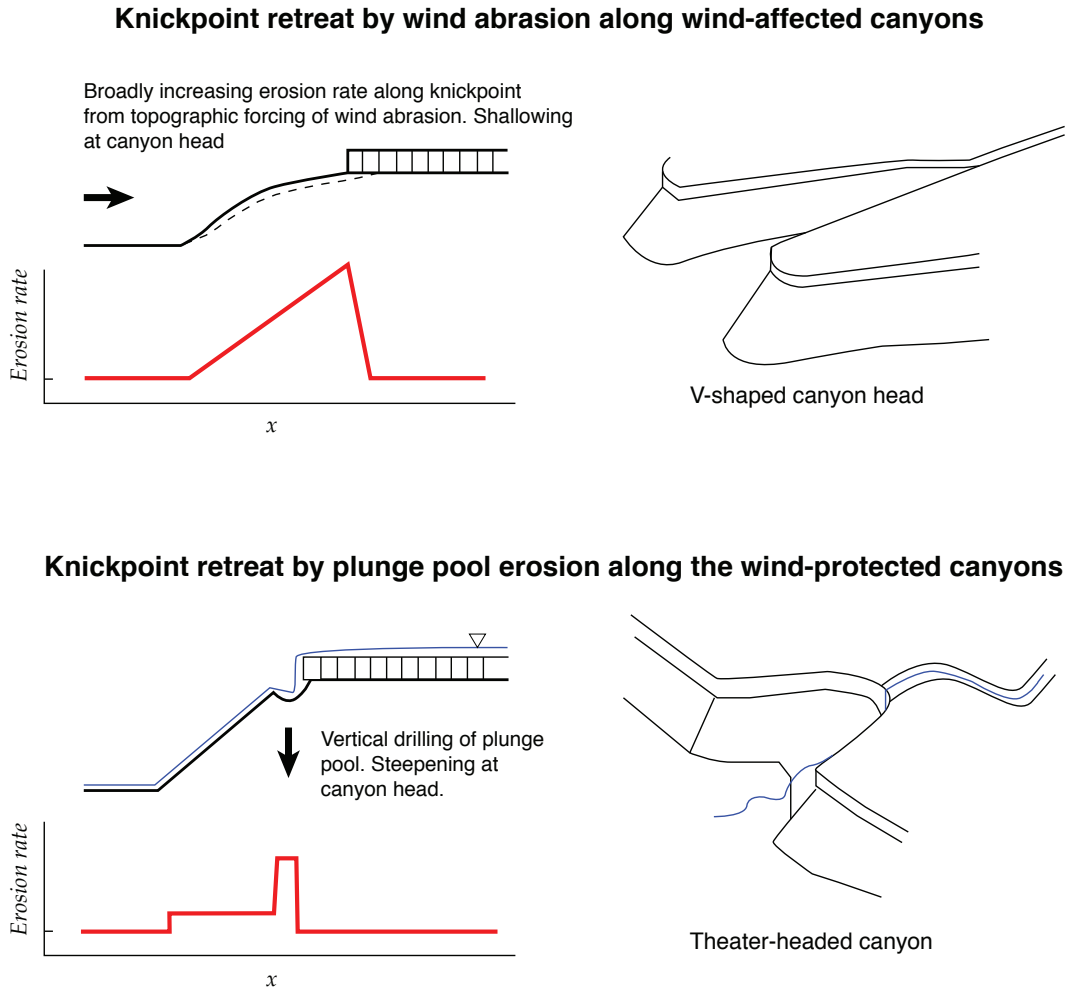

Figure 4.5: Cartoon illustrating the different predicted effects of wind and water erosion on canyon morphology. **a.** Characteristic profile geometry of a wind-affected canyon, with caprock boundary downwind of the topographic knickpoint crest, and hypothesized erosion pattern from topographic forcing of wind over the knickpoint. Erosion rate increases along the knickpoint, causing retreat by undermining the caprock and leading to a v-shaped canyon head. Once above the resistant caprock, erosion rate drops abruptly. **b.** Characteristic profile geometry of a wind-protected, fluvially dominated channel. Erosion is focused along the plunge pool where vertical drilling of water into the weak lower substrate can increase channel relief and undermine the caprock causing knickpoint retreat. The increase in relief by plunge pool erosion at the substrate boundary consequently leads to a more theater-shaped canyon head.

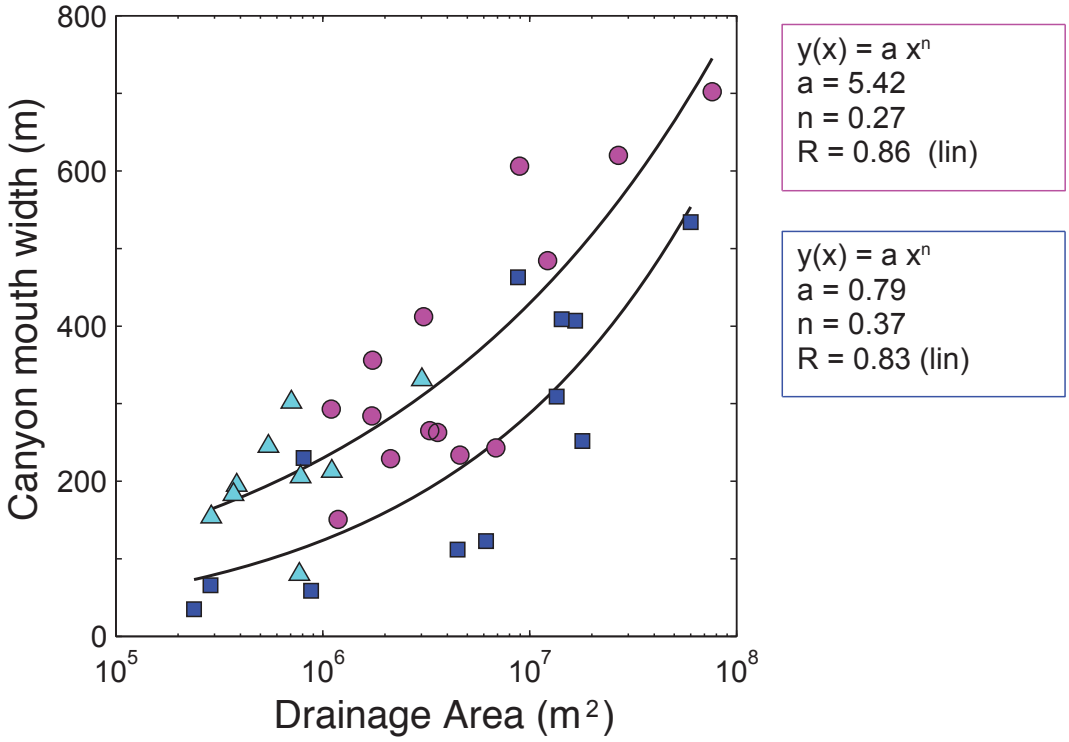

Figure 4.6: Plot of canyon mouth width as a function of upstream drainage area. Wind-protected canyons are blue squares, and show a power-law scaling of canyon mouth width as a function of drainage area. Canyon walls are often near the angle of repose down to the modern channel, and as larger drainage-area rivers tend to themselves be wider (Leopold and Maddock, 1953; Montgomery and Gran, 2001), it follows that canyon wall width should scale with upstream drainage area. Wind-affected canyons (cyan, magenta symbols) show a similar relationship yet are wider by approximately 100 m for a river of comparable drainage area.

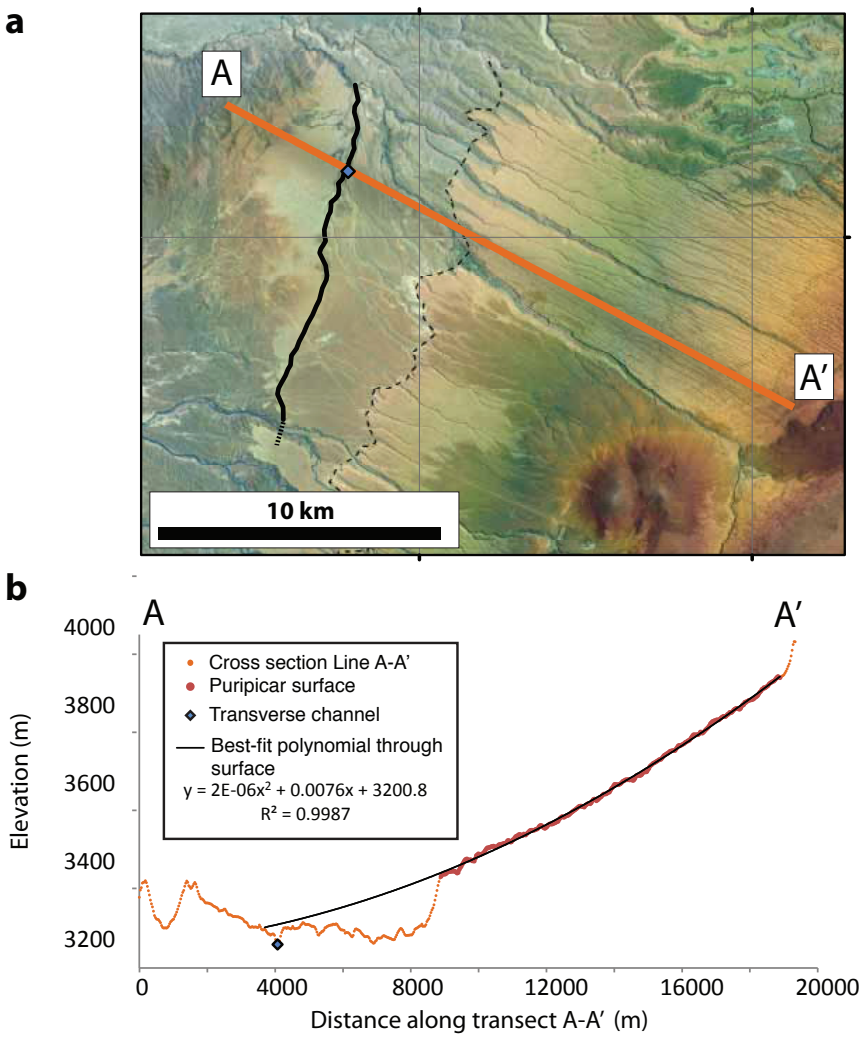

Figure 4.7: a. Map of the northern extent of the Puripicar ignimbrite showing the modern escarpment (black dashed line), initial escarpment (thick solid black line), and slope-parallel cross section line A-A'. **b.** Cross section A-A' showing the 30 m ASTER topography in orange, the Puripicar ignimbrite surface in red, and the location of the modern escarpment-parallel channel (blue diamond). The black line is the projection of the Puripicar surface into the valley using a best-fit polynomial. The surface projection intersects the topography at the approximate location of the escarpment-parallel channel at the base of an older hill, potentially marking the initial terminus of the ignimbrite as it flowed up against a local topographic high. Image ©Esri, ArcGIS 10. ASTER GDEM is a product of The Ministry of Economy, Trade, and Industry (METI) of Japan and the United States National Aeronautics and Space Administration (NASA).

4.4 Results and Discussion

For our topographic analysis we divide canyons into three populations that correspond to our three mapped initial escarpment locations (Fig. 4.2b). Both canyon head and escarpment retreat distances correlate with topographically forced variations in mean wind shear stress (Fig. 4.2c). We label these populations *fluvial*, *slow-wind*, and *fast-wind*, which correspond to protected, partially protected, and unprotected canyons, respectively. We measure along-channel horizontal retreat distances and find that the southern, fluvial canyons are retreating an average of 0.1 ± 0.1 mm/yr, with knickpoint crests located at the approximate lithologic boundary between the resistant caprock and less indurated basal unit of the tuff (Fig. 4.4a). The partially protected slow-wind canyon retreat rates increase by a factor of 2 (0.2 ± 0.1 mm/yr), and the unprotected fast-wind retreat rates increase by a factor of 17 (1.7 ± 0.7 mm/yr, Fig. 4.4d). This observed nonlinear dependence of canyon incision on shear stress is consistent with models of wind abrasion by saltating sediment (Anderson, 1986; Greeley et al., 1982). Additionally, wind-affected canyons are 100 m wider at their mouths for rivers of similar drainage area (Fig. 4.7), and wind-affected canyon heads have uniformly migrated downwind of knickpoint crests (Figs. 4.2b, 4.4b,d, and 4.8). This suggests that abrasion is occurring along canyon walls as well as above the crests of knickpoints.

We see clear field evidence for aeolian abrasion within wind-affected canyons in the form of erosional shadows where toppled blocks have shielded the underlying tuff from surface deflation (Fig. 4.4e). Once fallen, the blocks abrade in place, leaving upwind-facing horizontal fingers formed by the preferential erosion of weaker matrix around lithic inclusions (Fig. 4.9). Though availability of wind-transportable material is scarce, the ignimbrite may provide its own tools

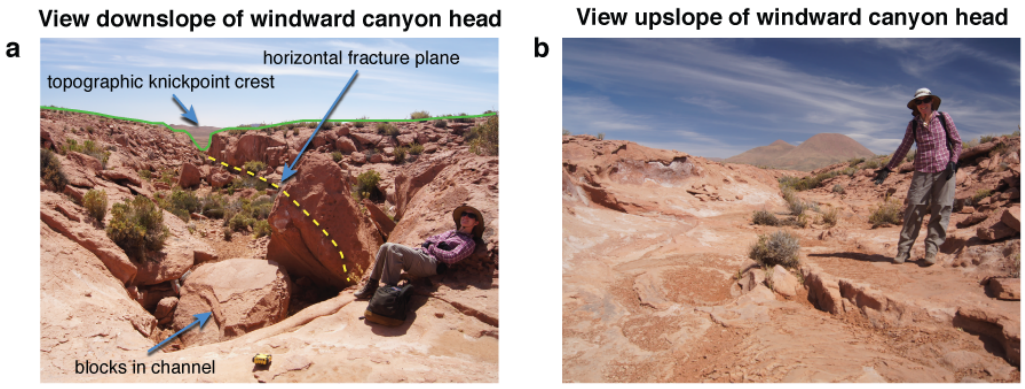

Figure 4.8: **a.** Photo taken looking downslope from the head of a windward canyon (the location where channel walls begin to significantly widen toward the escarpment). This location corresponds to the upper-most point in the canyon where blocks are delivered to the channel. An arrow points to the knickpoint crest located along the horizon line (low point along green line). The fracture plane that comprises the lower boundary of the blocks is shown as a dashed yellow line. **b.** View looking upslope from the same location, revealing a lack of boulders or sediment within the channel. From this point the channel is of relatively constant depth and width upslope.

for erosion via surface weathering (Fig. 4.10) and abrasion (Fig 4.9).

An additional topographic signature of this process transition exists in the canyon profile morphology. Mean knickpoint slopes in the slow-wind regime are approximately half that of the fluvial regime (0.22 ± 0.13 and 0.39 ± 0.17, respectively), and mean knickpoint slopes in the fast-wind regime are another factor of two less (0.11 ± 0.07, Fig. 4.4c). The contrast in knickpoint slope and retreat distance between wind-protected and wind-affected canyons suggests that wind abrasion alters canyon morphology by both propagating knickpoints downwind and reducing their slope. We hypothesize that the topographic forcing of wind over a knickpoint leads to enhanced abrasion at its crest and consequently a more aerodynamic canyon geometry. As winds tend to speed up at topographic highs due to streamline compression (Jackson and Hunt, 1975), and wind abrasion rate is extremely sensitive to changes in boundary shear stress (e.g., Anderson,

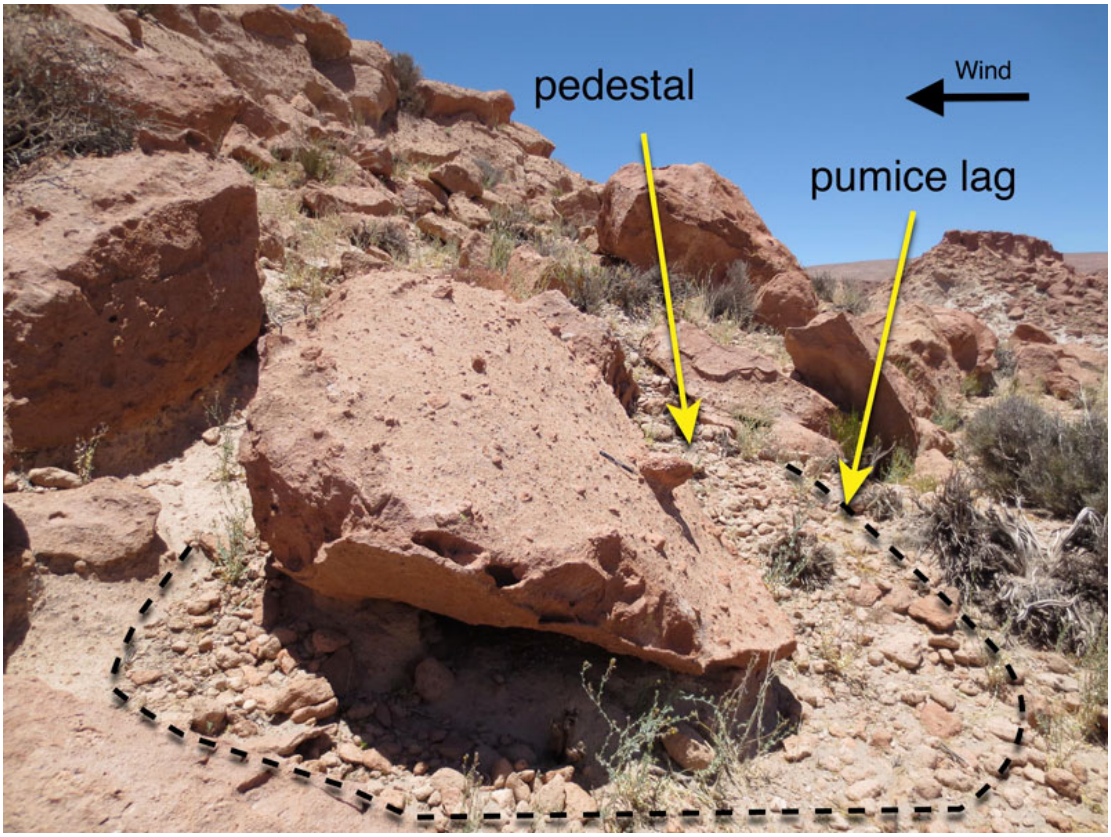

Figure 4.9: Field photo showing evidence for wind abrasion of a toppled block. The left arrow points to a horizontal finger-like protrusion formed by preferential erosion of the sandy matrix around a lithic pumice clast (note pen for scale at object base). The right arrow highlights a zone of pumice clasts surrounding the boulders that are forming a lag deposit as the blocks abrade away.

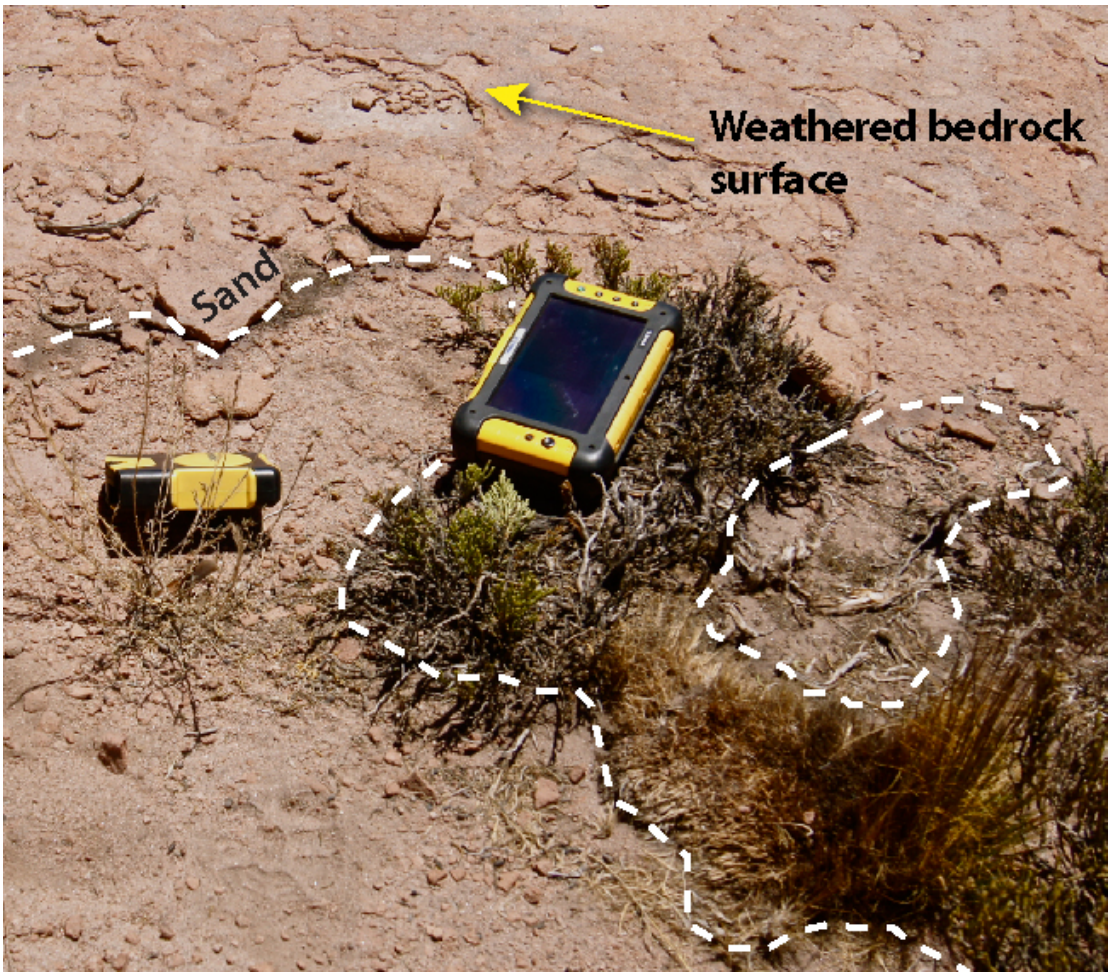

Figure 4.10: Field photo showing evidence for wind abrasion of a toppled block. The left arrow points to a horizontal finger-like protrusion formed by preferential erosion of the sandy matrix around a lithic pumice clast (note pen for scale at object base). The right arrow highlights a zone of pumice clasts surrounding the boulders that are forming a lag deposit as the blocks abrade away.

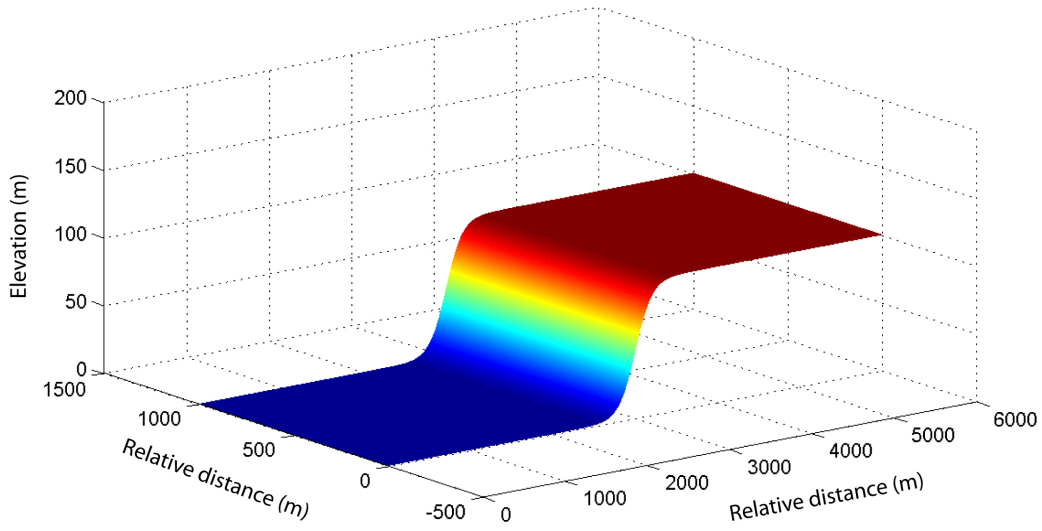

Figure 4.11: An example of the computational domain used for our static wind model analysis. The ramp is 1000 m wide by 6000 m long, with a height of 100 m. The topographic slope follows the general expression $1/(1 + ce^{-x})$, where c is a constant that governs the slope magnitude.

1986), topography should exert an influence on local wind abrasion rates.

We show this effect through wind model simulations over idealized topography with representative step dimensions from our fluvial, slow-wind, and fast-wind populations (Fig. 4.11, 4.12; see *Methods* section for model information). Steep-sloping fluvial knickpoints produce a three-fold increase in normalized wind surface shear stress at the knickpoint crest (Fig 4d). Erosion will thus focus along the crest due to the nonlinear dependence of abrasion rate on shear stress (Anderson, 1986). This speed-up effect diminishes significantly for representative canyons in the slow-wind regime, and all but disappears for slopes in the fast-wind regime (Fig. 4.12). A constant shear stress distribution across the fast-wind profile suggests these canyons represent equilibrium shapes (that can still propagate downwind), whereas the wind-protected fluvial profiles are highly unstable within a wind abrasion regime.

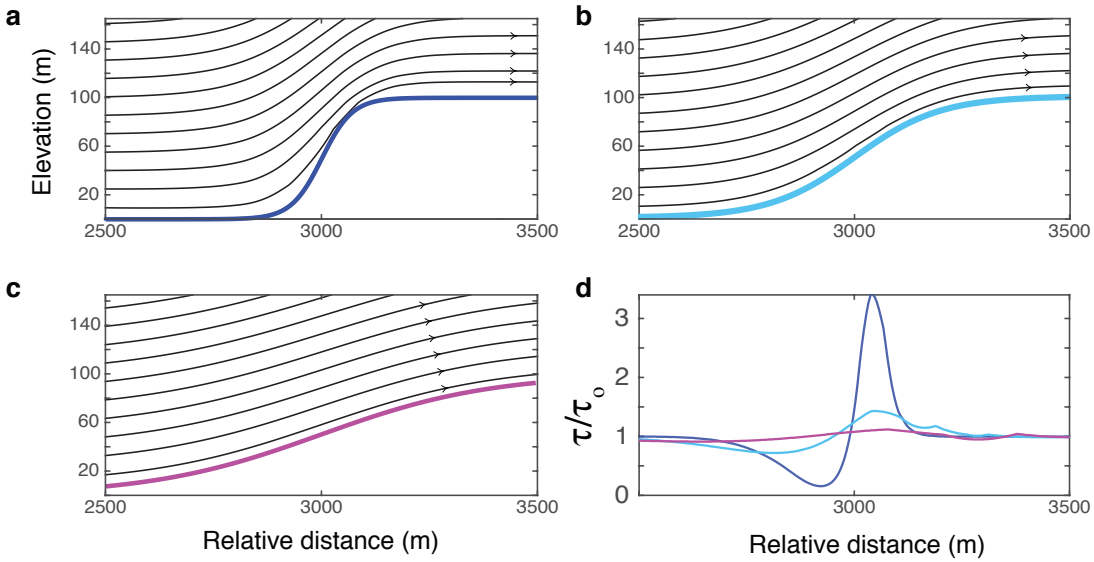

Figure 4.12: Results of wind model runs over 2D topographic ramps. **a-c** show streamlines for three model runs over sigmoidal ramps with step dimensions equal to the fluvial, slow-wind, and fast-wind populations. Streamline compression signifies an increase in the vertical gradient of horizontal wind speed. **d** shows associated surface shear stress (τ) normalized to incident shear stress (τ_o) for each topographic profile.

As a secondary approach to complement our static wind model results, we forward model channel profile evolution using an aeolian saltation abrasion model (e.g., Greeley, 1984; Anderson, 1986; Bridges et al., 2012) and an empirical expression for wind shear over an escarpment (ASCE, 2010; see *Methods* section for model description). Starting with a sigmoidal ramp of the same dimensions as our mean wind-protected population (Fig. 4.13), we run the model forward in time. As Figure 4.14 shows, the steep slope of the initial knickpoint causes shear stress to peak at the knickpoint crest, which drives increased abrasion and lengthening of the step. As the horizontal length scale increases, the speed-up effect in the empirical wind model diminishes until a slope of approximately 0.1 is reached, and the abrasion rate approaches a constant distribution across the channel that depends only on the channel slope. Thus, an equilibrium ramp slope is eventually reached which propagates downwind. Once the resistant caprock is breached, the vertical abrasion rate above the crest is comparable to the knickpoint propagation rate, and the knickpoint disappears. However, our model only works in the limit that a defined knickpoint crest can be identified. This is an inherent weakness in our model, and a refined wind model would eliminate this limitation and more of the parameter space could be explored. Regardless, a general picture emerges that, so long as it is possible to flux sediment up the knickpoint slope, the inherent geometry of the profile will cause the knickpoint slope to be effectively streamlined as it propagates downwind.

4.5 Conclusions

Taken together, our results show that topography influences wind-driven landscape evolution at varying scales: topographic shielding of high wind potential by mountains modulates the pace of canyon retreat along the Puripicar, and

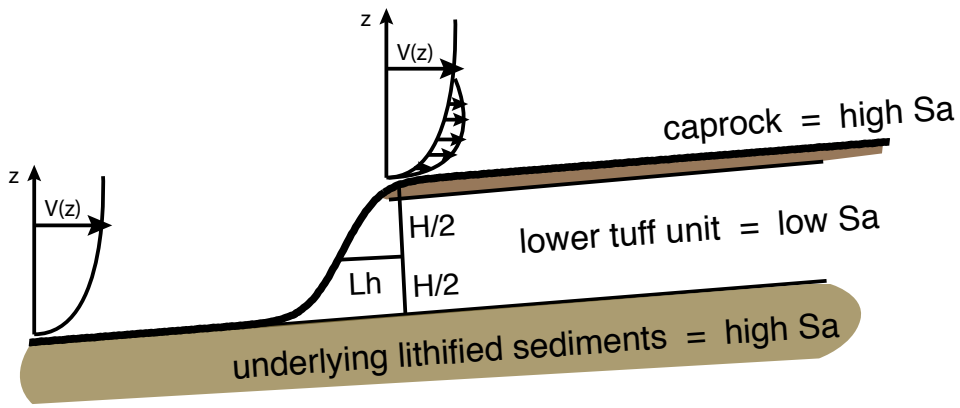

Figure 4.13: Diagram showing the parameters used in our 1D wind abrasion profile evolution model.

enhanced wind shear over knickpoints governs local abrasion rate within individual canyons. Though our results suggest wind-affected canyons appear to have a distinct topographic signature, fluvial knickpoint morphology can also vary greatly depending on the erosion process (Weissel and Seidl, 1998), and therefore shallow knickpoint geometries are not a unique indicator of the wind abrasion process. However, large regions of both Mars and Earth contain evidence of bedrock abrasion by wind (Goudie, 2008; McCauley, 1973), and within these landscapes wind may contribute significantly to landscape evolution through the abrasion of arid canyon systems. Furthermore, windblown sediment transport through canyons may not coincide with the fluvial transport direction and may potentially complicate sediment routing and budgets.

On Mars, many valley networks are commonly located near zones of high wind abrasion potential (Armstrong and Leovy, 2005). Thus current channel forms may not accurately reflect the fluvial processes that initially carved them. Because wind has the potential to significantly alter channel morphology by both widening

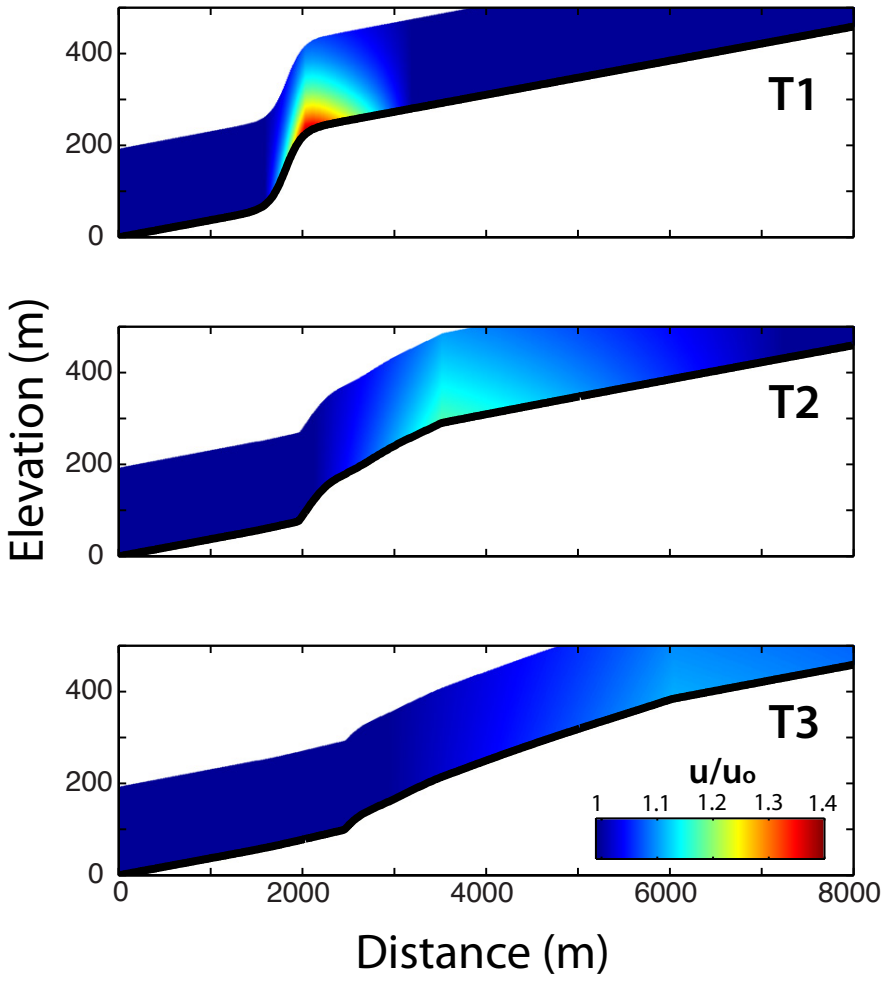

Figure 4.14: Three time slices in our numerical abrasion model. Colors show the fractional speed-up of the velocity field relative to the incident wind profile.

and deepening, paleo-hydrologic reconstructions from ancient Martian channels may require additional constraints to account for the potential effect of persistent wind abrasion. We note that yardang canyons in the Puripicar ignimbrite evolved while rivers have actively contributed to canyon incision. This overprinting of process makes wind abraded canyons difficult to identify and highlights the possibility that even when water was present on the Martian surface, wind may still have contributed to canyon formation. Determining the intermittency of both surface water and wind sediment transport events should aid in determining the relative contribution of these processes in arid, windy canyon systems.

4.6 Acknowledgements

We thank Kerri Johnson and David M. Rubin for field assistance and discussions that helped improve this manuscript. We thank Hector Toro Rivadera for logistical support in Chile, and Natalie Wagenbrenner for help with wind modeling. This work was funded by National Science Foundation grants EAR 0908850 (N.J.F.), EAR 0908324 (S. de S.), and NASA NNX10AP79G (S. de S.).

Chapter 5

Concluding remarks

The research presented in these chapters show that magmatic processes within the Central Andes are reflected in the topography at a range of spatial and temporal scales. At the first-order spatial scale of the Altiplano-Puna Magma Body, the molten batholith that feeds the 11 Myr ignimbrite flare-up of the APVC, magmatic addition to the crust appears to cause localized uplift that makes the APVC a distinct plateau from both the low-elevation Altiplano to the north and the high-relief, fault-bounded blocks of the Puna plateau to the south. In Chapter 2 we've shown that topographic estimates of the plutonic volume of the APMB are comparable to independent estimates from seismic imaging, suggesting that topography can be used to constrain mantle melt flux in areas of magmatic intrusion. Plutons are the building blocks of continental crust, and this study represents one of the few constraints on the active growth rates of a nascent batholith. Furthermore, this work suggests that magmatic addition can be a fundamental control the surface uplift history of a convergent orogen, a process often neglected in conceptual and numerical models (e.g., DeCelles et al., 2009; Pelletier et al., 2010).

At a second-order spatial scale of 35-50 km and a temporal scale of of 10-100

kyrs, deformation styles of actively growing volcanic systems can help determine the magnitude, duration, and mechanism of melt ascent from deeper to shallow reservoirs. Chapter 3 shows two examples of actively deforming volcanic centers that are thought to be potential collapse-caldera systems: Uturuncu Volcano (e.g., Sparks et al., 2008), and Lastarria-Cordon del Azufre (e.g., Ruch and Walter, 2014). Active uplift at Uturuncu occurs over a 70 km diameter footprint and centers at the peak of the 15 km diameter volcanic edifice, yet no long-wavelength topographic anomaly is present. Conversely, Lazufre has no volcanic edifice, yet the active uplift is spatially correlated with a 500 m amplitude, long-wavelength topographic dome that has persisted since 0.3 Ma.

Though our paleo-geodetic constraints from abandoned shorelines and river longitudinal profiles show no permanent measurable deformation since the 16 ka Tauca highstand, the topographic signals suggest distinct processes of melt ascent. This may have to do with the fact that Uturuncu lies at the center of the APMB, whereas Lazufre lies farther to the south and thus comes from a distinct parent body. Given the 15 km source depth associated with the intrusion beneath Uturuncu, and our topographic constraints, it is likely that the deformation at Uturuncu arises from a deep crustal source feeding melt into the APMB (e.g., Henderson and Pritchard, 2013). Thus, not only can we observe the surface uplift associated with the bulk emplacement of mantle melt into the crust as shown in Chapter 2, we can utilize the time-series of deformation at Uturuncu to observe the upward ascent of melt from the lower to middle crust.

At Lazufre, the shallower source depth and long-duration, long-wavelength topographic anomaly suggest prolonged magmatic inflation. Together with volcano-morphological evidence (e.g., Froger et al., 2007), our data suggest that Lazufre is a growing pre-caldera system. A key test of this hypothesis would be

whether the geochemistery of the ring of volcanoes that circumnavigate Lazufre reveal a genetic relationship. If so, that would reveal Lazufre to be a growing magmatic system on the scale of Yellowstone caldera (e.g., Ruch and Walter, 2014) and would thus warrant an increased level of monitoring in the future.

Lastly, at the 1-10 km scale, I show that the unique topographic and lithologic characteristics of ignimbrites can be used to quantify the mechanics of landscape evolution by wind-driven sediment transport, a process fundamental to the surface evolution of arid environments on earth as well as those of solar system bodies such as Mars, Venus, Titan, and Pluto (e.g., Greeley and Iversen, 1984; Stern et al., 2015). Utilizing a natural experiment within the Puripicar ignimbrite in northern Chile, we show that canyons are growing by the combined effects of wind and water erosion. Within the two-phase lithology of the ignimbrites, wherein a weak unwelded tuff layer is overlain by a resistant, welded caprock, the processes of wind and water abrasion leave distinct topographic signatures in the canyon profiles. Vertical drilling and headward retreat by plunge pool erosion appears to be the dominant process of fluvial canyon retreat along the Puripicar, whereas increased shear stress caused by wind speed-up at the crest of knickpoints appears to streamline canyon profiles as the knickpoints propagate downwind. Though we describe one mechanism of wind abrasion within Chapter 4, a broader implication is that pre-existing channels within a landscape can act as traps and conduits for windblown sediment. On planets like Mars, where water vanished from the surface 3 Gyrs ago and where windblown sediment fluxes remain high (e.g., Bridges et al., 2011), river canyons and surface fractures may act as local sources for wind abrasion and thus canyon morphology observed in the present-day may not necessarily reflect the magnitude of water or tectonics that initially created these features.

Bibliography

[1] Oded Aharonson, Maria T. Zuber, Daniel H. Rothman, Norbert Schorghofer, and Kelin X. Whipple. Drainage basins and channel incision on mars. *Proceedings of the National Academy of Sciences*, 99(4):1780–1783, 2002.

[2] Richard W. Allmendinger, Teresa E. Jordan, Suzanne M. Kay, and Bryan L. Isacks. The evolution of the altiplano-puna plateau of the central andes. *Annual Review of Earth and Planetary Sciences*, 25(1):139–174, 1997.

[3] Robert S. Anderson. Erosion profiles due to particles entrained by wind: Application of an eolian sediment-transport model. *Geological Society of America Bulletin*, 97(10):1270–1278, 1986.

[4] John C. Armstrong and Conway B. Leovy. Long term wind erosion on mars. *Icarus*, 176(1):57 – 74, 2005.

[5] ASCE. *Minimum Design Loads for Buildings and Other Structures*. American Society of Civil Engineers, Reston, VA, asce/sei 7-10 edition, 2010.

[6] A.Yu Babeyko, S.V Sobolev, R.B Trumbull, O Oncken, and L.L Lavier. Numerical models of crustal scale convection and partial melting beneath the altiplano–puna plateau. *Earth and Planetary Science Letters*, 199(3–4):373 – 388, 2002.

[7] John E. Bailey, Stephen Self, Luke K. Wooller, and Peter J. Mouginis-Mark. Discrimination of fluvial and eolian features on large ignimbrite sheets around la pacana caldera, chile, using landsat and srtm-derived {DEM}. *Remote Sensing of Environment*, 108(1):24 – 41, 2007.

[8] Victor R. Baker. Water and the martian landscape. *Nature*, 412(6843):228–236, 07 2001.

[9] Susan L. Beck, George Zandt, Stephen C. Myers, Terry C. Wallace, Paul G. Silver, and Lawrence Drake. Crustal-thickness variations in the central andes. *Geology*, 24(5):407–410, 1996.

[10] Susan L. Beck, George Zandt, Kevin M. Ward, and Alissa Scire. Multiple styles and scales of lithospheric foundering beneath the puna plateau, central andes. *Geological Society of America Memoirs*, 212:43–60, 2015.

[11] Pierre-Henri Blard, Jérôme Lave, Kenneth A. Farley, Victor Ramirez, Nestor Jimenez, Léo C.P. Martin, Julien Charreau, Bouchaïb Tibari, and Michel Fornari. Progressive glacial retreat in the southern altiplano (uturuncu volcano, 22 °s) between 65 and 14 ka constrained by cosmogenic 3he dating. *Quaternary Research*, 82(1):209 – 221, 2014.

[12] S. Bonvalot, G. Balmino, A. Briais, M. Kuhn, A. Peyrefitte, N. Vales, R. Biancale, G. Gabalda, F. Reinquin, and M. Sarrailh. *World Gravity Map*. Comission for the Geological Map of the World, Paris, 2012.

[13] N. T. Bridges, F. Ayoub, J-P. Avouac, S. Leprince, A. Lucas, and S. Mattson. Earth-like sand fluxes on mars. *Nature*, 485(7398):339–342, 05 2012.

[14] Michael H. Carr and Gary D. Clow. Martian channels and valleys: Their characteristics, distribution, and age. *Icarus*, 48(1):91 – 117, 1981.

[15] Matthew J. Comeau, Martyn J. Unsworth, Faustino Ticona, and Mayel Sunagua. Magnetotelluric images of magma distribution beneath volcán uturuncu, bolivia: Implications for magma dynamics. *Geology*, 2015.

[16] S. L. de Silva. Altiplano-puna volcanic complex of the central andes. *Geology*, 17(12):1102–1106, 1989.

[17] Shanaka De Silva, George Zandt, Robert Trumbull, José G. Viramonte, Guido Salas, and Néstor Jiménez. Large ignimbrite eruptions and volcano-tectonic depressions in the central andes: a thermomechanical perspective. *Geological Society, London, Special Publications*, 269(1):47–63, 2006.

[18] Shanaka L. de Silva and William D. Gosnold. Episodic construction of batholiths: Insights from the spatiotemporal development of an ignimbrite flare-up. *Journal of Volcanology and Geothermal Research*, 167(1–4):320 – 335, 2007. Large Silicic Magma Systems.

[19] Shanaka L. de Silva, Nancy R. Riggs, and Andrew P. Barth. Quickening the pulse: Fractal tempos in continental arc magmatism. *Elements*, 11(2):113–118, 2015.

[20] S.L. de Silva. Geochronology and stratigraphy of the ignimbrites from the 21 °30's to 23 °30's portion of the central andes of northern chile. *Journal of Volcanology and Geothermal Research*, 37(2):93 – 131, 1989.

[21] S.L. de Silva, J.E. Bailey, K.E. Mandt, and J.M. Viramonte. Yardangs in terrestrial ignimbrites: Synergistic remote and field observations on earth with applications to mars. *Planetary and Space Science*, 58(4):459 – 471, 2010. Exploring other worlds by exploring our own: The role of terrestrial analogue studies in planetary exploration.

[22] Peter G. DeCelles, Mihai N. Ducea, Paul Kapp, and George Zandt. Cyclicity in cordilleran orogenic systems. *Nature Geosci*, 2(4):251–257, 04 2009.

[23] Michele Dragoni and Cecilia Magnanensi. Displacement and stress produced by a pressurized, spherical magma chamber, surrounded by a viscoelastic shell. *Physics of the Earth and Planetary Interiors*, 56(3–4):316 – 328, 1989.

[24] Mihai N. Ducea and Mark D. Barton. Igniting flare-up events in cordilleran arcs. *Geology*, 35(11):1047–1050, 2007.

[25] Josef Dufek, Jason Wexler, and Michael Manga. Transport capacity of pyroclastic density currents: Experiments and models of substrate-flow interaction. *Journal of Geophysical Research: Solid Earth*, 114(B11):n/a–n/a, 2009. B11203.

[26] Ken L. Ferrier, Kimberly L. Huppert, and J. Taylor Perron. Climatic control of bedrock river incision. *Nature*, 496(7444):206–209, 04 2013.

[27] Yuri Fialko and Jill Pearse. Sombrero uplift above the altiplano-puna magma body: Evidence of a ballooning mid-crustal diapir. *Science*, 338(6104):250–252, 2012.

[28] Jonathan Fink. Surface folding and viscosity of rhyolite flows. *Geology*, 8(5):250–254, 1980.

[29] Noah J. Finnegan and Matthew E. Pritchard. Magnitude and duration of surface uplift above the socorro magma body. *Geology*, 37(3):231–234, 2009.

[30] Donald W. Forsyth. Subsurface loading and estimates of the flexural rigidity of continental lithosphere. *Journal of Geophysical Research: Solid Earth*, 90(B14):12623–12632, 1985.

[31] Jason M. Forthofer, Bret W. Butler, and Natalie S. Wagenbrenner. A comparison of three approaches for simulating fine-scale surface winds in support of wildland fire management. part i. model formulation and comparison against measurements. *International Journal of Wildland Fire*, 23(7):969–981, 2014.

[32] C. M. R. Fowler. *The Solid Earth*. Cambridge University Press, second edition, 2004. Cambridge Books Online.

[33] J.-L. Froger, D. Remy, S. Bonvalot, and D. Legrand. Two scales of inflation at lastarria-cordon del azufre volcanic complex, central andes, revealed from asar-envisat interferometric data. *Earth and Planetary Science Letters*, 255(1–2):148 – 163, 2007.

[34] Carmala N. Garzione, David J. Auerbach, Johanna Jin-Sook Smith, Jose J. Rosario, Benjamin H. Passey, Teresa E. Jordan, and John M. Eiler. Clumped isotope evidence for diachronous surface cooling of the altiplano and pulsed surface uplift of the central andes. *Earth and Planetary Science Letters*, 393:173 – 181, 2014.

[35] Prosenjit Ghosh, Carmala N. Garzione, and John M. Eiler. Rapid uplift of the altiplano revealed through 13c-18o bonds in paleosol carbonates. *Science*, 311(5760):511–515, 2006.

[36] Grove Karl Gilbert. Lake bonneville. Technical report, 1890.

[37] Andrew S. Goudie. Mega-yardangs: A global analysis. *Geography Compass*, 1(1):65–81, 2007.

[38] Karen B. Gran and David R. Montgomery. Spatial and temporal patterns in fluvial recovery following volcanic eruptions: Channel response to basin-wide sediment loading at mount pinatubo, philippines. *Geological Society of America Bulletin*, 117(1-2):195–211, 2005.

[39] Ronald Greeley, Rodman N. Leach, Steven H. Williams, Bruce R. White, James B. Pollack, David H. Krinsley, and John R. Marshall. Rate of wind abrasion on mars. *Journal of Geophysical Research: Solid Earth*, 87(B12):10009–10024, 1982.

[40] P.M. Gregg, S.L. de Silva, E.B. Grosfils, and J.P. Parmigiani. Catastrophic caldera-forming eruptions: Thermomechanics and implications for eruption triggering and maximum caldera dimensions on earth. *Journal of Volcanology and Geothermal Research*, 241–242:1 – 12, 2012.

[41] S. T. Henderson and M. E. Pritchard. Decadal volcanic deformation in the central andes volcanic zone revealed by insar time series. *Geochemistry, Geophysics, Geosystems*, 14(5):1358–1374, 2013.

[42] Alan D. Howard, William E. Dietrich, and Michele A. Seidl. Modeling fluvial erosion on regional to continental scales. *Journal of Geophysical Research: Solid Earth*, 99(B7):13971–13986, 1994.

[43] Alan D. Howard, Jeffrey M. Moore, and Rossman P. Irwin. An intense terminal epoch of widespread fluvial activity on early mars: 1. valley network

incision and associated deposits. *Journal of Geophysical Research: Planets*, 110(E12):n/a–n/a, 2005. E12S14.

[44] Bryan L. Isacks. Uplift of the central andean plateau and bending of the bolivian orocline. *Journal of Geophysical Research: Solid Earth*, 93(B4):3211–3231, 1988.

[45] P. S. Jackson and J. C. R. Hunt. Turbulent wind flow over a low hill. *Quarterly Journal of the Royal Meteorological Society*, 101(430):929–955, 1975.

[46] Brian R. Jicha and Oliver Jagoutz. Magma production rates for intraoceanic arcs. *Elements*, 11(2):105–111, 2015.

[47] T. E. Jordan, P. L. Nester, N. Blanco, G. D. Hoke, F. Dávila, and A. J. Tomlinson. Uplift of the altiplano-puna plateau: A view from the west. *Tectonics*, 29(5):n/a–n/a, 2010. TC5007.

[48] Leif Karlstrom, Heather M. Wright, and Charles R. Bacon. The effect of pressurized magma chamber growth on melt migration and pre-caldera vent locations through time at mount mazama, crater lake, oregon. *Earth and Planetary Science Letters*, 412:209 – 219, 2015.

[49] Suzanne Mahlburg Kay and Beatriz L Coira. Shallowing and steepening subduction zones, continental lithospheric loss, magmatism, and crustal flow under the central andean altiplano-puna plateau. *Geological Society of America Memoirs*, 204:229–259, 2009.

[50] Suzanne Mahlburg Kay, Beatriz L. Coira, Pablo J. Caffe, and Chang-Hwa Chen. Regional chemical diversity, crustal and mantle sources and evolution of central andean puna plateau ignimbrites. *Journal of Volcanology and Geothermal Research*, 198(1–2):81 – 111, 2010.

[51] R. Kreuels, K. Fraedrich, and E. Ruprecht. An aerological climatology of south america. *Meteorologische Runschau*, 28:17–24, 1975.

[52] Michael P. Lamb, William E. Dietrich, Sarah M. Aciego, Donald J. DePaolo, and Michael Manga. Formation of box canyon, idaho, by megaflood: Implications for seepage erosion on earth and mars. *Science*, 320(5879):1067–1070, 2008.

[53] Michael P. Lamb, Alan D. Howard, William E. Dietrich, and J. Taylor Perron. Formation of amphitheater-headed valleys by waterfall erosion after large-scale slumping on hawai'i. *Geological Society of America Bulletin*, 119(7-8):805–822, 2007.

[54] L. B. Leopold and Thomas Maddock Jr. The hydraulic geometry of stream channels and some physiographic implications. Technical report, 1953.

[55] Peter W. Lipman. The roots of ash flow calderas in western north america: Windows into the tops of granitic batholiths. *Journal of Geophysical Research: Solid Earth*, 89(B10):8801–8841, 1984.

[56] J. J. Major, T. C. Pierson, R. L. Dinehart, and J. E. Costa. Sediment yield following severe volcanic disturbance - a two-decade perspective from mount st. helens. 28(9):819–822, 2000.

[57] John F. McCauley. Mariner 9 evidence for wind erosion in the equatorial and mid-latitude regions of mars. *Journal of Geophysical Research*, 78(20):4123–4137, 1973.

[58] Peter Molnar and Joann M. Stock. Slowing of india's convergence with eurasia since 20 ma and its implications for tibetan mantle dynamics. *Tectonics*, 28(3):n/a–n/a, 2009. TC3001.

[59] David R. Montgomery, Joshua L. Bandfield, and Scott K. Becker. Periodic bedrock ridges on mars. *Journal of Geophysical Research: Planets*, 117(E3):n/a–n/a, 2012. E03005.

[60] David R. Montgomery and Karen B. Gran. Downstream variations in the width of bedrock channels. *Water Resources Research*, 37(6):1841–1846, 2001.

[61] Z. M. Moratto, M. J. Broxton, R. A. Beyer, M. Lundy, and K. Husmann. Ames Stereo Pipeline, NASA's Open Source Automated Stereogrammetry Software. In *Lunar and Planetary Science Conference*, volume 41 of *Lunar and Planetary Inst. Technical Report*, page 2364, March 2010.

[62] D. D. Muir, D. N. Barfod, J. D. Blundy, A. C. Rust, R. S. J. Sparks, and K. M. Clarke. The temporal record of magmatism at cerro uturuncu, bolivian altiplano. *Geological Society, London, Special Publications*, 422, 2015.

[63] J. Naranjo and P. Cornejo. Hoja salar de la isla. 72, 1992.

[64] Peter L. Nester, Eugenia Gayó, Claudio Latorre, Teresa E. Jordan, and Nicolás Blanco. Perennial stream discharge in the hyperarid atacama desert of northern chile during the latest pleistocene. *Proceedings of the National Academy of Sciences*, 104(50):19724–19729, 2007.

[65] Shunji Ouchi. Response of alluvial rivers to slow active tectonic movement. *Geological Society of America Bulletin*, 96(4):504–515, 1985.

[66] Scott R. Paterson and Mihai N. Ducea. Arc magmatic tempos: Gathering the evidence. *Elements*, 11(2):91–98, 2015.

[67] Jill Pearse and Paul Lundgren. Source model of deformation at lazufre volcanic center, central andes, constrained by insar time series. *Geophysical Research Letters*, 40(6):1059–1064, 2013.

[68] Jon D. Pelletier, Peter G. DeCelles, and George Zandt. Relationships among climate, erosion, topography, and delamination in the andes: A numerical modeling investigation. *Geology*, 38(3):259–262, 2010.

[69] Julita C. Penido, Caleb I. Fassett, and Sanjoy M. Som. Scaling relationships and concavity of small valley networks on mars. *Planetary and Space Science*, 75:105 – 116, 2013.

[70] David C. Pieri. Martian valleys: Morphology, distribution, age, and origin. *Science*, 210(4472):895–897, 1980.

[71] Christa Placzek, Jay Quade, and P. Jonathan Patchett. Geochronology and stratigraphy of late pleistocene lake cycles on the southern bolivian altiplano: Implications for causes of tropical climate change. *Geological Society of America Bulletin*, 118(5-6):515–532, 2006.

[72] Claudia B. Prezzi, Hans-Jürgen Götze, and Sabine Schmidt. 3d density model of the central andes. *Physics of the Earth and Planetary Interiors*, 177(3–4):217 – 234, 2009.

[73] Matthew E. Pritchard and Mark Simons. A satellite geodetic survey of large-scale deformation of volcanic centres in the central andes. *Nature*, 418(6894):167–171, 07 2002.

[74] J. Quade, M.P. Dettinger, B. Carrapa, P. DeCelles, K.E. Murray, K.W. Huntington, A. Cartwright, R.R. Canavan, G. Gehrels, and M. Clementz. The growth of the central andes, 22 °s–26 °s. *Geological Society of America Memoirs*, 212, 2014.

[75] Victor A. Ramos. The basement of the central andes: The arequipa and related terranes. *Annual Review of Earth and Planetary Sciences*, 36(1):289–324, 2008.

[76] D. Remy, J. L. Froger, H. Perfettini, S. Bonvalot, G. Gabalda, F. Albino, V. Cayol, D. Legrand, and M. De Saint Blanquat. Persistent uplift of the lazufre volcanic complex (central andes): New insights from pcaim inversion of insar time series and gps data. *Geochemistry, Geophysics, Geosystems*, 15(9):3591–3611, 2014.

[77] J. Ruch and T.R. Walter. Relationship between the insar-measured uplift, the structural framework, and the present-day stress field at lazufre volcanic area, central andes. *Tectonophysics*, 492(1–4):133 – 140, 2010.

[78] Morgan J. Salisbury, Brian R. Jicha, Shanaka L. de Silva, Brad S. Singer, Néstor C. Jiménez, and Michael H. Ort. 40Ar/39Ar chronostratigraphy of Altiplano-Puna volcanic complex ignimbrites reveals the development of a major magmatic province. *Geological Society of America Bulletin*, 123(5-6):821–840, 2011.

[79] L.M. Schoenbohm, K.X Whipple, B.C. Burchfiel, and L. Chen. Geomorphic constraints on surface uplift, exhumation, and plateau growth in the red river region, yunnan province, china. *Geological Society of America Bulletin*, 116(7-8):895–909, 2004.

[80] PAUL SEGALL. *Earthquake and Volcano Deformation*. Princeton University Press, 2010.

[81] M.A. Seidl and W.E. Dietrich. The problem of channel erosion into bedrock. *Catena Supplement*, 23:101–124, 1992.

[82] Brad S. Singer and et al. Dynamics of a large, restless, rhyolitic magma system at laguna del maule, southern andes, chile. *GSA Today*, 24(12):4–10, December 2014.

[83] Gary A. Smith. The influence of explosive volcanism on fluvial sedimentation; the deschutes formation (neogene) in central oregon. *Journal of Sedimentary Research*, 57(4):613–629, 1987.

[84] R. S. J. Sparks, C. B. Folkes, M. C.S. Humphreys, D. N. Barfod, J. Clavero, M. C. Sunagua, S. R. McNutt, and M. E. Pritchard. Uturuncu volcano, bolivia: Volcanic unrest due to mid-crustal magma intrusion. *American Journal of Science*, 308, 2008.

[85] S. A. Stern, F. Bagenal, K. Ennico, G. R. Gladstone, W. M. Grundy, W. B. McKinnon, J. M. Moore, C. B. Olkin, J. R. Spencer, H. A. Weaver, L. A. Young, T. Andert, J. Andrews, M. Banks, B. Bauer, J. Bauman, O. S. Barnouin, P. Bedini, K. Beisser, R. A. Beyer, S. Bhaskaran, R. P. Binzel, E. Birath, M. Bird, D. J. Bogan, A. Bowman, V. J. Bray, M. Brozovic, C. Bryan, M. R. Buckley, M. W. Buie, B. J. Buratti, S. S. Bushman, A. Calloway, B. Carcich, A. F. Cheng, S. Conard, C. A. Conrad, J. C. Cook, D. P. Cruikshank, O. S. Custodio, C. M. Dalle Ore, C. Deboy, Z. J. B. Dischner, P. Dumont, A. M. Earle, H. A. Elliott, J. Ercol, C. M. Ernst, T. Finley, S. H. Flanigan, G. Fountain, M. J. Freeze, T. Greathouse, J. L. Green, Y. Guo, M. Hahn, D. P. Hamilton, S. A. Hamilton, J. Hanley, A. Harch, H. M. Hart, C. B. Hersman, A. Hill, M. E. Hill, D. P. Hinson, M. E. Holdridge, M. Horanyi, A. D. Howard, C. J. A. Howett, C. Jackman, R. A. Jacobson, D. E. Jennings, J. A. Kammer, H. K. Kang, D. E. Kaufmann, P. Kollmann, S. M. Krimigis, D. Kusnierkiewicz, T. R. Lauer,

J. E. Lee, K. L. Lindstrom, I. R. Linscott, C. M. Lisse, A. W. Lunsford, V. A. Mallder, N. Martin, D. J. McComas, R. L. McNutt, D. Mehoke, T. Mehoke, E. D. Melin, M. Mutchler, D. Nelson, F. Nimmo, J. I. Nunez, A. Ocampo, W. M. Owen, M. Paetzold, B. Page, A. H. Parker, J. W. Parker, F. Pelletier, J. Peterson, N. Pinkine, M. Piquette, S. B. Porter, S. Protopapa, J. Redfern, H. J. Reitsema, D. C. Reuter, J. H. Roberts, S. J. Robbins, G. Rogers, D. Rose, K. Runyon, K. D. Retherford, M. G. Ryschkewitsch, P. Schenk, E. Schindhelm, B. Sepan, M. R. Showalter, K. N. Singer, M. Soluri, D. Stanbridge, A. J. Steffl, D. F. Strobel, T. Stryk, M. E. Summers, J. R. Szalay, M. Tapley, A. Taylor, H. Taylor, H. B. Throop, C. C. C. Tsang, G. L. Tyler, O. M. Umurhan, A. J. Verbiscer, M. H. Versteeg, M. Vincent, R. Webbert, S. Weidner, G. E. Weigle, O. L. White, K. Whittenburg, B. G. Williams, K. Williams, S. Williams, W. W. Woods, A. M. Zangari, and E. Zirnstein. The pluto system: Initial results from its exploration by new horizons. *Science*, 350(6258), 2015.

[86] Andrés Tassara and Andrés Echaurren. Anatomy of the andean subduction zone: three-dimensional density model upgraded and compared against global-scale models. *Geophysical Journal International*, 189(1):161–168, 2012.

[87] Jorge A. Vazquez and Mary R. Reid. Time scales of magma storage and differentiation of voluminous high-silica rhyolites at yellowstone caldera, wyoming. *Contributions to Mineralogy and Petrology*, 144(3):274–285, 2002.

[88] M. Vuille. Atmospheric circulation over the bolivian altiplano during dry and wet periods and extreme phases of the southern oscillation. *International Journal of Climatology*, 19(14):1579–1600, 1999.

[89] Thomas R. Walter and Mahdi Motagh. Deflation and inflation of a large magma body beneath uturuncu volcano, bolivia? insights from insar data, surface lineaments and stress modelling. *Geophysical Journal International*, 198(1):462–473, 2014.

[90] Kevin M. Ward, George Zandt, Susan L. Beck, Douglas H. Christensen, and Heather McFarlin. Seismic imaging of the magmatic underpinnings beneath the altiplano-puna volcanic complex from the joint inversion of surface wave dispersion and receiver functions. *Earth and Planetary Science Letters*, 404:43 – 53, 2014.

[91] A. B. Watts. *Isostasy and Flexure of the Lithosphere*. Cambridge University Press, Cambridge, UK, 2001.

[92] J.K. Weissel and M.A. Seidl. *Inland Propagation of Erosional Escarpments and River Profile Evolution Across the Southeast Australian Passive Continental Margin*, pages 189–206. American Geophysical Union, 1998.

[93] Charles W. Wicks, Wayne Thatcher, Daniel Dzurisin, and Jerry Svarc. Uplift, thermal unrest and magma intrusion at yellowstone caldera. *Nature*, 440(7080):72–75, 03 2006.

[94] S. Yun, P. Segall, and H. Zebker. Constraints on magma chamber geometry at sierra negra volcano, galápagos islands, based on insar observations. *Journal of Volcanology and Geothermal Research*, 150(1–3):232 – 243, 2006. The Changing Shapes of Active VolcanoesRecent Results and Advances in Volcano Geodesy.

[95] G. Zandt, M. Leidig, J. Chmielowski, D. Baumont, and X. Yuan. Seismic detection and characterization of the altiplano-puna magma body, central andes. *Pure and Applied Geophysics*, 160(3-4):789–807, 2003.